

Investigating the exchange of CO<sub>2</sub> in a tall-grass prairie ecosystem using stable isotopes and micrometeorological methods

by

Kyle Scott Stropes

B.S., in Agriculture, Kansas State University, 2014

A THESIS

submitted in partial fulfillment of the requirements for the degree

MASTER OF SCIENCE

Department of Agronomy  
College of Agriculture

KANSAS STATE UNIVERSITY  
Manhattan, Kansas

2017

Approved by:

Dr. Eduardo Alvarez Santos

# **Copyright**

© Kyle Stropes 2017.

## Abstract

Isotope analysis combined with micrometeorological techniques can bring new insights into the mechanisms governing biogeochemical cycles in ecosystems. New field-deployable optical sensors that have recently become available can provide accurate trace gas concentration measurements at sampling rates suitable for micrometeorological measurements. These instruments could help enhance current carbon cycling research efforts. This research will bring new insights into understanding the biophysical processes governing the carbon cycle at the ecosystem scale, which will be crucial for enhancing our future climate change scenario predictions. The impact that land use management has on the carbon cycle components of an ecosystem is an important issue that could be addressed with this new approach. More notably, research is needed to identify how management practices affect the abundance of C<sub>3</sub> and C<sub>4</sub> plant communities in grasslands and to identify how shifts in plant community composition can modify the net ecosystem exchange of CO<sub>2</sub>. Chapter 1 of this thesis provides a literature review on the carbon cycle in grasslands, stable isotope analysis in environmental mediums, and the combination of isotope analysis with micrometeorological methods to study carbon exchange at the ecosystem scale. In Chapter 2, we describe the evaluation of the performance for a multi-port sampling system's measurements of vertical concentration gradients of stable isotopes of CO<sub>2</sub>. The results of these analyzes show that the sampling system was suitable to measure vertical gradients of concentration under field conditions. Chapter 3 describes how the sampling system was used to study the isotope exchange in two watersheds at the Konza Prairie Biological station under distinct management conditions. Gradients of isotopes were measured in two adjacent watersheds (K2A and C3SA). The K2A watershed is burned every other year, while the C3SA watershed is in a patch-burn grazing system and is burned every three years. Results show that the sampling system's performance is adequate for our study. The sampling system was able to detect clear differences in the isotopic composition of nighttime NEE between the watersheds, which is believed to be greatly influenced by C<sub>3</sub> and C<sub>4</sub> plant community composition. Further research is needed to examine the role that other environmental conditions played on altering the isotopic signals of the NEE in each watershed. Additionally, other management practices should be examined using this sampling system to determine their impact on biophysical drivers in the ecosystem, which could subsequently impact the plant community abundance and diversity.

# Table of Contents

List of Figures .....	vi
List of Tables .....	ix
Chapter 1 - A literature review on the use of stable isotope analysis and micrometeorological techniques to investigate processes governing CO <sub>2</sub> exchange in ecosystems .....	1
1.1 Carbon cycle in grassland ecosystems .....	1
1.2 Monitoring carbon exchange in ecosystems .....	5
1.3 Stable isotopologues of CO <sub>2</sub> .....	7
1.4 Measures of stable isotopes .....	11
1.5 Stable isotope discrimination in plants .....	14
1.6 Isotope exchange in soils .....	18
1.7 Carbon isotope analysis in ecosystems .....	21
1.8 Chapter outlines and concluding remarks .....	31
Chapter 2 - Performance evaluation of a multiport sampling system to measure vertical gradients of CO <sub>2</sub> isotopes at the ecosystem scale.....	33
2.1 Introduction.....	33
2.2 Methodology .....	35
2.2.1 Instrumentation setup.....	35
2.2.2 Allan deviation analysis.....	38
2.2.3 Buffer volume tests .....	38
2.3 Results and discussions.....	42
2.3.1 Allan deviation.....	42
2.3.2 Buffer volumes and partial sampling errors.....	44
2.4 Conclusions .....	53
Chapter 3 - In-situ measurements of CO <sub>2</sub> isotope exchange using tunable diode laser spectroscopy and micrometeorological methods at a tall grass ecosystem .....	55
3.1 Introduction.....	55
3.2 Methodology .....	57
3.2.1 Site description.....	57
3.2.2 Isotope measurements.....	59

3.2.3 Flux measurements .....	61
3.2.4 Support measurements .....	63
3.2.5 Standardizing stable isotopic variations of CO <sub>2</sub> and isotope flux ratio method .....	66
3.3 Results and discussions .....	67
3.3.1 Site environmental conditions.....	67
3.3.2 Vegetation measurements .....	72
3.3.3 Soil CO <sub>2</sub> measurements .....	77
3.3.4 Ecosystem flux measurements .....	78
3.3.5 Temporal dynamics of the isotope exchange in grazed and ungrazed watersheds..	80
3.4 Conclusion .....	89
Bibliography .....	91
Appendix A - Table of the soil mapping units distribution for the K2A watershed.....	104
Appendix B - Table of the soil mapping units distribution for the C3SA watershed.....	105
Appendix C - IRGASON flux measurements compared to LI7500/CSAT3 flux measurements .....	106
Appendix D - Soil CO <sub>2</sub> respiration model statistic tables and graphs .....	107

## List of Figures

Figure 2.1 – A picture of the buffering volumes (metallic flasks) used with the multi-port sampling system.....	37
Figure 2.2 – (A) Allan deviation comparison of the tri-band and dual-band laser’s CO <sub>2</sub> mixing ratio signals and (B) shows the Allan deviation comparison of the tri-band and dual-band laser’s $\delta^{13}\text{C}$ signals. The averaging period (x axis) ranged from 0.1 to 1000 seconds. ....	44
Figure 2.3 – (A) shows the CO <sub>2</sub> mixing ratios (ppmv) measured from sampling inlets with and without air mixing volume treatments over time and (B) shows the CO <sub>2</sub> mixing ratio standard deviations (ppmv) for the gas sampling inlets with and without the air mixing volume apparatus treatment (inlets 5 and 6, respectively).....	46
Figure 2.4 – (A) shows partial sampling errors calculated (red dots) with respect to the full sample mean values for inlet 6 (without air-mixing) and (B) depicts results with respect to full sample mean values for inlet 5 (with air-mixing). The blue lines in both plots depict the maximum positive and negative errors of the CO <sub>2</sub> mixing ratio that can be estimated using the central limit theorem. ....	49
Figure 2.5 – (A) shows partial sampling errors calculated (red dots) with respect to full sample mean values for inlet 6, the treatment without air mixing and (B) depicts the results with respect to full sample mean values for inlet 5, the air mixed sample treatments. The blue lines in both figures depict the maximum positive and negative $\delta^{13}\text{C}$ (‰) errors values that can be estimated using the central limit theorem.....	50
Figure 2.6 – (A) shows the 30-minute average mixing ratio of CO <sub>2</sub> results of the multiple inlet tests and (B) shows the standard deviation values for these 30 minute averaging periods. The red shading represents the values of error for the 2-inlet treatment, black shading for the 4-inlet treatment, and blue shading for the 10-inlet treatment.....	51
Figure 2.7 – (A) shows the 30 minute average mixing ratio of $\delta^{13}\text{C}$ (‰) results of the multiple inlet tests and (B) shows the standard deviation values for these 30 minute averaging periods. The red shading represents the values of error for the 2-inlet treatment, black shading for the 4-inlet treatment, and blue shading for the 10-inlet treatment.....	53
Figure 3.1 – Schematic diagram illustrating of the isotope sampling system used in this study..	60

Figure 3.2 – A sample photograph of the canopy, where several grass species have fully bloomed. A National Ecological Observatory Network tower is on the right side of the picture. ....	65
Figure 3.3 – KPBS weather station’s 8-day temperature averages from 1981-2010 and the 2016 KPBS weather station’s 8-day temperature readings (°C). ....	68
Figure 3.4 – The KPBS weather station’s average cumulative precipitation normal totals (mm), from 1981 – 2010, and the KPBS weather station’s 2016 accumulated precipitation totals (mm).....	69
Figure 3.5 – (A) 30-minute average volumetric water content ( $\text{cm}^3 \text{ cm}^{-3}$ ) and (B) 30-minute soil temperature measured at 10 cm depth at the K2A watershed. ....	71
Figure 3.6 – Half-hourly values of shortwave radiation ( $\text{W m}^{-2}$ ) as measured by a pyranometer (LI200R, LICOR Biosciences, Lincoln, NE, USA). ....	71
Figure 3.7 – 3-day average green chromatic coordinate (GCC) values obtained from digital photographs taken at the K2A watershed in 2016. ....	73
Figure 3.8 – Plant heights during the growing season for the K2A watershed. Error bars in this chart depict the standard deviation found for each sampling period. ....	75
Figure 3.9 – Plant heights during the growing season for the C3SA watershed. Error bars in this chart depict the standard deviation found for each sampling period. ....	75
Figure 3.10 – (A) Leaf area index values for the K2A watershed and C3SA watershed and (B) Leaf area index standard deviation values for the K2A watershed and C3SA watershed....	77
Figure 3.11 – A multiple linear regression plot displaying the measured soil moisture content (%) and measured soil temperatures (°C) relationship with modeled soil $\text{CO}_2$ flux the dots are the measured independent variables and the colored grid is our linear regression plane. ....	78
Figure 3.12 – Half-hourly values on latent heat fluxes ( $\text{LE}, \text{W m}^{-2} \text{ s}^{-1}$ ) in the K2A watershed during the 2016 growing season. ....	79
Figure 3.13 – Half-hourly values of NEE for the K2A watershed compared to the modeled soil $\text{CO}_2$ respiration data. ....	80
Figure 3.14 – Half-hourly average values of: (A) $\text{CO}_2$ mixing ratio and (B) $\delta^{13}\text{C}$ of atmospheric $\text{CO}_2$ at the two watersheds. The values were derived based on the concentration readings from the top sampling inlets of the ungrazed and grazed watersheds (1.52 m and 1.5 m, respectively). ....	81

Figure 3.15 – Relationship between the isotopic flux-ratio signal in delta notation ( $\delta^{13}\text{C}_F$ ) versus the concentration gradient of  $\text{CO}_2$  in absolute form for the ungrazed (A) and grazed (B) watersheds. .... 84

Figure 3.16 – Half-hourly ensemble average of  $\delta^{13}\text{C}_F$  for 30 day-periods during (A) the midsummer (DOY 162 to DOY 192) and (B) early fall portion (DOY 220 to DOY 250) for the grazed (C3SA) and ungrazed (K2A) watersheds ..... 85

Figure 3.17 – Nightly average  $\delta^{13}\text{C}_F$  (‰) signal for the ungrazed watershed and the grazed watershed. .... 87

Figure 3.18 – Plots of (A) wind direction compared to the  $\delta^{13}\text{C}_F$  signal for the ungrazed watershed, (B) wind direction compared to the  $\delta^{13}\text{C}_F$  signal for the grazed watershed, (C) wind speed compared to the  $\delta^{13}\text{C}_F$  signal for the ungrazed watershed, and (D) wind speed compared to the  $\delta^{13}\text{C}_F$  signal for the grazed watershed..... 89



## List of Tables

Table 1.1 Common abundance of CO <sub>2</sub> isotopologues present in the free atmosphere, measured by the National Oceanic and Atmospheric Administration's ESRL division.....	7
Table 1.2 Primary fractionation events and their discrimination values against <sup>13</sup> CO <sub>2</sub> during photosynthesis.....	16

# **Chapter 1 - A literature review on the use of stable isotope analysis and micrometeorological techniques to investigate processes governing CO<sub>2</sub> exchange in ecosystems**

## 1.1 Carbon cycle in grassland ecosystems

The global carbon cycle is composed of many exchange mechanisms that are biotic and abiotic in nature. Photosynthesis is a major carbon pathway that is responsible for the exchange of CO<sub>2</sub> between the land surface and the atmosphere. Research suggests that global plant photosynthesis assimilates 175 Pg C per year (Welp, 2011). This assimilated carbon can be used by the plant for tissue growth and maintenance. Plant growth and maintenance metabolize the assimilated carbon, producing CO<sub>2</sub>. The efflux of CO<sub>2</sub> from the plant represents the plant's respiration. Estimates of global plant leaf respiration are roughly 60 Pg C per year (Atkin et al, 2015). Another important carbon exchange pathway is soil respiration. Soils anchor the plant's root systems and provide a habitat for many soil microorganisms within the rhizosphere, but soil microbes also exist outside of the rhizosphere. The plant's root system and the soil microbes can metabolize carbon assimilates and substrates creating an efflux of CO<sub>2</sub> from the soil. Our current estimates of global soil-CO<sub>2</sub> efflux to the atmosphere is approximately 91 Pg C per year (Raich & Schlesinger, 1992; Raich et al, 2002; Hashimoto et al, 2015). Continued research is needed to identify how biophysical processes, environmental drivers, and their feedbacks influence the carbon exchange components of the global carbon cycle, which will affect our ability to predict future climate change scenarios (Field et al, 2007). This research will be especially useful for studying the movement of carbon in ecosystems, such as grasslands.

Grassland ecosystems cover a significant portion of the Earth's land surface (White et al, 2000) and are major reservoirs of carbon (Conant, 2010). Human activities and management practices have led to major changes in the percent of land covered by grasslands (White et al, 2000; Anderson, 2006; Clay et al, 2014) and the loss of 50% to 70% of grassland soil carbon to the atmosphere (Schwartz, 2014). Studies have shown that grasslands are sensitive to changes in climate (Blair et al, 2014; Harrison et al, 2015) and are therefore susceptible to being influenced by global climate change. For example, Harrison et al. (2015) found that a decrease in midwinter precipitation led to a loss in grassland plant diversity. Since climate change is expected to alter the global pattern of precipitation events (Trenberth, 2011), there is the possibility of grasslands around the world losing their diversity. Blair et al. (2014) notes that there are documented shifts in the distribution of North American grasslands as a response to droughts, thereby suggesting that many grasslands have already been impacted by changes in precipitation patterns. Thus, there is an urgent need to study grassland management practices and to implement proper management practices that will help minimize or prevent further losses of carbon in grasslands, reduce losses of plant diversity, and make grasslands more resilient to climate change.

Animal grazing and prescribed burns are two major management practices influencing the carbon budget of grasslands (Conant, 2010; Collins & Calabrese, 2012; Blair et al, 2014). One direct impact that grazing and fires have on the carbon budget of grasslands is the removal of carbon from the ecosystem. Grazers remove carbon in a grassland by consuming plant material and assimilating the nutrients from plant material into their biomass. Fires remove carbon from the ecosystem because the combustion of organic matter releases carbon dioxide into the atmosphere. The frequency, intensity, and timing of these fire events can also influence the carbon budget of a grassland by changing the plant community composition and soil

properties of the ecosystem (Collins & Calabrese, 2012; Šimanský, 2015). Changes in plant community composition and in soil properties can change the carbon budget of the ecosystem by altering the quantity of carbon stored (Mendoza-Ponce & Galicia, 2010), location of the carbon stored (Wang et al, 2010; Wei et al, 2012), and stability of the carbon stored in the ecosystem (Eskelinen et al, 2009), because different plant species allocate different quantities of carbon to their respective vegetative parts, such as their roots, stems, leaves, and other anatomical structures.

Fire is often purposely introduced into grassland ecosystems by using prescribed burn treatments (PBT). These treatments are often used to enhance the growth of particular grass species, such as warm season C<sub>4</sub> grasses, and to deter the growth and spreading of unwanted plant species, such as *Juniperus virginiana*, in grassland ecosystems (Taylor, 2008; Knapp et al, 2009; Randall, 2012; Blair et al, 2014). The frequency of fires is critical to hindering the growth and expansion of forest ecosystem succession into grasslands. Ratajczak et al. (2016) observed that sites with PBT conducted over a period smaller than 3 years typically remained as grasslands, but sites that were burned less frequently were more susceptible to ecosystem transitions to shrublands and woodlands. Therefore, the suppression of fire events can increase the probability that a grassland undergoes ecosystem succession, transforming the grassland into a shrubland and eventually a forest. Shrublands and forests can have vastly different carbon allocation schemes compared to a grassland ecosystem (Pinno & Wilson, 2011). For example, forests tend to have relatively more carbon partitioned to aboveground tree biomass and have a low root to shoot ratio, while grasslands tend to have more carbon partitioned belowground into fine roots and have a higher root to shoot ratio (Peichl et al, 2012; Wang et al, 2014).

Another crucial component of grassland management is the timing of a prescribed burn. Appropriate timing of a prescribed burn is critical for suppressing the growth of an unwanted plant community. By applying a burn during a timeframe when these unwanted plants are most susceptible, such as during a part of the plant's life cycle when fire is most damaging to its health, prescribed burns can help regulate the population of particular plant species in an ecosystem (Knapp et al, 2009; McGranahan et al, 2012; Randall, 2012; Towne & Craine, 2014). For example, Towne and Craine (2014) note that traditional spring burn treatments in a prairie ecosystem lead to an increase in the cover of C<sub>4</sub> grasses, such as *Sorghastrum nutans* (Indian grass), while autumn and winter burn treatments led to an increase in the cover of C<sub>3</sub> grasses, such as *Koeleria macrantha* (Junegrass) and plants in the genus *Carex* (sedges). The correct timing and frequency for a prescribed burn is often complicated by weather conditions (Weir, 2011), topography of landscape (Whelen, 1995), moisture content of fuel (McGranahan et al, 2012), and the amount of fuel, which can dictate the intensity and effectiveness of a prescribed fire (Knapp et al, 2009).

Since fires can be important for stimulating the growth of particular plant species in the ecosystem, PBT can be advantageous for enhancing the quantity and quality of certain forage plants that are consumed by many herbivores (Dufek et al, 2014; Raynor et al, 2015). Grazing operations often manage stocks of herbivores that selectively consume specific forage species (Rinehart, 2006; Taylor 2008). Since each herbivore species has their own preference for certain plant species, and because the herbivores have different grazing patterns within an ecosystem (Allred et al, 2011), grazing operations can eventually change the plant community composition in the ecosystem (Taylor, 2008; Spasojevic, 2010). This shift in the plant community composition can be notably different from the more uniform changes in plant community

composition brought about by fire treatments (Collins & Smith, 2006). This further complicates our attempts to understand the relationships between the carbon cycle and land use management in grassland ecosystems. Improper management of grasslands, such as overgrazing, can lead to critically low levels of biomass. This biomass serves as a fuel stock for fire treatments. Low fuel stocks reduce the effectiveness of PBT for controlling the growth of unwanted plants (Delgado-Balbuena, 2013), which increases the probability of unwanted plant encroachment in the ecosystem. In some grazing operations, this encroachment can reduce the forage production needed to feed livestock and the profitability of grazing systems (Simonsen et al, 2015). Therefore, a balance between PBT and grazing operations must be maintained if grassland managers want to protect the ecosystem that sustains their livelihood.

Quantifying the effects that these different management practices, and the many environmental drivers that play a role in implementing these practices, have on an ecosystem's carbon cycle is an important step to improving our understanding of how changes to grasslands can ultimately affect the carbon budget of the biosphere. A myriad of methods and techniques are used to describe the movement of carbon across many temporal and spatial scales. These practices attempt to assist us in describing why and how carbon budgets change over time.

### 1.2 Monitoring carbon exchange in ecosystems

Several methodologies have been formulated to monitor or estimate the net movement of CO<sub>2</sub> in ecosystems. The net movement or exchange of CO<sub>2</sub> in an ecosystem is the resulting difference between CO<sub>2</sub> sequestered by ecosystem photosynthesis and the amount of CO<sub>2</sub> released by ecosystem respiration. Net CO<sub>2</sub> ecosystem exchange has been monitored continuously at several sites around the world using micrometeorological techniques, such as the eddy covariance method (Baldocchi et al, 2012). The eddy covariance approach uses time-

averaged scalar concentration measurements and wind velocity measurements to measure gas or energy fluxes. Due to technological limitations, many past CO<sub>2</sub> flux monitoring campaigns that used eddy covariance were short (Baldocchi, 2003). Advances in instrumentation and data storage capabilities have helped facilitate eddy covariance projects in analyzing CO<sub>2</sub> fluxes year round (Lee et al, 2004). These projects have slowly coalesced into a network of flux measurement towers, located in diverse environments, called the FluxNet (Law, 2005; Baldocchi et al, 2001; Baldocchi et al, 2012). This network has helped scientists investigate the mechanisms that control carbon exchange within many different ecosystems and has helped improve global carbon cycling models (Williams et al, 2009). Nevertheless, even with the increasing availability of ecosystem CO<sub>2</sub> exchange data, our current carbon cycle models are inaccurate, contain many uncertainties, and need further constraints in their input parameters to yield more accurate results (Williams et al, 2009; Welp et al, 2011; Ciais et al, 2013; Collins et al, 2013; Raczka et al, 2016).

The increase in accuracy and precision of current global carbon model estimates will be essential for guiding policy makers in their efforts to create more effective actions and decisions for mitigating global climate change. Many uncertainties stem from issues in upscaling our models of CO<sub>2</sub> exchange from the plant to the ecosystem level (Griffis, 2013), the unknown or unquantified impacts on different components of the carbon cycle brought about by changes in ecosystem land use or management (Ciais et al, 2013), and the unclear effects that increasing CO<sub>2</sub> concentrations and climate change have on CO<sub>2</sub> exchange mechanisms in the soil-plant-atmosphere continuum (Brüggemann et al, 2011; Welp et al, 2011; Ciais et al, 2013). The analysis of stable isotopes of CO<sub>2</sub> could potentially improve our understanding of the biophysical processes responsible for the carbon exchange in ecosystems (Dawson et al, 2002; Griffis, 2013;

Flanagan and Farquhar, 2014) and help to improve our current carbon cycling modeling attempts.

### 1.3 Stable isotopologues of CO<sub>2</sub>

Isotopes are variants of a specific element with different numbers of neutrons in their nuclei. Some isotopes are stable, while others are unstable. Stable isotopes are forms of isotopes that do not undergo radioactive nucleic decay, while unstable isotopes can undergo this decay process. Isotopologues are compounds that contain varying isotopes of different elements. Table 1.1 displays the abundance of CO<sub>2</sub> isotopologues in the free atmosphere. The free atmosphere is defined as portion of the atmosphere in which Earth’s surface friction negligibly influences the motion of air (Stull, 1988). This table shows that the CO<sub>2</sub> isotopologue containing the light stable isotopes <sup>12</sup>C and <sup>16</sup>O is relatively more abundant compared to the other forms, such as <sup>13</sup>C<sup>16</sup>O<sub>2</sub>, <sup>12</sup>C<sup>18</sup>O<sup>16</sup>O, and <sup>12</sup>C<sup>17</sup>O<sub>2</sub>, which occur in very trace amounts. In this literature review, the focus of future discussions will be on the CO<sub>2</sub> isotopologue forms <sup>12</sup>C<sup>16</sup>O<sub>2</sub>, sometimes labeled just as <sup>12</sup>CO<sub>2</sub> or <sup>12</sup>C, and <sup>13</sup>C<sup>16</sup>O<sub>2</sub>, which is sometimes similarly labeled as just <sup>13</sup>CO<sub>2</sub> or <sup>13</sup>C.

**Table 1.1 Common abundance of CO<sub>2</sub> isotopologues present in the free atmosphere, measured by the National Oceanic and Atmospheric Administration’s ESRL division (ESRL-A, 2016)**

Mass	Isotopologues	Abundance
44	<sup>12</sup> C <sup>16</sup> O <sub>2</sub>	98.40%
45	<sup>13</sup> C <sup>16</sup> O <sub>2</sub>	1.19%
45	<sup>12</sup> C <sup>17</sup> O <sup>16</sup> O	0.0748%
46	<sup>12</sup> C <sup>18</sup> O <sup>16</sup> O	0.41%
46	<sup>13</sup> C <sup>17</sup> O <sup>16</sup> O	0.00084%
46	<sup>12</sup> C <sup>17</sup> O <sub>2</sub>	0.0000142%



The analysis of stable isotopes over varying temporal and spatial scales in the environment often involves monitoring the changes in the ratio of isotope or isotopologue concentrations within environmental mediums, such as water, air, soil, and plants. Changes in the abundance of an isotope are often expressed in terms of a delta notation, which is given by:

$$\delta = \left[ \left( \frac{R_{Sample}}{R_{Standard}} \right) - 1 \right] \times 1000 \quad (1.1)$$

where  $\delta$  is the isotopic composition of a given substance (‰),  $R_{sample}$  is the ratio of the abundance of the heavier isotope to the abundance of the lighter isotope in a sample, and  $R_{standard}$  is the isotope ratio of a reference material, such as the Vienna Pee Dee Belemnite sample (V-PDB) for carbon isotopes  $^{12}\text{C}$  and  $^{13}\text{C}$ . For example, the  $\delta^{13}\text{C}$  represents the  $^{13}\text{C}/^{12}\text{C}$  composition of a given material or sample with respect to the standard material V-PDB. A positive  $\delta^{13}\text{C}$  value would indicate that the sample is relatively enriched in the heavier isotope compared to the standard material, while a negative  $\delta^{13}\text{C}$  value would indicate that the sample is relatively depleted in the heavier isotope compared to the standard material.

The isotopic composition of a substance can change over space because several physical, chemical, and biological processes can inherently prefer to consume one isotope or isotopic form over the other forms. Therefore, these processes can change the ratio of isotopes in environmental mediums. For example, the proportion of atmospheric  $\text{CO}_2$  isotopologues has steadily shifted over time (Ciais et al, 2013). This shift in the atmosphere's  $\delta^{13}\text{C}$  has been coined the Suess effect, named after the chemist Hans Suess. Suess was the first to identify this process and its influence on radiocarbon dating (Keeling, 1979). The Suess effect is the result of fossil fuel combustion processes producing  $\text{CO}_2$  that has a more negative  $\delta^{13}\text{C}$  signal, equal to  $-28\text{‰}$ , compared to the average  $\delta^{13}\text{C}$  signal of the free atmosphere, which is roughly equal to  $-8\text{‰}$  (ESRL-B, 2016). The byproducts of fossil fuel combustion therefore make the free atmosphere's

$\delta^{13}\text{C}$  signal more negative over time (Keeling, 1979; Ciais et al, 2013). Interestingly enough, the  $\delta^{13}\text{C}$  value in the fossil fuel combustion products reveal the origins of the fossil fuels to be made up of organic matter that was derived from decomposition of  $\text{C}_3$  plant tissue.

Processes that discriminate against one isotope or isotopologue form over others are labeled as fractionation events. Most fractionation events can be classified into two categories: kinetic fractionation events or equilibrium fractionation events. Kinetic fractionation events occur when irreversible unidirectional reactions or transport processes take place (Kendall & McDonnell, 1998; Griffis, 2013). Such events occur when there is a non-limiting amount of substrate for a reaction, when substrates of a reaction become physically isolated, and because of differences in chemico-physical properties between isotopes (Kendall & McDonnell, 1998; Ghashghaie & Tcherkez, 2012). The mass of an isotope or an isotopologue can play a major role in the substances chemico-physical properties, as well as influence the isotope's kinetic energy (KE) and potential energy (PE) status. For example, let us assume we have two  $\text{CO}_2$  isotopologues:  $^{13}\text{CO}_2$  and  $^{12}\text{CO}_2$ , both moving between two points in space and both are at thermal equilibrium with one another. The isotopologue  $^{12}\text{CO}_2$  has a smaller mass than  $^{13}\text{CO}_2$ . In order for the two isotopologues to have equal KE, while moving an equal amount of distance to reach a point in this space, for instance a reaction site, the heavier isotopologue must have a lower velocity compared to the lighter isotopologue. Thus, the heavier isotopologue will take longer to move the same distance as the light isotopologue moves to reach the reaction site (Cobb, 2012). Potential energy principles can be applied to describe discrimination events against isotopes by examining the energy in the compound's chemical bonds. Heavier isotopes in the compound tend to create stronger chemical bonds between elements compared to lighter isotopes. Lighter isotopes' bonds in compounds are more easily broken, allowing the isotope to

be reacted with at faster rates compared to the heavier isotopes. Thus, under non-equilibrium conditions, the lighter isotope will be reacted with first and the reaction's products will be relatively enriched in the lighter isotope compared to the substrates consumed by the reaction (Cobb, 2012).

Equilibrium fractionation events occur when conditions are present that allow chemical and physical processes to reach an isotopic equilibrium (Kendall & McDonnell, 1998; Griffis, 2013). Although the reaction rates of particular isotopes will be identical in these processes, this does not mean that the isotopic compositions of the processes' products will be consistently identical (Kendall & McDonnell, 1998). This is because the magnitude in which equilibrium fractionation events discriminate against particular isotopologues is dependent on not only the physical properties of the isotopes, like in kinetic fractionation events, but also on other variables, such as temperature or the physical phase-state of the compound. For example, the evaporation of water in a pool tends to result in a change of the isotopic composition of the water vapor leaving the pool's surface and the remaining water in the pool. Typically, the water vapor's isotopic ratio of heavy to light isotopes will become more depleted in the  $^{18}\text{O}$  isotope compared to the source pool, while the remaining pool water will become relatively enriched in  $^{18}\text{O}$ , because the lighter isotopes evaporate more readily than heavier isotopes (Kendall & McDonnell, 1998).

The change in the ratio of the isotopic composition ( $\alpha$ ) between the products and reactants of a reaction that induces a fractionation event is given by:

$$\alpha = \frac{R_{\text{reactants}}}{R_{\text{products}}} \quad (1.2)$$

where  $R_{\text{reactants}}$  is the isotopic composition of the material before the fractionation event takes place, and  $R_{\text{products}}$  is the isotopic composition of the material after a fractionation event occurs.

This change in isotopic composition between products and reactants can also be seen as a discrimination ( $\Delta$ ) against the heavier isotope or a measure of the deviation of  $\alpha$  from unity, and is usually defined by:

$$\Delta = \alpha - 1 \quad (1.3)$$

isotope discrimination of the heavier isotopologue can also be described as the reduction or depletion of the heavier isotopologue during fractionation events (Brüggemann et al, 2011). In particular, solving for the amount of discrimination against the heavier isotopologue present in a given reaction or process ( $\Delta^{13}C$ ) can be accomplished by:

$$\Delta^{13}C = \frac{\delta^{13}C_s - \delta^{13}C_p}{1 + \delta^{13}C_p} \quad (1.4)$$

where  $\delta^{13}C_s$  is the isotopic signature of the carbon compound prior to being used in a chemical reaction or moved in a physical process, while  $\delta^{13}C_p$  is the isotopic signature of the carbon compound after the chemical or physical activities have occurred (Brüggemann et al, 2011).

#### 1.4 Measures of stable isotopes

Measuring the magnitude of discrimination against isotopes is possible by analyzing the changes in the stable isotope concentrations of a sample over time. Differences in the stable isotope concentrations and the magnitude of discrimination values can be very small, thus it is imperative to have accurate and precise measurements of stable isotopes when studying fractionation events and quantifying discrimination processes. This is accomplished using a variety of instruments and techniques. In this section, we will focus on instrumentation that is used to analyze the quantity of isotopes in a given sample.

The traditional method for analyzing isotopic ratios in different samples was accomplished using isotope ratio mass spectrometers (IRMS). These spectrometers can distinguish different isotopes based on their mass-to-charge ratios and motions in a strong

magnetic field (Griffis, 2013). Although IRMS can provide very accurate measurements of isotopic composition of materials, sample preparation and purification is time consuming. This can make IRMS analysis expensive and labor intensive. This is especially true when these systems are interfaced with additional analyzer systems (Ghosh & Brand, 2003; Muccio & Jackson, 2009; Griffis, 2013). Such interfaces include elemental analyzers, gas chromatographs, and liquid chromatographs. Elemental analyzers and gas chromatographs are the most commonly used interfaces, while liquid chromatography may require revisions to become applicable for more isotopic studies (Muccio & Jackson, 2009). The IRMS systems and their interfaces can be used for a variety of projects that do not require high-frequency data measurements and where samples can be analyzed in the laboratory, but coupling this technology with methods that describe the movement of scalars in the atmosphere, such as micrometeorological techniques, can be challenging. This is because of the lack of portability, high maintenance costs, and amount of time committed for sample preparation reduces the potential of these systems to be used with many micrometeorological techniques that require fast temporal resolution measurements of gas concentrations (Griffis, 2013). One alternative to IRMS systems is the use of new optical sensors for isotopic measurements.

Several types of instruments and techniques use optical sensors to monitor the concentrations of isotopic compounds, such as quantum cascade lasers, cavity ring down spectroscopy, Fourier-transform infrared spectroscopy, and tunable diode laser absorption spectroscopy (TDLAS) (Griffis, 2013; Vitiello et al, 2015). Griffis (2013) notes that TDLAS instruments were some of the first to be used in-situ environments. These spectrometers work by exploiting the fact that each isotopic compound of interest has a unique molecular absorption spectrum of energy. These instruments use a laser source to emit radiation at a known intensity,

wavelength, and frequency through a sampling cell. The properties of this radiation match the vibrational resonance properties of the scalar of interest, which allows the radiation to be absorbed by the scalar. At the end of the sampling cell is a laser detector that measures the strength of incoming electromagnetic radiation. The change in the intensity of the electromagnetic radiation spectrum between the laser and detector reveals the quantity of the isotopologues. Recent advances in optical instrument systems have allowed for increased sampling rates that are suitable for the use of micrometeorological methods. In some optical systems, the need for cryogenics to cool the laser is no longer required. This reduces upkeep time and allows for more extensive sampling campaigns, which can be invaluable for monitoring long-term changes in carbon cycling components within an ecosystem as a result of changes to management practices and climate change.

High frequency stable isotope measurements and micrometeorological approaches can be combined to trace the movement of CO<sub>2</sub> in ecosystems and the magnitude of transportation in processes that exchange CO<sub>2</sub> (Griffis, 2013; Flanagan & Farquhar, 2014; Riederer et al, 2015). For example, Wehr et al. (2016) combined these approaches to better quantify the magnitude of ecosystem respiration during the day and night times in a deciduous temperate forest. They found that ecosystem respiration is lower during the day than at night, which is counter to what was originally believed. Combining high frequency stable isotope measurements and micrometeorological approaches together can provide many research opportunities and could prove to be very powerful for expanding our knowledge of the carbon cycle. In studying the movement of carbon in an ecosystem, it must be remembered that many small-scale components, such as plants and soils, contribute to ecosystem exchange and efflux of CO<sub>2</sub>. The next following

sections will focus on the plant and soil components that contribute to the movement of CO<sub>2</sub> in an ecosystem.

### 1.5 Stable isotope discrimination in plants

The stable isotopes of CO<sub>2</sub> have been used to study biophysical CO<sub>2</sub> exchange processes in ecosystems at various space and time scales (Brüggemann et al, 2011; Werner & Gessler, 2011, Werner et al, 2012; Ciais et al, 2013). The <sup>12</sup>CO<sub>2</sub> and <sup>13</sup>CO<sub>2</sub> isotopologues have been investigated extensively at the leaf and plant scales because of how the ratio between the two changes during carbon exchange mechanisms, such as plant stomatal uptake, photosynthesis, and respiration of carbon substrates (Dawson et al, 2002; Sun et al, 2011; Tcherkez et al, 2011; Ghashghaie & Tcherkez, 2012; Ghashghaie & Badeck, 2014).

The relative abundance of <sup>13</sup>CO<sub>2</sub> in plant material is usually lower than the <sup>13</sup>CO<sub>2</sub> concentration of the air outside the plant. This is because there is discrimination against the <sup>13</sup>CO<sub>2</sub> molecules as they move near and through the plant (Table 1.2). For example, there is slight discrimination against the <sup>13</sup>CO<sub>2</sub> molecules as they diffuse through the leaf air-boundary layer interface. This is because the heavier isotopologue has a higher mass and subsequently slower diffusion velocity through the boundary layer, compared to the lighter isotopologues. This discrimination value ( $\Delta^{13}C$ ) against the heavy isotopologues can result in a 2.9‰ decrease in the abundance of <sup>13</sup>CO<sub>2</sub> with respect to the abundance of <sup>13</sup>CO<sub>2</sub> in the ambient air (Brüggeman et al, 2011; Ghasghaie & Tcherkez, 2012). Furthermore, the heavier isotopologue is discriminated against when moving through the leaf stomata, resulting in an approximately 4.4‰ reduction in the abundance of <sup>13</sup>CO<sub>2</sub> compared to the ambient air <sup>13</sup>C signal (Brüggemann et al, 2011; Ghasghaie & Tcherkez, 2012). Additional discrimination occurs as the <sup>13</sup>CO<sub>2</sub> molecules enter the leaf intercellular space and diffuse into the aqueous solution, where they will eventually reach

the enzymatic sites for photosynthesis, resulting in an approximate decrease in their abundance of roughly 0.7‰ and 1.1‰ respectively (Brüggemann et al, 2011).

Different photosynthetic pathways, like C<sub>3</sub> and C<sub>4</sub> pathways, have different degrees of discrimination against <sup>13</sup>CO<sub>2</sub>. Much of the difference between their magnitudes of discrimination is based upon the steps involved in each pathway. For example, C<sub>3</sub> plants rely upon the Calvin cycle to transform CO<sub>2</sub> into organic molecules. This cycle uses the enzyme Rubisco to catalyze the creation of 3-phosphoglycerate molecules. The Calvin cycle acts as a fractionation event as it discriminates against the <sup>13</sup>C isotope by an average of roughly 20‰ to 29‰, compared to the isotopic signal of atmospheric CO<sub>2</sub> (Ghashghaie & Badeck, 2014).

C<sub>4</sub> photosynthesis processes are different from C<sub>3</sub> as they include additional steps before CO<sub>2</sub> is consumed in the Calvin cycle, and the Calvin cycle occurs in the bundle sheath of C<sub>4</sub> plants compared to the mesophyll of C<sub>3</sub> plants. One of the early steps in C<sub>4</sub> plants is the diffusion of CO<sub>2</sub> into the leaf and its movement into the cytoplasm. As CO<sub>2</sub> molecules enter the cytoplasm they undergo a hydration reaction to produce HCO<sub>3</sub><sup>-</sup>. This reaction causes a discrimination against the <sup>13</sup>CO<sub>2</sub> molecule with an approximate value of -9‰ (Tcherkez et al, 2011). The HCO<sub>3</sub><sup>-</sup> molecule is used with phosphoenolpyruvate (PEP) molecules to create oxaloacetate. This process is catalyzed by the enzyme PEP carboxylase (PEP-C). This oxaloacetate is eventually converted into malate, transported to the bundle sheath, and is then broken down into pyruvate and CO<sub>2</sub>. These CO<sub>2</sub> molecules are then concentrated near the site of Rubisco catalysis thereby increasing the chance that even the heavy isotopic compounds will undergo carboxylation. The C<sub>4</sub> photosynthesis pathway thus helps avoid photorespiration losses and reduces overall carbon isotope discrimination, as C<sub>4</sub> plants discriminate against the <sup>13</sup>C isotope by an average of 4 to 15‰, compared to isotope signal of atmospheric CO<sub>2</sub> (Ghashghaie & Tcherkez, 2012; von



Caemmerer et al, 2014). Table 1.2 provides a summary of the location for the major fractionation events and their respective discrimination values.

**Table 1.2 Primary fractionation events and their discrimination values against  $^{13}\text{CO}_2$  during photosynthesis**

Locations of fractionation event	$\Delta^{13}\text{C}$
Leaf air-boundary layer	2.9
Leaf stomata	4.4
Leaf Intercellular air space	0.7
Intercellular aqueous solution	1.1
$\text{C}_3$ photosynthesis	20 – 29
$\text{C}_4$ photosynthesis	4 – 15

Plants that fix carbon using the Crassulacean acid metabolism process, also known as the CAM photosynthetic pathway, discriminate against the  $^{13}\text{C}$  isotope in a unique fashion. CAM plants can show discrimination values similar to  $\text{C}_3$  plants during the daytime, but during the night, the discrimination values are more similar to what is observed in  $\text{C}_4$  plants (Farquhar et al, 1989). This is likely due to the inherent changes in the photosynthetic pathway over the course of a day. At night, the process of storing  $\text{CO}_2$  into the cellular vacuoles as malic acid, a  $\text{C}_4$  acid, acts as a carbon concentrating mechanism much like the  $\text{C}_4$  pathways ability to move carbon into the plant's bundle sheath. During the day, the stored carbon is eventually transformed into  $\text{CO}_2$ , which is used in the Calvin cycle.

Besides photosynthesis, other plant physiological processes discriminate against the  $^{13}\text{C}$  isotope and can ultimately influence the isotopic composition of the plant's respiration efflux, biomass, and other byproducts. For example, glycolysis is a metabolic process that breaks down complex organic molecules into  $\text{CO}_2$  and energy. In this process, there are a series of conversions between many intermediate molecules. Each conversion can create fractionation

events, such as the conversion of 3-phosphoglyceraldehyde to 1,3-bisphosphoglyceric acid. This conversion step tends to create a discrimination value of approximately 5‰ (Tcherkez et al, 2011). Werner and Gessler (2011) note that there are three major potential mechanisms that can influence the variability of the  $\delta^{13}\text{C}$  signal in plant, soil, and ecosystem respired  $\text{CO}_2$ . The first factor they mention is that changes in the substrates used for plant or soil microbial metabolism can alter the  $\delta^{13}\text{C}$  signal of the respired  $\text{CO}_2$ . Secondly, they mention that strength of different metabolic pathways can add to the variability of the  $\delta^{13}\text{C}$  signal in respired  $\text{CO}_2$ . Lastly, variations in the ecosystem  $\delta^{13}\text{C}$   $\text{CO}_2$  signal can occur because distinct components of the ecosystem, such as the soil and plants, contribute different magnitudes of  $\text{CO}_2$  fluxes and their  $\delta^{13}\text{C}$  signals at different times. Such processes are discussed more extensively in Werner and Gessler (2011), as well as by Tcherkez et al. (2011).

Many carbon exchange mechanisms and their magnitudes of discrimination against particular isotopes can change because of several factors. For example, Ghashghaie and Tcherkez (2012) note that the  $^{13}\text{C}$ -signal in photosynthetic products can vary between plant species, varying plant growth stages, and environmental conditions. Another example is that leaf growth and aging creates a change in the physical properties of the leaf, such as its thickness. This increase in leaf thickness can enhance the discrimination against heavier  $\text{CO}_2$  isotopologues, because with increases in leaf thickness comes increases in mesophyll thickness and a subsequent decrease in mesophyll diffusion conductance (Flexas et al, 2012, Barbour et al, 2016). A larger mesophyll space means that the  $\text{CO}_2$  molecules must travel a greater distance to reach the enzymatic sites for carboxylation. Thus, there will be likely be a more discrimination against the heavier  $\text{CO}_2$  isotopologues (Kodama et al, 2011; Flexas et al, 2012; Werner et al, 2012). Additional research is still needed to address knowledge gaps in fractionation events

during post-carboxylation, decarboxylation, and C<sub>4</sub> photosynthetic pathway processes (Werner et al, 2012; von Caemmerer et al, 2014; Ghashghaie & Badeck, 2014).

### 1.6 Isotope exchange in soils

Soils play a large role in the global carbon cycle. Soils are the largest carbon pool in the terrestrial biosphere and contain the second largest carbon exchange pathway between the atmosphere and the terrestrial biosphere (Raich & Schlesinger, 1992; Scharlemann et al, 2014). Despite the vast amount of research on soils, there is a lack of understanding on the formation and distribution of global soil carbon stocks (Guo & Gifford, 2002; Wang et al, 2010; Shi et al, 2012; Torn et al, 2013), the carbon exchanges processes within soil systems (Wang & Hsieh, 2002; Bond-Lamberty & Thomson, 2010), and how soils systems are altered under changing environmental conditions, plant communities, and management practices (Raich & Schlesinger, 1992; Bahn et al, 2008; Liu et al, 2009; W. Wang et al, 2013; Scharlemann et al, 2014; Beverly & Franklin, 2015). The analysis of carbon compounds in soil systems provide new insights into the mechanisms governing carbon exchange in the soil (Amundson et al, 1998). This section will provide examples of how isotope research has helped study the soil carbon cycle thus far and the future of isotopic analysis applications to soil systems research.

Stable CO<sub>2</sub> isotope analysis has become a great tool for understanding the biophysical drivers of soil CO<sub>2</sub> transport dynamics and for identifying the major contributors of soil CO<sub>2</sub> efflux (Nickerson et al, 2014). The three primary sources of soil CO<sub>2</sub> efflux are the autotrophic, heterotrophic, and rhizosphere respiration pathways. The heterotrophic component of soil respiration originates from microbial decomposition of carbon materials, such as organic matter, while the autotrophic component of soil respiration is primarily attributed to plant root respiration, but can also include organisms that are in a symbiotic relationship with plant roots.

Rhizosphere respiration is debatably classified as a part of either the autotrophic or heterotrophic pathways (Kuzyakov, 2006). For this review, the rhizosphere component will be discussed as an independent pathway.

These respiration pathways can produce different  $\delta^{13}\text{C}$  signals over time, because their signals are highly dependent upon the isotopic composition of the carbon substrates that are being consumed. For instance, in autotrophic soil respiration the main source of carbon substrates for root respiration is the aboveground carbon assimilates synthesized by the plants. These substrates are influenced by different biochemical pathways before reaching the root sites of respiration. For example, the  $\delta^{13}\text{C}$  signal of the autotrophic soil respiration can majorly depend on the plant species and environmental factors (Ghashgaie & Badeck, 2014). This is also true for the carbon exudates that are used in the rhizosphere respiration pathway (Zhu & Cheng, 2011). The  $\delta^{13}\text{C}$  signature of the heterotrophic respiration soil efflux relies upon the  $^{13}\text{C}$  composition of the soil organic matter and the microbial community that will use the organic matter's substrates in metabolic pathways. The large variety of microbial decomposers in soils can also influence the  $\delta^{13}\text{C}$  signal in heterotrophic  $\text{CO}_2$  effluxes, because each microbial species uptakes and respire the carbon substrates through their own unique physiological mechanisms (Henn & Chapela, 2000; Garcia-Pausas & Paterson, 2011).

In order to improve and validate current soil carbon partitioning models, there must be continued attempts at untangling respiration and total  $\text{CO}_2$  efflux components (Albanito et al, 2012). Bowling et al. (2015) remarks that the differences in the  $\delta^{13}\text{C}$  isotopic signals between the soil respiration pathways in established ecosystems, in which plants and soil carbon have similar isotopic compositions, might be too small to be useful for distinguishing the source components in the total respiration efflux  $\delta^{13}\text{C}$  signal. Such observations are usually different compared to

non-established ecosystems, such as agricultural ecosystems, because there might be drastic differences between the isotopic signals of the respiration components. For example, Fassbinder et al (2012) showed that the autotrophic and heterotrophic soil respiration components contributions to an agricultural ecosystem's respiration could be separated using isotopic analysis and micrometeorological measurements. They observed that during the soybean and corn growing seasons, the measured ecosystem soil respiration  $\delta^{13}\text{C}$  signals were close to the  $\delta^{13}\text{C}$  values that are commonly associated with the respective plant's photosynthetic pathway, while during the springtime the  $\delta^{13}\text{C}$  signal of the ecosystem respiration was close to the expected range of  $\text{C}_3$  plants regardless of the plants growing at the time. They hypothesized that during the springtime the soil microbial decomposition of  $\text{C}_3$  plant residue was contributing strongly to the net ecosystem  $\text{CO}_2$  efflux.

Many other factors, such as the physical properties of soils and environmental conditions, are believed to influence the  $\delta^{13}\text{C}$  signal of soil efflux  $\text{CO}_2$  (Bowling et al, 2008). Uncertainty exists in isotopic analysis at the soil system scale because there are knowledge gaps on the extent in which environmental variables affect  $\delta^{13}\text{C}$  signal temporal dynamics, such as precipitation events (Unger et al, 2012) and periods of drought (Balogh et al, 2015). Bowling et al. (2015) discussed that previous studies observed diel fluctuations in the isotope composition of the soil  $\text{CO}_2$  efflux. These studies attributed the changes in isotopic composition to changes in environmental forcing, but Bowling et al. (2015) did not find similar results based on experimental data collected in a subalpine forest. Balogh et al. (2015) argues that drought events are one case of environmental forcing that can change the magnitude and isotopic signals of soil system  $\text{CO}_2$  efflux. One important conclusion of their study is that the autotrophic respiration fluxes were hampered by drought conditions to a greater extent than the heterotrophic fluxes. It

is possible that under normal, non-drought conditions, the isotopic signals could be too similar to be used in isotope analysis. In reality, soil moisture content can vary over the course of a growing season for many ecosystems. More research is needed to determine if there is a strong correlation between soil moisture content and the strength of the autotrophic and heterotrophic CO<sub>2</sub> δ<sup>13</sup>C signals. In addition, there is a need for research to clarify the extent that other physical and environmental factors play on the variability of the soil CO<sub>2</sub> efflux δ<sup>13</sup>C signal over time.

Currently, soil CO<sub>2</sub> efflux is often measured at the soil surface using chambers. These measured fluxes are a result of the contributions of different sources at different depths in the soil, which means the individual contributors' δ<sup>13</sup>C signals will be convoluted. Future soil system isotopic analysis research will likely use online subsurface sampling techniques to discern the strength and isotopic signals of soil CO<sub>2</sub> efflux sources at various soil depths and temporal scales (Goffin et al, 2014; Gangi et al, 2015). Although we can attempt to use the heterotrophic and autotrophic isotopic signal analysis to separate the contributors to the surface CO<sub>2</sub> efflux, the subsurface sampling method has the potential to enhance our soil CO<sub>2</sub> flux partitioning approaches. In addition, more detailed sampling approaches could improve our understanding of how environmental drivers affect the δ<sup>13</sup>C composition of the soil CO<sub>2</sub> flux. This future technique could prove very valuable for improving current land surface and carbon cycle models.

### 1.7 Carbon isotope analysis in ecosystems

Isotope analysis can be useful for studying carbon exchange processes at the ecosystem scale, such as identifying the contributions that C<sub>3</sub> and C<sub>4</sub> plants have on the ecosystem respiration. For example, Shimoda et al. (2009) measured the flux of CO<sub>2</sub> and the δ<sup>13</sup>C signal of atmospheric CO<sub>2</sub> and plant biomass samples from a mixed grassland ecosystem. With these data, they were able to determine the proportion of C<sub>3</sub> and C<sub>4</sub> plants contributing to the ecosystem CO<sub>2</sub>

respiration. They found that C<sub>4</sub> plants contributed roughly 63-67% to the ecosystem's respiration during the months of October and November. Isotope analysis can also be used to separate the net ecosystem CO<sub>2</sub> exchange (NEE) into its assimilation and respiration components. Bowling et al. (2001) performed flux partitioning by collecting CO<sub>2</sub> gas samples in flasks at two heights within a deciduous forest. These gas samples were examined for their isotopic composition and their data were used in a series of equations that partitioned the NEE data, collected by eddy covariance instruments, over the duration of the experiment. Though they felt that there were sufficient data to successfully complete their partitioning attempts, they concluded that direct eddy covariance measurements of the <sup>13</sup>CO<sub>2</sub> flux would be necessary in the future.

Other attempts at combining isotopic analysis with micrometeorological techniques used different instruments, such as TDLAS. These systems often required a fair amount of time committed to instrument upkeep, such as for refilling the cryogen that cools the instrument's laser (Griffis, 2013). With advances in isotope gas sampling analysis and environmental parameter measurement instruments, we can more effectively combine powerful micrometeorological techniques with isotopologue analysis. Three techniques that will be addressed in this section are used to predict or monitor the concentration of scalars in an ecosystem. These are Keeling plots, eddy covariance, and the isotope flux ratio analysis.

A Keeling plot is a technique that can be used to estimate the concentration of a scalar in an ecosystem based on the assumption that mass is conserved during the exchange or movement of scalars between two stocks or reservoirs (Köhler et al, 2006). In terms of CO<sub>2</sub>, the commonly used reservoirs used in this technique is the CO<sub>2</sub> concentration emitted from a source component and the concentration of CO<sub>2</sub> in the background. The addition of these two concentrations gives us the atmospheric CO<sub>2</sub> concentration levels. This technique can accompany isotopic analysis,

allowing researchers the ability to estimate  $\delta^{13}\text{C}$  values for a given  $\text{CO}_2$  concentration based on a linear regression approach (Pataki et al, 2003). Two basic assumptions are made when using this technique. Köhler et al. (2006) states that the first assumption is that the ecosystem or system of reservoirs being examined can only contain two reservoirs. Secondly, they state that the isotopic ratio of carbon added by a source does not change during the time of observation. This linear modeling approach does have inherent disadvantages that can limit its application in particular studies. Pataki et al. (2003) notes that turbulence can eliminate the buildup of  $\text{CO}_2$  profiles and that advection can bring in air masses that have passed over ecosystems that are not of interest, thereby adding  $\text{CO}_2$  with an isotope signal that is not wanted. Such phenomena could lead to erroneous Keeling plot mixing lines and inaccurate results. Additionally, Keeling plots have traditionally used flask sampling approaches to collect gas samples. This approach significantly limits the amount of data points that are available for analysis because time is needed to collect the gas samples, prepare said samples, and run it through an IRMS system. Though IRMS systems have some applications in a few micrometeorological methods, such systems are not yet fully capable of being used in high frequency eddy covariance measurements (Griffis, 2013).

Eddy covariance is one micrometeorological technique used to measure  $\text{CO}_2$  exchange in ecosystems, and can be useful for isotopic analysis. With great advancements in technology during the 90's, such as the advancements in sonic anemometers, gas analyzers, personal computers, and dataloggers, the eddy covariance method has become the most popular micrometeorological technique used to quantify  $\text{CO}_2$  and energy fluxes at the ecosystem scale (Baldocchi, 2003). This technique is based on the fact that turbulent motion in the atmosphere (eddies) transports matter and energy between the land surface and the atmosphere. The covariance between the changes in the concentration of scalars with the change in direction or



motion of these eddy can be monitored overtime to reveal the net movement of a scalar in or out of an ecosystem, in terms of the flux density of that scalar.

The use and accuracy of eddy covariance flux measurements relies on several assumptions. Burba (2013) states that the measurements being made are assumed to represent the area of interest. To do this, he says that the upwind fetch and footprint of fluxes must be adequate in length and size to ensure that the scalars being measured are coming from the area of interest. Next, we must assume that the instruments being used can detect small changes in the concentrations of the scalars of interest. Other assumptions include that the terrain is horizontal and uniform, air density fluctuations are negligible, and flow divergences and convergences are negligible. One other common assumption that must be addressed is that the instruments should be placed just high enough above the canopy to properly sample ecosystem fluxes in the boundary layer of interest (Burba, 2013). Considerations about the isotopic measurement instrument must be addressed as well. Isotopic measurement instruments are essentially closed path gas analyzers. As such, several factors like the tube material, tube dimensions, air flow rate, and inline filters, must be examined to prevent excessive tube attenuation of gas species and to help observe high quality data (Massman & Ibrom, 2008; Haslwanter et al, 2009; Munger et al, 2012; Burba, 2013). The eddy flux ( $F$ ,  $\text{kg m}^{-2} \text{s}^{-1}$ ) of a given scalar by using the following equation:

$$F = \overline{\rho_{air}} \overline{w'c'} \quad (1.5)$$

where  $\overline{\rho_{air}}$  is the time averaged dry air density ( $\text{kg m}^{-3}$ ) and  $\overline{w'c'}$  is the time averaged covariance of vertical wind speed ( $w$ ,  $\text{m s}^{-1}$ ) with the gaseous scalar mixing ratio ( $c$ ,  $\text{mol}_{\text{gas}} \text{kg}_{\text{dry air}}^{-1}$ ).

Recent studies have combined eddy covariance and isotopic measurements to study isotopic exchanges at the ecosystem scale (Griffis et al, 2008; Wehr et al, 2013). Wehr and

Saleska (2015) used stable carbon isotopes to partition the net ecosystem-atmosphere exchange of CO<sub>2</sub> in a temperate deciduous forest. They measured the flux of the net CO<sub>2</sub> ecosystem exchange, its isotopic ratio (<sup>13</sup>C/<sup>12</sup>C), and the isotopic ratio of the non-foliar respiration. This study shows that some of the individual flux components could be identified and quantified. They believe that this quantifying helped reduce errors and biases in their data, as well as create more confidence in the precision of their measurements.

Sturm et al. (2012) measured CO<sub>2</sub> fluxes and their isotopic ratios using eddy covariance over a mixed forest canopy, but determining ecosystem discrimination on hourly or diurnal time scales proved to be a challenge in this ecosystem (Sturm et al, 2012). They found that their eddy covariance measurements had a low signal-to-noise ratio and an uncertainty equal to 10‰, which meant that small variations in the isotopic signals could not be sufficiently resolved. They believe that they could improve upon the signal-to-noise ratio by placing the sensors closer to or within the canopy so that they would be able to measure larger fluctuations in concentration in comparison to the free atmosphere. Under certain conditions, such as short or dense canopies, their recommendation may not be feasible because current eddy covariance instruments are too bulky to be deployed within short or dense canopies. Eddy covariance can also encounter additional issues when measurements are taken within a canopy. These issues are related to the instrumentation's inability to measure eddy motions with time scales faster than the instrument's response time and is related to the inability of the instrument to measure eddy motion that occupies a volume smaller than the sampling volume of the instrument (Burba, 2013). These small eddies form from the breakdown of larger eddies by drag forces created by the canopy and surface. This drag results in a transfer of momentum from the eddy turbulence to the surface layer elements, often called a momentum sink, which results in a reduction in the turbulent

kinetic energy (Wilson, 1989). The reduced kinetic energy results in a decrease of the eddy's size. As a result of these interactions between the canopy and turbulence, there is a higher probability for encountering the small eddies when coming closer to and deeper within the canopy (Burba, 2013), thereby making eddy covariance measurements unreliable in such cases. Thus, an alternative method is needed to measure the movement of scalars.

One commonly used alternative to eddy covariance measurements is the flux-gradient methodology. To estimate flux-gradient values, we can use the following equation (Meredith et al, 2014):

$$F_C = -K_m \bar{\rho}_n \frac{d\bar{C}}{dz} \quad (1.6)$$

where  $F_C$  is the flux of a scalar ( $\text{kg}_{\text{scalar}} \text{m}^{-2} \text{s}^{-1}$ ),  $K_m$  is the eddy diffusivity coefficient ( $\text{m}^2 \text{s}^{-1}$ ),  $\bar{\rho}_n$  is the time-averaged molar density of dry air ( $\text{kg}_{\text{dry air}} \text{m}^{-3}$ ), and  $d\bar{C}/dz$  is the mean concentration of the scalar for a given height at  $dz$  ( $\text{kg}_{\text{scalar}} \text{kg}^{-1}_{\text{dry air}} \text{m}^{-1}$ ). Traditional flux-gradient approaches rely upon the Monin-Obukhov similarity theory to derive a relationship between concentration gradients and fluxes of scalars (Simpson et al, 1998; Meredith et al, 2014; Monson & Baldocchi, 2014). Though this technique can prove to be a useful alternative in settings where eddy covariance measurements are not feasible, the technique can have several challenges. Notably, the scalar transport coefficients in the similarity theorem can often be underestimated in the roughness sublayer (Simpson et al, 1998; Monson & Baldocchi, 2014). The roughness sublayer is an atmospheric layer that is heavily influenced by the canopy surface. Sampling within this layer is inherently difficult because of the complex and often-chaotic nature of turbulence flow through the heterogeneous canopy elements (Monson & Baldocchi, 2014). Another problem with the flux-gradient technique is that several assumptions are made when using the flux-gradient relationships. One of the main assumptions of this approach is that the length scale of turbulence

transport of the scalars is smaller than or nearly equal to the length scale of the concentration gradients. This assumption can be invalidated because in some canopies there are large eddies that sweep away the concentration gradients, thereby creating a counter-gradients, which makes for unrealistically large eddy diffusivity values (Monson & Baldocchi, 2014). Due to these concerns, this technique is sometimes used in the inertial sublayer, the atmospheric layer just above the roughness sublayer. However, according to Smith and Cresser (2003), gradients in this sublayer might become too small and difficult to measure. Therefore, careful consideration regarding the heights of concentration measurements used to conduct flux-gradient measurements must be made.

The flux-gradient relationships have been adapted for isotopic studies for finding the isotopic flux ratio (Griffis et al, 2004), which is described as:

$$\frac{F^{Heavy}}{F^{Light}} = \frac{-(K \frac{\bar{\rho}_a}{M_a}) \frac{d[Heavy]}{dz}}{-(K \frac{\bar{\rho}_a}{M_a}) \frac{d[Light]}{dz}} \quad (1.7)$$

where  $F^{Heavy}/F^{Light}$  is the ratio of the net fluxes of the heavier and lighter isotopologues respectively (dimensionless), such as  $^{13}\text{CO}_2$  and  $^{12}\text{CO}_2$ ,  $\bar{\rho}_a$  is the time averaged air density ( $\text{kg m}^{-3}$ ),  $M_a$  is the molecular mass of dry air (kg),  $\frac{d[Heavy]}{dz}$  and  $\frac{d[Light]}{dz}$  are the time averaged concentration gradients. Equation 1.7 is often used between discrete samplings inlets and can be represented using the following equation:

$$\frac{F^{Heavy}}{F^{Light}} = \frac{-(K \frac{\bar{\rho}_a}{M_a}) \overline{[Heavy]_{z2} - [Heavy]_{z1}}}{-(K \frac{\bar{\rho}_a}{M_a}) \overline{[Light]_{z2} - [Light]_{z1}}} \quad (1.8)$$

where the expressions  $\overline{[Heavy]}$  and  $\overline{[Light]}$  are the time averaged concentration values between two heights,  $z_2$  and  $z_1$  respectively. Equation 1.8 can be simplified even further by assuming that the eddy diffusivity for each isotopologue is the same, and that the dry air density and molecular

weight do not change substantially over the height that the air samples are taken. Based on the previous assumptions, equation 1.9 can be rewritten as follows:

$$\frac{F^{Heavier}}{F^{Lighter}} = \frac{[Heavy]_{z2} - [Heavy]_{z1}}{[Light]_{z2} - [Light]_{z1}} \quad (1.9)$$

The ratio between heavier and lighter isotope fluxes is usually expressed in delta notation and is given by:

$$\delta_F = \left( \frac{F^{Heavier} / F^{Lighter}}{R_{standard}} - 1 \right) \quad (1.10)$$

where  $\delta_F$  is the isotopic composition of the flux (‰) and  $R_{standard}$  is the isotopic composition of a standard material, e.g. VPDB.

As shown in the derivation of the isotopic flux ratio equation, when converting the flux-gradient variables to the isotopic flux ratio equation we cancelled out many of the K-theory terms. This allows the isotopic flux ratio method to not be as hindered by the weaknesses of the flux-gradient approach as was previously discussed in this section. However, it must be noted that the implementation of the isotopic flux ratio method, the flux-gradient approach, and eddy covariance can encounter difficulties when concentration gradients are small (Griffis et al, 2008).

The isotopic flux ratio method has several advantages over the previously mentioned combination of eddy covariance and isotopic analysis. With flux-gradient approaches (Meredith et al, 2014) and its derived isotopic flux ratio methodology, there is no need for fast response instruments to obtain quality data. Fast response measurements could be useful, though, for detecting rapid shifts in isotopic compositions of respiration components. Santos *et al* (2012) evaluated the use of the isotopic flux ratio method in a forest ecosystem and compared their data with data from a modified Keeling plot, a more traditional means of estimating the isotopic ratio of CO<sub>2</sub> for an ecosystem flux. They found that both methods had similar agreement in their  $\delta^{18}O_F$  and  $\delta^{13}C_F$  results, but the isotopic flux ratio method retained a greater amount of data.

Another advantage of the isotopic flux ratio method over other approaches is that it can be used to sample several areas of interest with the same gas analyzer. For instance, Glenn et al. (2011) used the isotopic flux ratio method to identify the dominant sources of respiration effluxes in an agricultural system. Their research site consisted of four experimental plots. Two of the plots had intensive tillage treatments and the other two had reduced tillage treatments. Gradients of CO<sub>2</sub> isotopologue were measured above those plots using a multiport sampling system connected to a tunable diode laser trace gas analyzer. The gas sampling campaigns occurred during the fall season and during the spring season right after the corn harvest. The organic matter in these plots was primarily composed of C<sub>3</sub>-based organic matter. As explained in section 1.4, the C<sub>3</sub> and C<sub>4</sub> crops will have different  $\delta^{13}\text{C}$  values in their biomass. Because of the unique  $\delta^{13}\text{C}$  values in each crop's biomass, Glenn et al. (2011) were able to estimate how much the decomposition of C<sub>4</sub> materials contributed to the total respiration flux for each plot throughout the study. They found that approximately 70% of the total respiration flux originated from the decomposition of C<sub>4</sub> materials during the fall of 2006. This value dropped to 20 to 30% during the following spring of 2007.

Drewitt et al. (2009) investigated the potential impacts that conventional tillage systems and no-till systems had on the soil and ecosystem respiration isotopic ratio signals. They used a tunable diode laser to measure concentrations of <sup>12</sup>CO<sub>2</sub> and <sup>13</sup>CO<sub>2</sub> above four plots. Two of these plots received a conventional tillage treatment, while the other two received a no-tillage treatment. Recent crop rotations consisted of winter wheat, corn, soybeans, and corn again. Drewitt et al. (2009) found that the plots that mixed corn residue into the soil using tillage had respiration  $\delta^{13}\text{C}$  values more characteristic of the C<sub>4</sub> signature compared to the no-till field, but overtime the  $\delta^{13}\text{C}$  signals became more depleted. This revealed that carbon substrates from the

C<sub>4</sub> residues became more scarce as time progressed. Thus, microbial decomposers began to target the C<sub>3</sub> soil organic matter.

The techniques mentioned so far are not suitable for studying the isotopic exchange within plant canopies. Novel approaches in studying isotopic exchange, such as inverse Lagrangian analysis techniques, could be an alternative to measuring the isotopic exchange within plant canopies. Lagrangian mechanics in classical fluid and field theory are different from Eulerian mechanics. Eulerian mechanics tend to use a static framework for describing or studying fluid motion and physical characteristics at a specific location in space and time (Monson & Baldocchi, 2014), whereas Lagrangian mechanics uses a moving framework to follow the flow of individually dispersed fluid particles or parcels (Jacques et al, 2012). Following these scalars allows the observer to describe the physical characteristics of the scalar for many trajectories over time. The Eulerian framework is commonly used for described the concentration of scalars at a fixed point and time (Jacques et al, 2012), which is typical when conducting micrometeorological observations of scalars. With the Lagrangian approach, turbulence statistics are used to predict the history and fate of the air parcel's trajectory (Warland & Thurtell, 2000), which can lead to a better description of processes within plant canopies.

Lagrangian analysis techniques could provide an alternative to traditional micrometeorological methods for studying the isotopic exchange within plant canopies and to separate the contributions of soil and plants to the net isotopic flux. Santos et al. (2012) compared the results of a Lagrangian dispersion analysis and isotopic flux ratio method in monitoring and inferring changes in isotopic concentration values in a forest canopy. They found that a backwards Lagrangian analysis held potential for further enhancing the studies of isotopic exchange in ecosystems, but required further evaluation under varying turbulence conditions.

## 1.8 Chapter outlines and concluding remarks

Two additional chapters are included in this thesis. The next chapter is dedicated to describing the performance analysis of a novel tunable diode laser (TGA200A). An assessment is completed that described the performance of the instrument and the potential benefits in using buffering volumes to mix the analyzer's air samples. In addition, an analysis into the number of sampling inlets affecting partial sampling time errors was completed. These evaluations are critical to ensuring high quality data is collected by the instrument and is helpful for understanding the strengths and weaknesses of the sampling system when used for gaseous isotopologue studies.

The last chapter describes the use of this evaluated TGA200A instrument for in-situ measurements of two isotopic variants of CO<sub>2</sub> within a tall-grass prairie ecosystem. As discussed in section 1.1, these ecosystems are major influencers of the global carbon cycle. Use of isotopic analysis could help improve our understanding of carbon exchange mechanisms in these ecosystems. Such research is needed to study the changes in carbon exchange because of changes to plant community composition, which is often brought about by different management strategies and techniques. In this study, prescribed burn treatments and grazing operations were the main management strategies used to alter plant community composition. Details about the site descriptions, how the TGA200A sampling system was setup, and how some environmental parameters likely impacted our isotopic signals will be discussed.

Updating, revising, and ensuring quality checks in the micrometeorological methods, isotopic analysis techniques, and their implementations will often add more complex and rigorous mathematics. Such an increase in the difficulty of analysis may be necessary to accurately resolve the strength of CO<sub>2</sub> sources and sinks in an ecosystem. This document has



touched on the importance for increasing research in grasslands and has highlighted the past research in forest ecosystems. However, many other ecosystems, ecotones, and biomes need to be investigated using the combined stable isotope analysis and micrometeorological approach, because all ecosystems encompass the global carbon and energy cycles. All the advances in techniques, methodologies, instruments, and other principles for studying the carbon cycle in the environment will be key to validating our future climate change models and their scenario predictions.

## **Chapter 2 - Performance evaluation of a multiport sampling system to measure vertical gradients of CO<sub>2</sub> isotopes at the ecosystem scale**

### 2.1 Introduction

The combination of micrometeorological techniques and stable isotope analysis has led to more accurate, precise, and frequent measurements of CO<sub>2</sub> components at the ecosystem scale (Bowling et al, 2008; Santos et al, 2012; Griffis, 2013, Wehr & Saleska, 2015). Recent advancements in stable isotope optical sensors will provide great improvements over traditional approaches that require labor-intensive sampling preparation, slow measurement frequencies, and limited sampling campaign intervals (Griffis, 2013). This new generation of sensors will surely help advance our ability to study plant, canopy, and ecosystem responses to climate change (Griffis, 2013).

Tunable diode laser trace gas analyzers using thermoelectric cooling are an example of this new generation of optical sensors. These gas analyzers use spectroscopic principles to measure the concentration of isotopes of interest passing through the instrument's sampling cell. The instrument's laser generates electromagnetic radiation (EMR) over a very narrow range of the electromagnetic spectrum, with frequency and wavelength properties matching each isotopologue's unique vibrational resonance frequencies (Griffis, 2013). This EMR is split and sent through a reference cell and a sample cell. The energy that is not absorbed by the isotopologue species of interest in the reference cell and sampling cell eventually travels to a detector at the end of each respective cell path. The difference in EMR emitted by the laser and EMR sensed by the detector, as described by absorption and transmission spectral analysis, is proportional to the quantity of the isotopologue of interest.

Isotope measurement systems require high precision to measure very small changes in isotope concentrations in natural environments. Instrument noise can limit the instrument's ability to detect small changes in concentration of isotopes at ecosystems over a given time period. The use of sufficiently long averaging periods can reduce some instrument noise. Statistical approaches, such as Allan deviation analysis, can be used to evaluate instrument precision and its relationship with the averaging time. This analysis has been used in previous studies to evaluate the precision of isotope systems (Richter et al, 2009; Tuzson et al, 2011; Sturm et al, 2012). Therefore, this analysis could provide means to find the optimum averaging time interval with the least deviation, and therefore most precision, in concentration signals for a sampling system.

Another source of measurement uncertainty arises from high frequency fluctuations in concentration measurements. These sampling errors reduce the signal to noise ratio, making it difficult to measure the small gradients of gas concentration often required to study isotope exchange in ecosystems. Buffer volumes have been used to reduce natural high frequency fluctuations in concentration signals and improve the ability of sampling systems to measure very small gradients of concentration (Meredith et al, 2014; Cescatti et al, 2016). Evaluating the effectiveness of these buffer volumes for a particular sampling system is crucial to improve the detection limits of gas sampling systems.

Another major source of measurement uncertainty stems from partial sampling time errors. This source of uncertainty is particularly important for multi-port sampling systems, which use manifolds to measure more than one air inlet using a single gas analyzer. Each inlet is sampled during a relative short time interval, ranging from a few seconds to a couple of minutes, until the manifold redirects the airflow to the next subsequent air inlet. The amount of time spent

purging the system in-between air inlet switching creates a notable loss of inlet sample data and an increase in the chance of measurement errors. This measurement approach has the advantage of eliminating possible bias that may arise if different instruments were used to measure each air intake. However, errors associated with partial sampling time can be important when sampling multiple intakes with a single instrument. There is a need to characterize these partial sampling time errors and to evaluate the impact that the number of inlets being sampled can have on sampling errors.

The objective of this study was to evaluate the performance of a new tunable diode laser trace gas analyzer (TGA200A, Campbell Scientific, Logan, UT, USA) and a custom-made multi-port sampling system. Two distinct TGA lasers were analyzed for their deviation and precision by using an Allan deviation approach. An additional test was conducted to examine the effectiveness that a buffering volume has on reducing high frequency fluctuations of the  $^{12}\text{CO}_2$  and  $^{13}\text{CO}_2$  mixing ratio measurements. The standard deviation values of gas concentration measurements that went through the buffering volume were compared with air streams not passing through a buffering volume. Sampling errors associated with partial sampling time were also evaluated based on number of inlets and if air was mixed using the buffer volumes.

## 2.2 Methodology

### 2.2.1 Instrumentation setup

Mixing ratios of the stable isotopologues  $^{13}\text{CO}_2$  and  $^{12}\text{CO}_2$  were measured at 10 Hz using a tunable diode laser trace gas analyzer (TGA200A, Campbell Sci., Logan, UT, hereafter TGA). The precision and stability of two laser sources were examined. One laser measures the mixing ratio of  $^{13}\text{C}^{16}\text{O}_2$  and  $^{12}\text{C}^{16}\text{O}_2$ , while the other laser measures the mixing ratio of  $^{13}\text{C}^{16}\text{O}_2$ ,  $^{12}\text{C}^{16}\text{O}_2$ , and  $^{12}\text{C}^{18}\text{O}^{16}\text{O}$ . These two lasers will be referred as the dual-band and tri-band laser,

respectively. One reference tank provided CO<sub>2</sub> at a concentration of 2500 ppmv when using the dual-band laser, while another tank provided CO<sub>2</sub> at a concentration of 10,000 ppm when using the tri-band laser. The gas from these tanks were drawn through the TGA reference cell at 20cm<sup>3</sup> min<sup>-1</sup>. Nitrogen gas was used to purge an air gap between the reference and sample cells and their respective detectors. A calibration of the TGA system was performed using NOAA standard CO<sub>2</sub> tanks, with a span of 340 ppmv to 540 ppmv.

Gas samples are drawn into the gas analyzer's sampling cell from a custom-built multiport manifold sampling system using a vacuum pump (XDD1, Edwards, Crawley, UK). The multiport manifold and TGA were both connected to a datalogger (CR3000, Campbell Sci.). The datalogger controlled the manifold valves that directed gas samples through the analyzer and bypass. Over time, the manifold would switch valve positions to allow the Edwards vacuum pump to pull air through a different inlet gas stream than the previously analyzed inlet gas stream. Gas samples coming from inlets that are not being measured in a given interval are directed to a bypass port on the manifold. These gas samples are drawn through the exhaust port by using another pump (DOAV502, Gast Manufacturing, Benton Harbor, MI). The datalogger stored the gas analyzer's isotopic and diagnostic data onto a memory card. These files were transferred to the laboratory server and converted to ascii format to be analyzed.

Calibrations tanks and the buffer volume apparatus, also called an air mixing apparatus, were also connected to the multiport manifold system. The buffering volume apparatus (Figure 2.1) consisted of eight 750 mL stainless steel flasks. Each gas-sampling inlet stream has their own 750 mL stainless steel flask, excluding the tubing connected to the reference and calibration tanks.



**Figure 2.1 – A picture of the buffering volumes (metallic flasks) used with the multi-port sampling system.**

Although buffering volumes can increase the delay in measurements between sampling inlets, our sampling system is setup to allow for continuous airflow through the buffering volume and through the manifold. This continuous flow of gas samples helps reduce the delay time of gas samples reaching the sample cells of the gas analyzer. Aluminum/polyethylene composite tubing (Synflex 1300, Aurora, OH, USA), with an interior diameter of 4.318 mm, was used to carry gas samples between the inlets, tanks, the buffer volume apparatus, and multiport manifold. Low-density polyethylene tubing with an inner diameter of 6.35 mm connected the manifold's exhaust port to the Gast pump. Similar tubing connects the gas analyzer to the Edward's pump.

The  $^{13}\text{C}$  composition of  $\text{CO}_2$  in the air was expressed in delta notation form, calculated using  $^{13}\text{C}^{16}\text{O}_2$  and  $^{12}\text{C}^{16}\text{O}_2$  mixing ratios measured by the TGA200A, given by:

$$\delta^{13}\text{C} = \left[ \left( \frac{R_{\text{sample}}}{R_{\text{standard}}} \right) - 1 \right] * 1000 \quad (2.1)$$

where  $\delta^{13}\text{C}$  is the carbon isotopic composition of a given substance (‰),  $R_{\text{sample}}$  is the ratio of the heavy isotopologue concentration ( $^{13}\text{CO}_2$ ) to the more abundant lighter isotope concentration ( $^{12}\text{CO}_2$ ) in a given gas sample.  $R_{\text{standard}}$  is the reference isotopic ratio value, stemming from the

Vienna Pee Dee Belemnite samples (VPDB), equal to 0.011797 (Griffis, 2013). The delta notation simply gives a reference for how enriched or depleted the sample is with the concentration of the  $^{13}\text{C}$  relative to the standard material.

### 2.2.2 Allan deviation analysis

To conduct the Allan deviation analysis, we first used our Edwards pump to pull gas samples from a tank with a known  $\text{CO}_2$  concentration (~450 ppm) through the manifold and into the TGA sampling cell for 4 hours. The tri-band laser was the first laser to be tested and the test was conducted in the laboratory. Approximately three months later, the dual-band laser was tested using the same methodology as the tests conducted on the tri-band laser. However, the tests for the dual-band were completed under field conditions. The  $\text{CO}_2$  mixing ratio and  $\delta^{13}\text{C}$  signal from each laser during the 4-hour interval was used to calculate the Allan deviation using the following equation (Allan, 1966):

$$\sigma_y(\tau) = \sqrt{\frac{1}{2(n-1)} \sum_{i=1}^{n-1} (y_{i+1} - y_i)^2} \quad (2.2)$$

where  $\sigma_y(\tau)$  is the Allan deviation at some given length of time scale,  $n$  is the number of samples being examined,  $\tau$  is the length of the time scale allotted for the averaging interval of the signals,  $y_i$  is the signal value within an interval of  $\tau$ ,  $y_{i+1}$  is the signal value within the next interval of  $\tau$ , and  $i$  is an index. Values of  $\sigma_y(\tau)$  were obtained for a range of  $\tau$  values ranging from 0.1 to 4000 seconds using a Matlab script. This time interval was selected as it corresponds to typical averaging time intervals in micrometeorological studies.

### 2.2.3 Buffer volume tests

The tri-band laser was used to measure the mixing ratio of  $\text{CO}_2$  from two sampling inlets. The sampling inlets were positioned to sample air from an exhaust port located inside

Throckmorton Hall's plant growth chamber room. The exhaust port consisted of a plastic box with a volume of approximately 38 L with a 12.7 cm outer diameter plastic hose attached to its top. A blower (Vanguard 208VAC, Rotron) drew air from the top of Throckmorton hall through the hose and into the box.

To evaluate the effect of buffering volumes on concentration measurements, one sampling inlet was connected directly to the manifold. The other sampling inlet was connected to the buffering volume apparatus, which was then connected to the manifold. Each inlet's air stream was sampled by the TGA every 30 seconds over a two-day period. The mixing ratios of  $^{13}\text{CO}_2$  and  $^{12}\text{CO}_2$  were measured by the TGA during each 30-second cycle. The CR3000 monitored which inlet was being analyzed by the TGA during these 30-second cycles, which was necessary for accurate data labeling. Data containing the 30-second mixing ratio cycle and their respective inlet labels, inlets with or without the buffering volume treatment, were then transferred to the CR3000. The CR3000 was programmed to calculate the standard deviation of mixing ratio values during each 30-second cycle. Each 30-second cycle was then sorted out by the corresponding sampling inlet. The standard deviation values between each corresponding inlet were then compared to evaluate the effect that buffering volumes had on the standard deviations on  $\text{CO}_2$ .

A method proposed by Qiu (2006) was used to estimate errors associated with partial sampling times and to determine if buffering volumes reduced these errors. In this methodology, we need to split an original sample's results into different sub-samples to simulate multiple inlets and their respective sample mixing ratio averages. Data were collected over the course of one day at the Konza Prairie Biological Station's K2A watershed. Two inlets were used to draw gas to the TGA during this experiment. One inlet stream was passed through a buffering volume,



while the other inlet stream was not. The first 10 seconds of each 30-second sampling interval for this inlet was eliminated, leaving 20 seconds of data to be averaged. The omission of these 10-second intervals was necessary to ensure that each currently being sampled air intake's gas stream had completely purged the previously sampled air intake's gas stream.

The 20-second averages were then split into 5 groups, hereafter called sub-samples. Since the TGA operates at 10 Hz, this means that 200 measurements are gathered in each 20-second sampling interval. Therefore, splitting these 200 measurements up into the 5 sub-samples results in 40 measurements per sub-sample. The splitting into sub-samples simply simulates the use of 5 inlets cycling samples through the TGA. This splitting was done for the inlet stream that had passed through the buffering volume and the inlet stream that did not go through a buffering volume. Purging times in the sub-samples were deemed unnecessary for this particular experiment, as the main emphasis of this particular experiment was to determine if buffering volumes helped reduce the partial sampling time errors and the deviation values of CO<sub>2</sub> and  $\delta^{13}\text{C}$ .

The mean mixing ratio of CO<sub>2</sub> and  $\delta^{13}\text{C}$  for each full sample period,  $C_o$ , and their respective sub-sample periods,  $C_i$ , can be subtracted from one another to determine the apparent error for each sub-sample ( $\Delta C_i$ ). For example, the full sample mean mixing ratio or  $\delta^{13}\text{C}$  for some time interval of 20 seconds is  $C_o$  and the first sub-sample mean within that full sample has a value of  $C_i$ . The difference between  $C_i$  and  $C_o$  ( $C_i - C_o$ ) is the error associated with partial sampling time for these samples, which is labeled as  $\Delta C_i$ . The 20-second samples, which were not split, were then used to estimate the maximum and minimum error by using the central limit theorem as suggested by Qiu (2006). By using this theorem, we assume our data to be normal

and that we had a large number of samples. The central limit theorem (CLT) with 95% probability is given as follows:

$$|\bar{c} - \mu_c| = \frac{1.96 \sigma_c}{\sqrt{n}} \quad (2.3)$$

where  $|\bar{c} - \mu_c|$  is the estimated maximum and minimum error,  $\bar{c}$  is the sub-sample mean, and  $\mu_c$  is the full sample mean.  $\sigma_c$  is the standard deviation of the full time period sample set and  $n$  is the number of samples in the set. The daily root mean square error was computed and compared between the buffering-volume treated sub-samples and the sub-samples that did not undergo a buffering-volume treatment. Lastly, the number of sub-sample periods that went above or below the maximum or minimum errors, respectively, were compared between the sub-samples that were passed through the buffering volume to the sub-samples that were sent directly to the sampling manifold. The number of instances that the sub-sample periods went above or below the minimum and maximum error estimates were tallied for the sub-samples that had undergone a buffering volume treatment and tallied for the sub-samples that did not. These tallies were compared against the total number of samples in their respective treatment (with buffering or without buffering) in order to calculate the percentage of occurrences that sub-sample group means went above or below the maximum error estimate value at 95% probability.

The relationship between partial sampling errors and the number of air intakes was investigated during a 7-day period. Samples were taken above a native tall-grass prairie canopy. A single inlet was used to sample air; therefore, there was no cycling to other inlets or tanks. Air sampled from the single air inlet was mixed using the air buffering apparatus in order to reduce high frequency fluctuations and variability in the CO<sub>2</sub> mixing ratios and  $\delta^{13}\text{C}$  values. Data analyzed from this single inlet's air stream were split into sub-sample groups simulating 2, 4, and 10 inlets. Each sub-sample groups was given 30 seconds of analysis time. The initial 10 seconds

in these 30-second intervals were removed to allow for purging time. Only one sub-sample group was analyzed for its CO<sub>2</sub> mixing ratio and  $\delta^{13}\text{C}$  30-minute averages over the duration of the experiment. The 30-minute averages from this one simulated inlet, per sub-sample group, were compared with the true 30-minute averages that were based on the single air inlet's data. For example, in the case of the sub-sample group with 2 inlets, only one of these inlets' 30-minute averages were compared against the 30-minute average from the single inlet. Similarly to the methodology used by Qiu (2006), the values for each sub-sample group's one inlet 30-minute average was subtracted by the true 30-minute average values. These values, referred to as  $\Delta\text{C}$  (similar to  $\Delta\text{C}_i$ ), reveal the error between treatments compared to the true values. These values and their standard deviations were compared over the 7-day period.

## 2.3 Results and discussions

### 2.3.1 Allan deviation

The Allan deviation plots shown in this section were limited to 3000 seconds. This was done to help highlight noise and deviation characteristics that occur with changing averaging intervals. Plotting the entire 4-hour interval could reduce our ability to see noise characteristics and trends in deviation because of plot scaling effects. From here on, the term CO<sub>2</sub> refers to the total mixing ratio of the CO<sub>2</sub> in the gaseous sample and does not refer to one particular isotopologue.

Figure 2.2 displays the Allan deviation curves of  $\delta^{13}\text{C}$  and CO<sub>2</sub> for both the tri-band and dual-band lasers for a range of averaging time intervals. Figure 2.2A shows that the tri-band laser typically has higher Allan deviation values than the dual-band laser for all averaging time intervals. The dual-band laser's initial  $\delta^{13}\text{C}$  deviation value, when  $\tau$  is at 1 second, is approximately 0.42‰, while the tri-band laser's initial  $\delta^{13}\text{C}$  deviation value is approximately

1.68%. Figure 2.2B shows that for all averaging time intervals plotted, the tri-band laser had a relatively higher Allen deviation than the dual-band laser's Allan deviation values. The initial CO<sub>2</sub> deviation values for the dual-band and tri-band are, respectively, 0.13 ppmv and 0.49 ppmv. Higher deviation in the averaging time interval typically means more variability and less precision in the data. The dual-band laser's performance, in terms of its precision for measuring CO<sub>2</sub> and for measuring <sup>12</sup>C<sup>16</sup>O<sub>2</sub> and <sup>13</sup>C<sup>16</sup>O<sub>2</sub> so that δ<sup>13</sup>C can be calculated, has less deviation and more precision than the tri-band for all averaging intervals. Many factors could play into why this occurring. Since the tri-band dedicates time to scanning for three separate isotopologues (<sup>12</sup>C<sup>16</sup>O<sub>2</sub>, <sup>13</sup>C<sup>16</sup>O<sub>2</sub>, and <sup>12</sup>C<sup>18</sup>O<sup>16</sup>O), there are less data points available to be measured and likely more deviation in the data set. The dual-band dedicates time to scanning for only two separate isotopologues (<sup>12</sup>C<sup>16</sup>O<sub>2</sub> and <sup>13</sup>C<sup>16</sup>O<sub>2</sub>). Therefore, more data points are available to be analyzed and less variability is expected.

Additional analysis is needed to determine if differences in pressure and temperature in the TGA sampling cell and reference cell are influencing the results of this particular study. The dual-band's average pressure during sampling of the tank was 30.1 mb, while the tri-band was on average at 24.3 mb. Additionally, the TGA's temperature was approximately 35°C when using the tri-band and 45.3°C when using the dual-band laser. It would be very beneficial to repeat this test again and analyze both lasers in house. This test would surely confirm the results revealed in Figure 2.2, but new minimum deviation values might become available to analyze and compare between the two lasers.

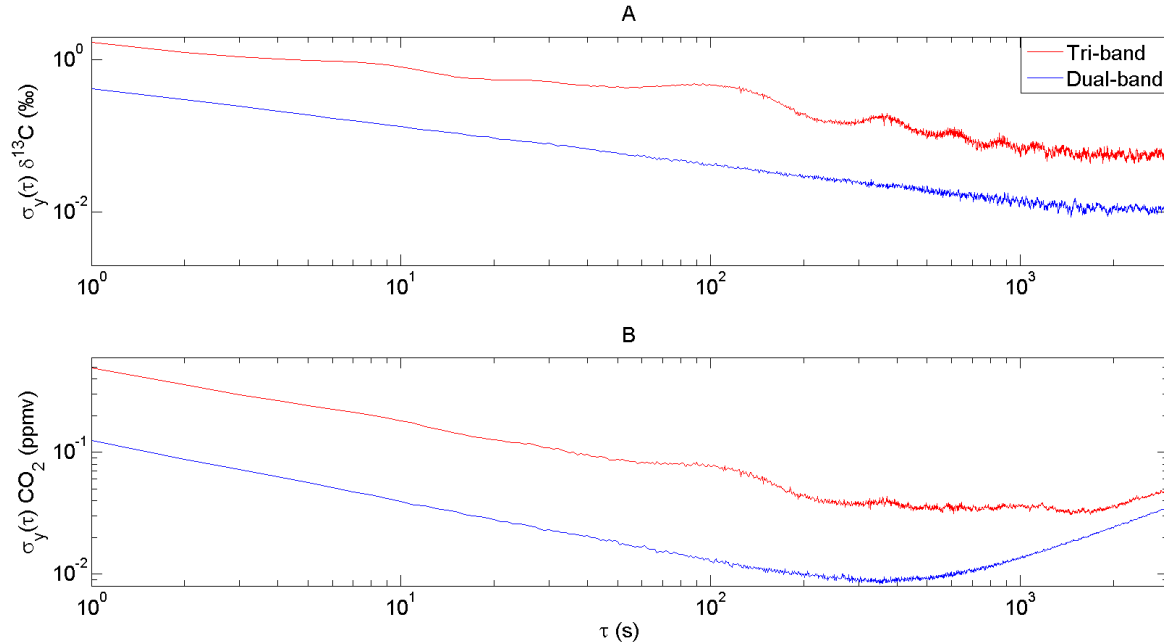


**Figure 2.2 – (A) Allan deviation comparison between the tri-band and dual-band laser’s  $\delta^{13}\text{C}$  signals and (B) shows the Allan deviation comparison of the tri-band and dual-band laser’s  $\text{CO}_2$  mixing ratio signals. The averaging time interval ( $\tau$ ) ranged from 1 to 3000 seconds.**

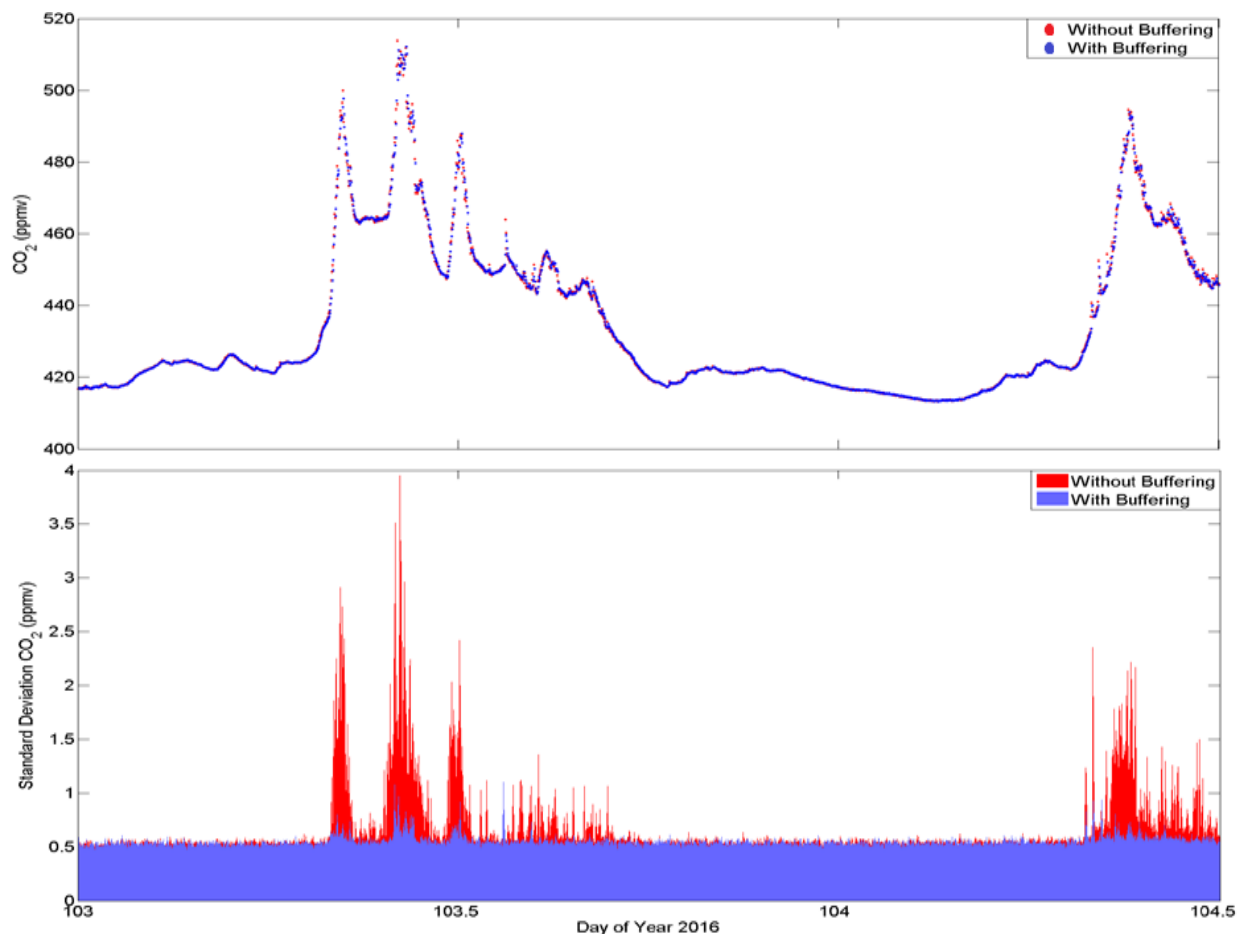
### 2.3.2 Buffer volumes and partial sampling errors

Figure 2.3 shows the diel changes in  $\text{CO}_2$  mixing ratio over time for this experiment and the results of the buffering experiment, respectively. The air inlet stream with a buffering volume connected (blue shade) had an average flow rate of  $212.31 \text{ cm}^3 \text{ min}^{-1}$  during the test, while the air inlet stream without the buffering volume connected had an average air flow rate of  $204.31 \text{ cm}^3 \text{ min}^{-1}$  during the test. The TGA’s pressure stayed relatively constant through the experiment and was on average 22.34 mb. Each inlets’  $^{13}\text{CO}_2$  and  $\text{CO}_2$  mixing ratio values and their standard deviations were compared for a 2-day period, but only 36 hours of this experiment will be discussed to help distinctly show differences between the deviation values of the inlets.

Figure 2.3A shows the mixing ratios of  $\text{CO}_2$  measured for both inlets over the course of 36 hours, while Figure 2.3B displays the  $\text{CO}_2$  mixing ratio standard deviation values for the inlets. The  $\text{CO}_2$  mixing ratio increases dramatically during the daytime for both air intakes.

Daytime mixing ratio values vary widely for both inlets, with brief periods of stable mixing ratios between spikes in mixing ratio values throughout the day. Nighttime mixing ratio values showed less variability and were lower in CO<sub>2</sub> values compared to the daylight measurements for both inlet treatments. Additionally, both treatments appear to have similar mixing ratio values during the nighttime measurements. Figure 2.3B displays the change in standard deviation over the course of the buffering volume test. Inlet 6 (without buffering volume) showed more fluctuations in CO<sub>2</sub> mixing ratio than the sample line with the buffering volume (inlet 5).

Results from Figures 2.3A and 2.3B show that the use of buffering volumes in multi-port sampling systems definitely helps reduce noise concentration measurements. Since the gas being sampled is derived from an urban environment, the spikes in CO<sub>2</sub> mixing ratio is likely based on anthropogenic sources, such as vehicle emissions. The timestamps seem to coincide with what would be inferred as the rush-hour traffic. Hence, a major increase in the CO<sub>2</sub> mixing ratio occurs at these times. The buffer volumes appear to attenuate the spikes in the CO<sub>2</sub> mixing ratio.



**Figure 2.3 – (A) shows the CO<sub>2</sub> mixing ratios (ppmv) measured from sampling inlets with and without air mixing volume treatments over time and (B) shows the CO<sub>2</sub> mixing ratio standard deviations (ppmv) for the gas sampling inlets with and without the air mixing volume apparatus treatment (inlets 5 and 6, respectively).**

Figure 2.4 depicts the results of the sub-sample partial error experiment for air inlets with the buffering volume attached (inlet 5) and without the buffering volume attached (inlet 6). For Figure 2.4A, estimates reveal that 1059 sub-sample error values exceeded the maximum positive estimated error values and that 1058 sub-sample error values were below the maximum negative estimated error value. This shows that nearly 29.4% of the 7195 sub-samples had errors that were unpredictable using the CLT with 95% probability. The root mean square error for this treatment was calculated to be 0.2528  $\mu\text{mol CO}_2 \text{ mol}^{-1}$  dry air per day. For Figure 2.4B, estimates

reveal that 538 sub-sample error values exceeded the maximum positive estimated error values and that 510 sub-sample error values were below the maximum negative estimated error value. This shows that about 14.6% of the 7195 sub-samples had errors that were unpredictable using the CLT with 95% probability. This value of 14.6% is notably less compared to the 29.4% value obtained by the inlet stream that did not have a buffering volume attached. The root mean square error for this treatment was calculated to be  $0.1149 \text{ umol CO}_2 \text{ mol}^{-1} \text{ dry air per day}$ , which was less than the root mean square error for inlet 6.

Figure 2.5 depicts the results of the sub-sampling partial errors of  $\delta^{13}\text{C}$  values for inlets 6 and 5, respectively. Figure 2.5A reveals that approximately 195 sub-sample error values exceeded the maximum positive estimated error values and that 194 values were below the maximum negative estimated error values. This reveals that about 5% of the sub-samples had errors that were unpredictable using the CLT with 95% probability. The root mean square error for this treatment was calculated to be 0.25%. For Figure 2.5B, we found that roughly 181 sub-sample error values exceeded the maximum positive estimated error values and that 169 values were below the maximum negative estimated error values. This reveals that about 4.9% of the sub-samples had errors that were unpredictable using the central limit theorem with 95% probability. The root mean square error for this treatment was calculated to be 0.25%. There appears to be minimal difference between the treatments when examining the  $\delta^{13}\text{C}$  signal.

The results in Figures 2.4 show that samples going through the buffer volumes were more concise compared to the samples that did not undergo mixing through the buffering volumes. What this means that the samples that did undergo mixing were typically closer to the true 30-minute values compared to samples that did not undergo a mixing treatment. Therefore, the buffering volume apparatus helped reduce the errors associated with partial sampling times when

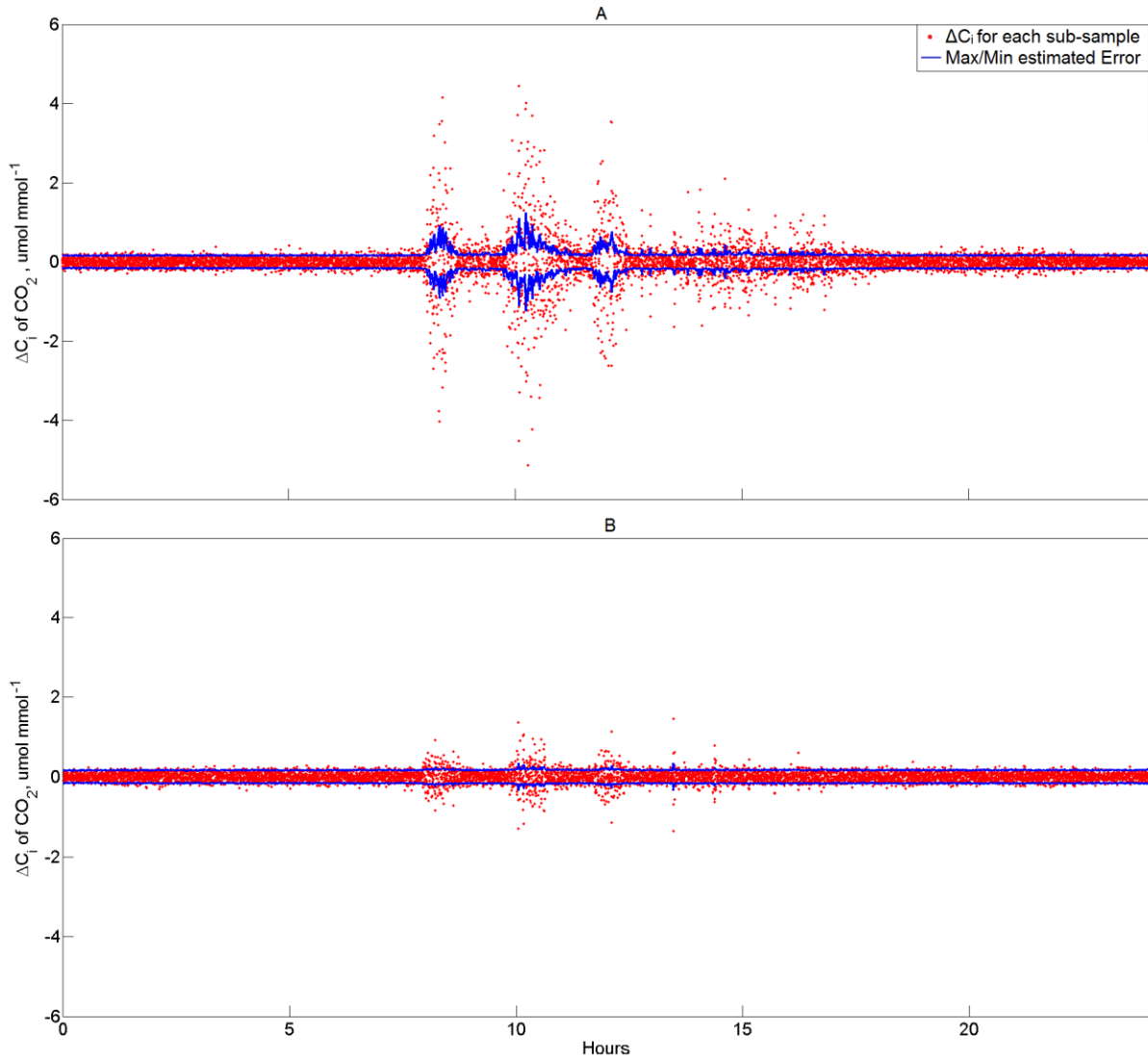


examining the CO<sub>2</sub> mixing ratio and improved the confidence that our data would fall within the maximum error estimates. Figure 2.5 shows that the buffering volume had relatively little impact on decreasing the apparent error and the standard deviation values for  $\delta^{13}\text{C}$  signals. One theory behind this is that since  $\delta^{13}\text{C}$  is a ratio between the  $^{13}\text{C}^{16}\text{O}_2$  and  $^{12}\text{C}^{16}\text{O}_2$  molecule and that the buffering volume likely mixed both isotopologues equally well,  $\delta^{13}\text{C}$  would not likely be influenced. If the buffering volumes did create a noticeable fractionation event, then this would've likely influenced the results shown in Figure 2.5.

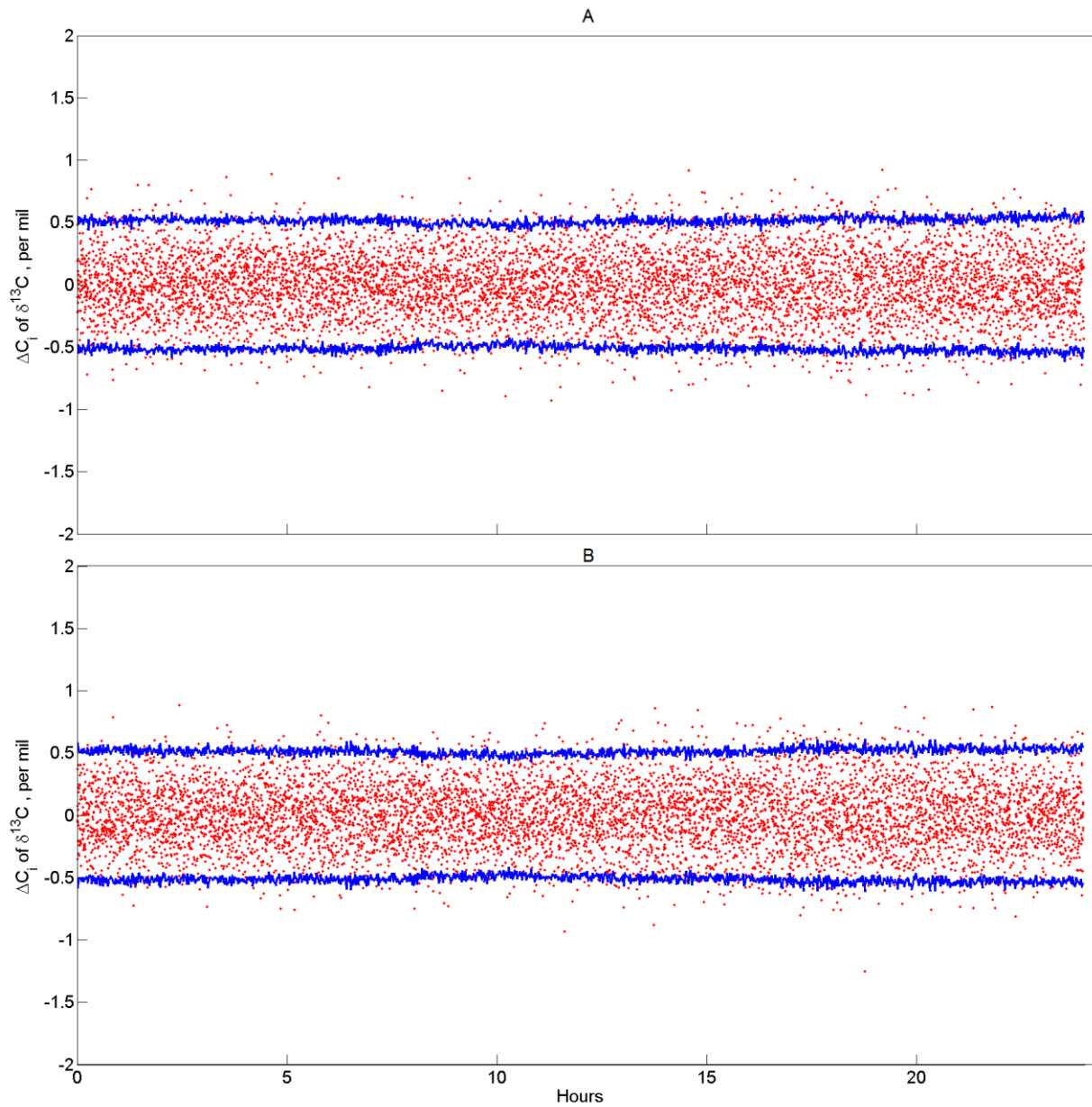
Figure 2.6 depicts the results of the CO<sub>2</sub> mixing ratio partial sampling time error test for a different number of air intakes. For this test, the 30-min mixing ratio measurements by a single intake, which were not subject to partial sampling time error, were used as a reference to the true 30-min mixing ratio measurements. Figure 2.6A shows that increasing the number of inlets for the sampling system appears to decrease the accuracy of the mixing ratio measurements, likely because of data loss from cycling through other inlet sampling and purging cycles. There are a few instances when this trend is not true. For example, in the early hours of DOY 214, the 4-inlet treatment's error value appears to be equal to or just above the error value of the 10-inlet treatment. The reduced sample size for the 10-inlet treatment might be increasing the variability of the dataset, thereby resulting in a higher-than-normal difference compared to the true 30-min mixing ratio measurements.

Figure 2.6B shows that, much like the results revealed in Figure 2.6A, the 10-inlet treatment consistently had higher values. In this case, these are higher standard deviation values. Thus, the trend in these data is that increasing the number of inlets in a sampling cycle can lead to higher variability within each of the inlets respective 30 minute sampling average periods.

Similarly, there are instances where the deviation values of the lower number of inlet treatments, 2 and 4, are relatively close to one another. This has been attributed as random error.



**Figure 2.4 – (A) shows partial sampling errors calculated (red dots) with respect to the full sample mean values for inlet 6 (without air-mixing) and (B) depicts results with respect to full sample mean values for inlet 5 (with air-mixing). The blue lines in both plots depict the maximum positive and negative errors of the  $\text{CO}_2$  mixing ratio that can be estimated using the central limit theorem.**



**Figure 2.5 – (A) shows partial sampling errors calculated (red dots) with respect to full sample mean values for inlet 6, the treatment without air mixing and (B) depicts the results with respect to full sample mean values for inlet 5, the air mixed sample treatments. The blue lines in both figures depict the maximum positive and negative  $\delta^{13}\text{C}$  (‰) errors values that can be estimated using the central limit theorem.**

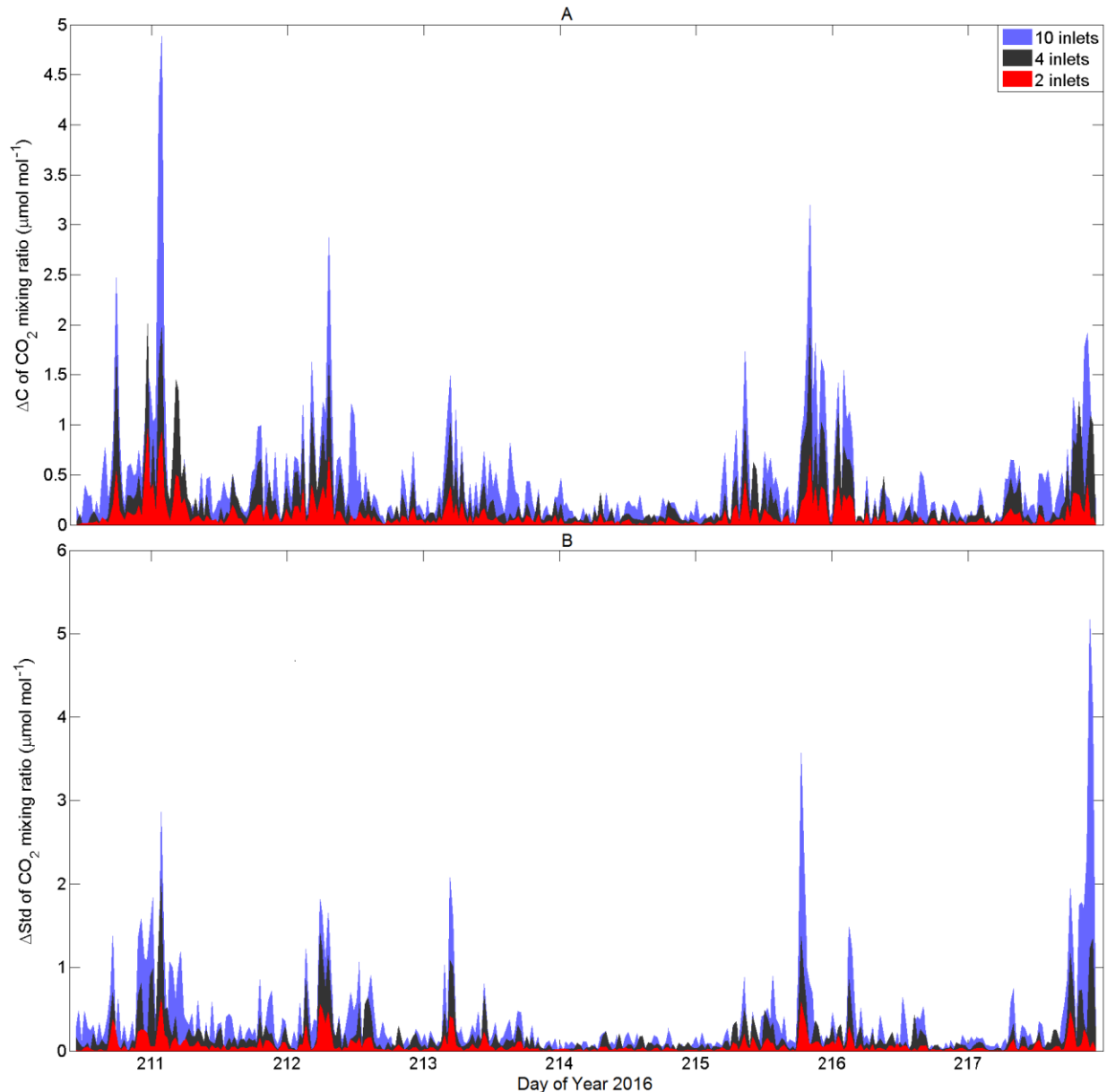


**Figure 2.6 – (A) shows the 30-minute average mixing ratio of CO<sub>2</sub> results of the multiple inlet tests and (B) shows the standard deviation values for these 30 minute averaging periods. The red shading represents the values of error for the 2-inlet treatment, black shading for the 4-inlet treatment, and blue shading for the 10-inlet treatment.**

Figure 2.7 depicts the evaluation of the differences in  $\delta^{13}\text{C}$  signals between the respective multiple inlet treatments and the true single inlet treatment's 30-minute averaging period. Figure 2.7A shows a noticeable trend in the increase of difference in  $\delta^{13}\text{C}$  signal with an increase in the

number of inlets used in a sampling cycle, but this trend is not as strong as the one depicted in Figure 2.7A for the CO<sub>2</sub> mixing ratio values. In many periods, the 2 and 4-inlet treatments have equal to or roughly greater difference values compared to the 10 inlet treatment. Despite this apparent weaker trend, the  $\delta^{13}\text{C}$  signals for the 4-inlet treatments were usually lower than 0.1‰. For the 2-inlet treatments, the  $\delta^{13}\text{C}$  signal is usually lower than or equal to 0.05‰. Much like the previous plots regarding this multiple treatment experiment, Figure 2.7B reveals there is a notable trend between the increasing number of inlets and the increase in the magnitude of the difference in standard deviation values. However, as mentioned in the previous discussion, the trend is not as clear as for the CO<sub>2</sub> mixing signals. Several instances occur where the smaller number of inlet treatments have standard deviation difference values equal to or greater than the 10-inlet treatment, but this is likely attributed to random sampling error. Despite these occurrences, the standard deviations for most treatments is typically below 0.1‰, but a few instances where values are higher did occur for the 10-inlet treatment. Based on these results, it appears that increasing the number of inlets used in a sampling system increases the measurement noise due to partial sampling time errors. The sampling system's performance does not appear to be hindered majorly when using 4 inlets.

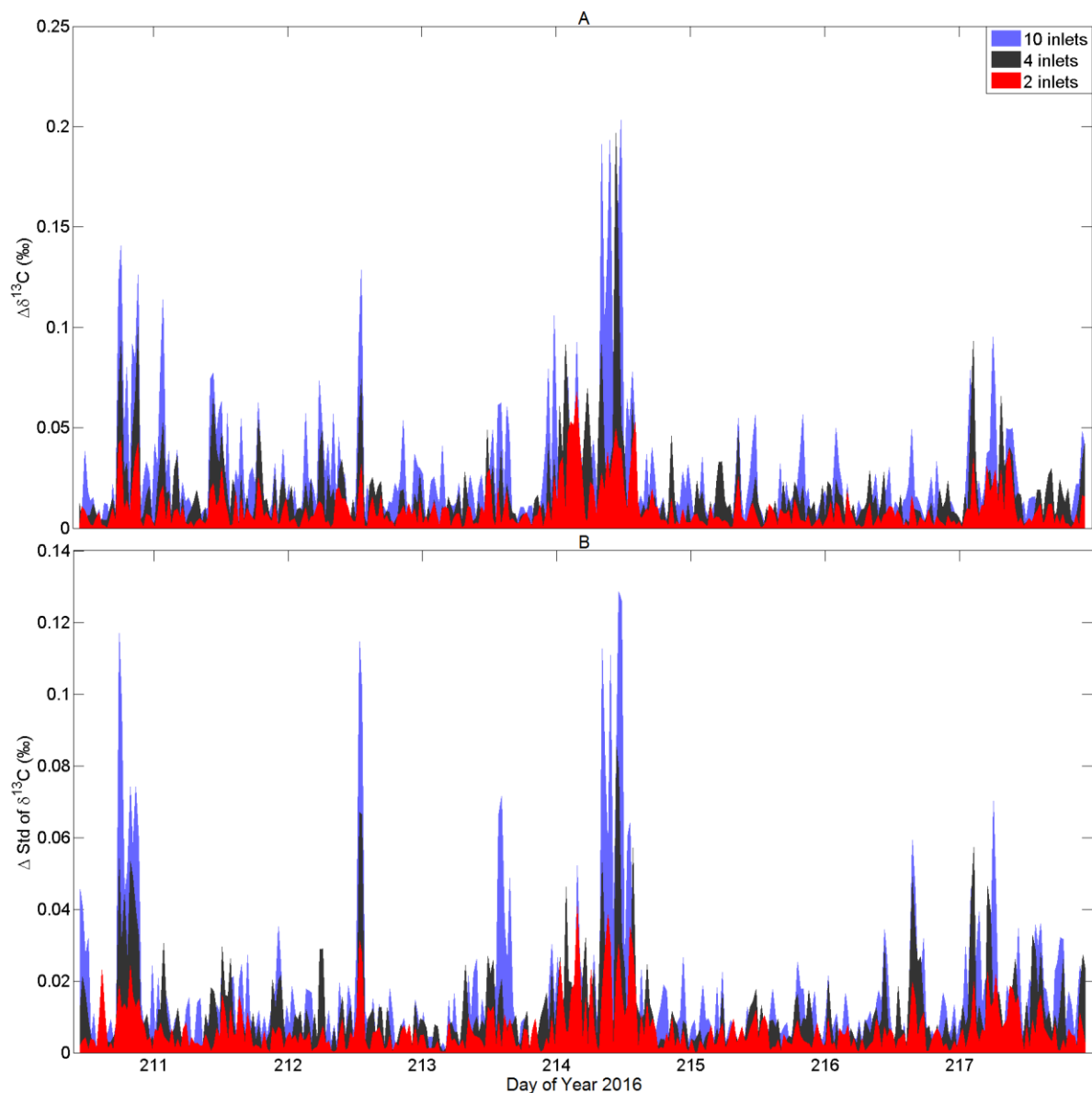


**Figure 2.7 – (A) shows the 30 minute average mixing ratio of  $\delta^{13}\text{C}$  (‰) results of the multiple inlet tests and (B) shows the standard deviation values for these 30 minute averaging periods. The red shading represents the values of error for the 2-inlet treatment, black shading for the 4-inlet treatment, and blue shading for the 10-inlet treatment.**

## 2.4 Conclusions

More tests are needed to describe the noise of  $\delta^{13}\text{C}$  and  $\text{CO}_2$  signals when using the dual-band laser with the air-mixing volume apparatus attached to the gas inlets. In addition, the long-term accuracy and stability of each laser needs to be tested. Our tests show that this instrument is

suitable for monitoring and measuring ambient air samples for CO<sub>2</sub> isotopologues. Although the tri-band laser source was less precise than the dual-band laser attachment, measurements of <sup>12</sup>C<sup>18</sup>O<sup>16</sup>O could increase our understanding of the interactions between the water and carbon cycles. Thus, precision and variability in stable isotope signals might be traded for the ability to measure <sup>12</sup>C<sup>18</sup>O<sup>16</sup>O.

Though one inlet is optimal for this sampling system, one inlet can be an unfeasible option when wanting to analyze the gas concentration profile in a canopy and ecosystem. Analyzing the concentration profile with one gas analysis instrument requires multiple inlets at varying heights. Therefore, a more sophisticated approach might be necessary to indicate the maximum number of inlets feasible with a given acceptable apparent error and deviation in the sampling system's performance.

Lastly, the buffering volume system helped reduce errors associated with partial sampling time and helped to reduce natural variability of CO<sub>2</sub> mixing ratio measurements. Additional tests could be used to test error reductions and variability for the <sup>18</sup>O stable isotope signal when using the tri-band laser. Additionally, since the buffering volume test used the tri-band laser and the tests were completed in an urban setting, similar buffer volume tests are needed with the dual-band laser attachment in a similar setting. This would help show the amount of error expected with the dual-band, compared to the tri-band, when buffering volumes are used to mix gas samples. Advances in optics may help improve the tri-band laser's performance. Additional lasers might become available for the TGA200A in the near future that measure isotopic signals in methane and other trace gas species. These lasers would require performance tests similar to what has been conducted in this experiment. Identifying the quality of data produced by these lasers will be essential to enhancing our future global carbon cycling models.

# **Chapter 3 - In-situ measurements of CO<sub>2</sub> isotope exchange using tunable diode laser spectroscopy and micrometeorological methods at a tall grass ecosystem**

## 3.1 Introduction

There is a need to better understand how environmental drivers and management practices influence the carbon cycle at the ecosystem scale, so that we can better predict how climate change will affect precipitation patterns, ambient air temperatures, and energy partitioning and biogeochemical cycles (Dore, 2005; Wu et al, 2011; Ciais et al, 2013; Collins et al, 2013). Such changes could significantly alter the plant community composition (Walther et al, 2002), ecosystem services (Lawler et al, 2014), and eventually soil properties (Post et al, 2000; Schwartz, 2014). The feedbacks created from changes in ecosystems and environmental variables are not well understood, nor well predicted, thereby leading to a notable loss of certainty and accuracy in current carbon cycling models that are used to simulate global climate change scenarios (Griffis, 2007; Welp et al, 2011; Cuntz, 2011; Ciais et al, 2013; Dymond et al, 2016). In order to resolve these issues, so that we can better predict and prepare for different climate change scenarios, we must have a better understanding of how the connections between carbon exchange mechanisms in the soil-plant-atmosphere continuum are altered when ecosystems are put under different management practices and environmental conditions (Brüggemann et al, 2011; Werner et al, 2012).

With recent advances in optical instrumentation, we can now sample gases at faster sampling rates for longer sampling campaigns, which will be helpful to solve some of our knowledge gaps regarding carbon cycling in ecosystems (Griffis, 2013). As noted in Chapter 1,



this advancement in optical sensor technology has facilitated the combination of micrometeorological measurements with stable isotope analysis to measure changes in the isotope composition  $\text{CO}_2$  and  $\text{H}_2\text{O}$  ecosystem effluxes at a wide variety of spatial and temporal scales. (Werner et al, 2012; Griffis, 2013). These new techniques could bolster our ability to analyze the movement of  $\text{CO}_2$  in ecosystems that undergo changing management practices and environmental conditions. These measurements could be particularly useful in mixed grassland ecosystems because these ecosystems take up a relative large proportion of the Earth's surface and are a significant carbon stock (White et al, 2000; Conant, 2010), thereby making them a pivotal player in the global carbon cycle. As such, major changes in these ecosystems, brought about by management practices and environment drivers, could drastically alter or even enhance global climate change. Two of the major management practices of grasslands are rangeland grazing operations and timely prescribed burn treatments (Collins & Calabrese, 2012; Fischer et al, 2012). As previously mentioned in Chapter 1, management conditions can significantly alter species composition, notably the  $\text{C}_3$  and  $\text{C}_4$  composition, as well as the isotopic signal of a grassland ecosystem's net  $\text{CO}_2$  exchange (NEE). Hence, the practice of combining micrometeorological techniques with stable isotopic analysis could help us to monitor changes in  $\text{C}_3/\text{C}_4$  composition in these ecosystems by tracking the relative contribution of these species to the net  $\text{CO}_2$  exchange at the ecosystem scale.

The main objective of the study described in this last chapter was to investigate how grazing and prescribed burns affect the  $^{13}\text{C}$  composition of the NEE at the Konza Prairie Biological Station using high frequency measurements of  $^{13}\text{CO}_2$  and  $^{12}\text{CO}_2$  and micrometeorological techniques. The mixing ratios of  $^{13}\text{CO}_2$  and  $^{12}\text{CO}_2$  were monitored using a tunable diode laser spectrometer (TDLS) at two heights, in two watersheds during the 2016

sampling season. These watersheds are under different management conditions: one is ungrazed under a 2-year prescribed burn cycle and the other one is grazed in a 3-year patch burn cycle. It is hypothesized that these watersheds will have notably different isotopic ratios of the  $^{13}\text{CO}_2$  and  $^{12}\text{CO}_2$  NEE fluxes.

## 3.2 Methodology

### 3.2.1 Site description

The site selected for our study was the Konza Prairie Biological Station (KPBS, Lat: 39.0987° N; Long:-96.5671°; Alt: 415 m) south of Manhattan, Kansas. The KPBS is located in the Flint Hills of Kansas and is one of the few remaining native tall-grass prairie ecosystems. The KPBS is described as a temperate mid-western continental climate with an annual mean temperature of 13°C (Collins et al, 2012). Annual precipitation is approximately 835 mm and the majority of this rainfall occurs during the growing season, which encompasses early March into late August (Hayden, 1998), but the rainfall can vary significantly on a year to year basis. The dominant wind direction in Kansas is from the south. The Flint Hills area primarily consists of perennial C<sub>4</sub> grasses, such as big bluestem (*Andropogon gerardii*), little bluestem (*Schizachyrium scoparium*), indiangrass (*Sorghumstrum nutans*), and many others. Perennial forbs, woody vegetation, and C<sub>3</sub> grass communities also inhabit the landscape. The diversity and abundance of plant species varies considerably depending upon the experiment location within each watershed, because each watershed has different management treatments consisting of varying prescribed burn treatments, such as different frequencies and times of ignition, to different grazing applications. The field experiment was carried out from April to November in 2016 in two adjacent watersheds: K2A and C3SA. The K2A watershed is burned every other year and is ungrazed. The most recent prescribed burn occurred on April 12, 2016. The majority of species in this

watershed are C<sub>4</sub> grass plants, while woody species communities are sparsely connected in the hill valleys. The C3SA watershed is a part of a patch-burn grazing system with neighboring watersheds, with particular sections of the watershed being burned every three years. The last burn occurred on April 1, 2014 and the grazing system was established in 2011. The stocking density from May 1<sup>st</sup> to October 1<sup>st</sup> is roughly 3.2 ha per cow and calf pair (Konza LTER, 2016). The C3SA watershed had a noticeable increase in the abundance of sedges, shrubs, and woody species relative to the K2A watershed. In some parts of watershed, there are flattened stands of vegetation because of cattle movement stomping plants down onto the soil surface. This influences the variability of the plant height across the landscape, thus the canopy height and leaf area index (LAI) of the C3SA watershed is expected to be not as uniform as the K2A watershed.

The soil properties of these watersheds vary considerably because of the topographical features of the landscape, such as the hill slope position, are notably different. The K2A watershed predominately contains soil units mapped as a Benfield-Florence complex with slopes ranging from 5% to 30%. This complex has a typical profile depth of 96.5 cm before reaching weathered bedrock (NRCS, 2016). The main textures in this complex are silty clay loams and silty clays, within the A and B horizons respectively. The air intakes sampling gases in this watershed, which will be discussed more extensively later, were installed well within the Benfield-Florence complex-mapping unit. The C3SA watershed is predominately composed of Clime-Sogn complexes with slopes ranging from 3% to 20%. The typical profile depth of these complexes is 78.7 cm before reaching weathered bedrock (NRCS, 2016). The main texture in this complex is a silty clay throughout the soil horizons. Air intakes for this watershed were installed near a shift between the Clime-Sogn complexes and the Benfield-Florence complexes. Soil maps for the K2A and C3SA watersheds are provided in Appendices A and B, respectively.

### 3.2.2 Isotope measurements

The mixing ratios of the  $^{12}\text{CO}_2$  and  $^{13}\text{CO}_2$  isotopologues were measured at a frequency of 10 Hz using a tunable diode laser trace gas analyzer (TGA200A, Campbell Scientific, Logan, UT, USA, hereafter TGA). The first laser used in the beginning of the experiment analyzed air for the mixing ratio of  $^{12}\text{C}^{16}\text{O}_2$ ,  $^{13}\text{C}^{16}\text{O}_2$ , and  $^{12}\text{C}^{16}\text{O}^{18}\text{O}$  (tri-band). This laser was replaced on May 18<sup>th</sup> (DOY 139) by one that measures the mixing ratio of only  $^{12}\text{C}^{16}\text{O}_2$  and  $^{13}\text{C}^{16}\text{O}_2$  isotopologues (dual-band). As described in Chapter 2, the tri-band laser typically had higher deviation values compared to the dual-band laser. This may play a role in our isotope analysis results. Such measurements are possible by these lasers using the tunable diode laser spectroscopy techniques as described in Chapters 1 and 2. Additional details about this technique are provided by Griffis (2013) and Bowling *et al* (2003). The TGA, and the casing that houses the instrument, were contained in a large white insulated wooden box. The box has an air conditioning unit attached to its lid to provide temperature control if necessary. Sampling inlets for the K2A watershed were installed April 17<sup>th</sup> (DOY 108), while inlets for the C3SA watershed were installed June 10<sup>th</sup> (DOY 162).

The TGA was interfaced with a custom-made multiport manifold sampling system (Campbell Scientific, Logan, UT, USA) to measure the isotopic composition of atmospheric  $\text{CO}_2$  above the canopies in the K2A and C3SA watersheds using air intakes (Figure 3.1). Air was drawn through the air intakes using sample (XDD1, Edwards) and bypass (DOAV502, Gast) pumps. Plastic tubing with a 12.7 mm outer diameter connected the TGA sample pump and a similarly sized low-density polyethylene tubing connected the manifold system to the bypass pump.

The air sampling intakes consisted of a stainless-steel tube connected to a plastic rain diverter and a mesh screen. Downstream from the stainless tubing is a heated filter (SS-4F-K4-7, 7 $\mu$ m sintered element filter, Swagelok, OH, USA) which was used to prevent dust accumulation and mitigate condensation in the sampling line and manifold. A PVC cover was used to shield the intake filter and the power connection to the heating element. The intakes were connected to aluminum/polyethylene composite tubing (Synflex 1300, Aurora, OH, USA), with an outer diameter of 6.35 mm and interior diameter of 4.32 mm, which was used to direct gas samples from the gas inlets to the air mixing volume apparatus, consisting of a series of 750 ml stainless steel flasks (1 flask per inlet line). Such mixing volumes act as a high-pass filter, which helps reduce high frequency in the trace gas measurements caused by atmospheric turbulence and minimizes errors caused by partial sampling time (Meredith et al, 2014; Cescatti et al, 2016). The air from all intakes was then drawn into the custom-made manifold (Campbell Sci.), which was used to direct the airflow from each inlet to the TGA or through the bypass. Reference tanks were directly connect to the TGA, while calibration gas tanks were directly attached to the manifold. The reference gas (2500 ppm CO<sub>2</sub>) was drawn though the TGA’s reference cell at a flow rate of 200 cm<sup>3</sup> min<sup>-1</sup>.

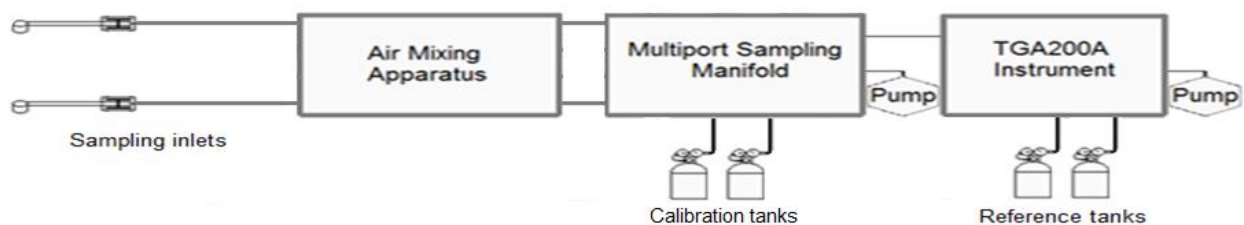


**Figure 3.1 – Schematic diagram illustrating of the isotope sampling system used in this study.**

The gradient of mixing ratios of <sup>12</sup>CO<sub>2</sub> and <sup>13</sup>CO<sub>2</sub> were measured at two heights above the canopy for each watershed. Initially, the air inlet heights for the K2A watershed were 0.49 m

and 1.53 m, while the inlet heights for the C3SA watershed were 0.56 m and 1.7 m. The intake heights were adjusted as the plant canopy height increased during the growing season, so that the lowest intake was above the roughness sublayer. Inlets were sampled for 30 seconds each before switching to another inlet. The K2A site's inlets were sampled first in a sequential order from the lowest to highest inlet, followed by the C3SA site's inlets being sampled in a similar fashion. Sample flow rate was maintained around  $200 \text{ cm}^3 \text{ min}^{-1}$ . This was done for roughly 4 minutes before switching to sampling the calibration tanks ( $\sim 320 \text{ ppm}$  and  $\sim 450 \text{ ppm CO}_2$ ). These tanks were sampled for 30 seconds each before switching back to inlet streams. The total cycle of measurements lasted for 5 minutes. The K2A site's air sampling inlets are approximately 174 meters west of the C3SA site's air sampling inlets.

### 3.2.3 Flux measurements

An eddy covariance (EC) system was installed at the K2A watershed to measure fluxes of energy and  $\text{CO}_2$ . An open path infrared gas analyzer (LI-7500, LICOR Biosciences, Lincoln, NE, USA) measured the mixing ratio of  $\text{CO}_2$  and  $\text{H}_2\text{O}$ , while a 3D sonic anemometer (CSAT3, Campbell Scientific) was used to measure the three orthogonal wind components ( $u_x$ ,  $u_y$ , and  $u_z$ ) during the sampling campaign. A datalogger (CR3000, Campbell Sci.) was used to record the data from the open path gas analyzer and the sonic anemometer at a frequency of 20 Hz. The EC instruments were installed at a height of 2.5 m. An additional EC system was installed 6 meters west of the first EC system. This extra EC system consisted of a combined sonic anemometer attached to a closed-path infrared gas analyzer (IRGASON, Campbell Scientific, Logan, UT, USA). The IRGASON was installed at a height of 2.58 m. Power supply issues and programming mistakes caused a loss of data for the first EC system. Data from the extra EC system was used to fill data gaps in the original EC system's flux measurements. Linear

regression analysis was conducted between the two systems to verify that differences between measured fluxes were minimal. Appendix C provides a plot of the flux comparison results. The flux comparison results between our EC system and the IRGASON EC system show that both flux values were highly correlated ( $R^2 = 0.9441$ ) and that differences between fluxes were small (slope = 0.9881). Therefore, data gaps in our original EC system were reliably filled using the IRGASON flux measurements. High frequency raw data from the original EC system were automatically transferred to a server every 30 minutes. Onsite card storage for both the original EC system and the alternate EC system were collected weekly. The high frequency data were processed using an offline software package (EddyPro, 6.0.0, LICOR Biosciences). Processed data were then used to fill gaps between the original EC system and the extra EC system by using a commercial software package (MATLAB, R2014a, The MathWorks Inc., Natick, MA, 2014).

Soil CO<sub>2</sub> flux was measured at least every other week using an automated chamber system (LI-8100, LICOR Biosciences, Lincoln, NE, USA). Ten chamber collars, made of PVC tubing (10 cm inner diameter, 5 cm in height), were placed at a cardinal and semi-cardinal direction 2 meters away from the EC station at a soil depth of 2.3 cm. Sampling dates were often 2-3 days after precipitation events had occurred. This was done to ensure our data was collected during times when moisture was readily available for microbial activity, but not when saturated to reduce the likelihood of sampling on days when respiration would be inhibited by excessive moisture. To ensure the accuracy of the soil CO<sub>2</sub> measurements, plant biomass was clipped from the interior of the collars; collars would be reinstalled every month to ensure good contact with the soil, as the natural wetting and drying of the soil pushed the collars out over time. Measurements for each collar included a 30-second dead band interval and a 2-minute sampling

period. The sampling flow rate of the LI-8100 was set to the lowest setting available as suggested by the manual. Volumetric soil water content and soil temperature were sampled at 10 cm below the soil surface. A linear regression model was created by correlating the LI-8100 outputs with the soil moisture and soil temperature variables measured by our soil moisture sensors (CWS655, Campbell Scientific, Logan, UT, USA). The linear regression model used was solved by using the follow:

$$Rs = i * T_{10} + j * \theta_{10} \quad (3.1)$$

where  $Rs$  is the soil respiration ( $\text{umol m}^{-2} \text{s}^{-1}$ ),  $T_{10}$  is the soil temperature at 10 cm ( $^{\circ}\text{C}$ ),  $\theta_{10}$  is the volumetric soil moisture content at 10 cm (%), and  $i$  and  $j$  are coefficients solved for using linear regression analysis in SAS. The measured soil respiration data collected by the LI-8100 was the dependent variable needed to create estimates for the  $i$  and  $j$  coefficients. This model is similar to the linear model described by Chen et al. (2011), but one notable difference is apparent. For example, we attempted to use the linear model without converting soil moisture content into relative soil water content. This model was then applied to our seasonal soil moisture and soil temperature data, and then compared with our NEE flux data for only the K2A watershed, as the C3SA watershed does not contain an EC system to compare fluxes. Soil respiration data from the previous K2A growing season were included in our model so that the model simulates expected respiration values for the treatment, rather than just a specific growing season.

#### 3.2.4 Support measurements

The vegetation phenology at K2A watershed was monitored using digital photographs (Richardson et al, 2007). Digital photographs of the plant canopy were taken at K2A every 15 minutes, between 10 AM and 5 PM, using a digital camera (Trail camera – 4 megapixel,



Bushnell). The camera was mounted to the original EC system's aluminum tower. These photos were processed using a MATLAB function provided by the PhenoCam network ("PhenoCam Tools", 2016) to find the green chromatic coordinate (GCC) of the canopy, which was used in this experiment as a surrogate for describing the canopy green-up vigor and canopy senescence. A grey reference panel was used to ensure the red-green-blue channels of the camera were not experiencing signal drift. The reference panel's grey color is expected to create a near constant GCC value because of the equal distribution of red, blue, and green color signals that a grey panel reflects. The reference panel was replaced with a larger version on June 15<sup>th</sup>. This helped increase the area of interest that was examinable in our GCC MATLAB program when analyzing the reference panel. The GCC MATLAB program was set to average GCC values over 3 day spans. The camera was set up facing the north direction to reduce the likelihood of photo overexposure due to sunlight. Figure 3.2 depicts an example of one of the photographs taken by our digital camera during the full bloom of the grass canopy (DOY 255, September 11). Photographs were also used to help describe weather conditions, such as cloudy or clear sky conditions and precipitation events.

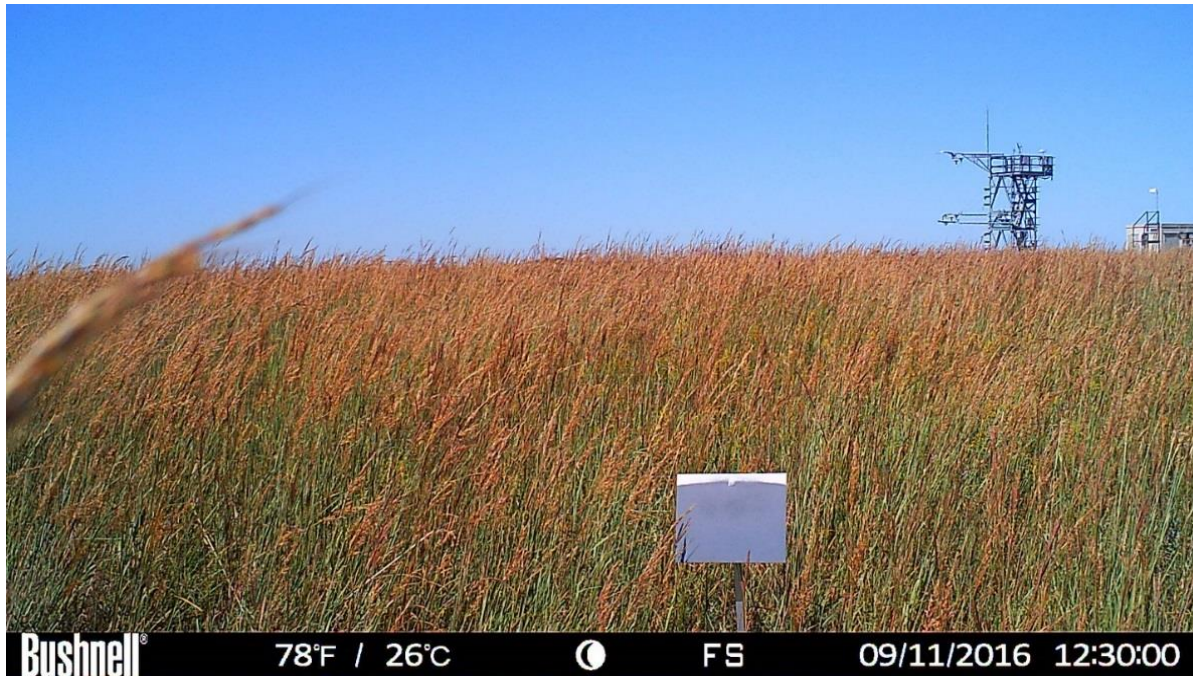


**Figure 3.2 – A sample photograph of the canopy, where several grass species have fully bloomed. A National Ecological Observatory Network tower is on the right side of the picture.**

The maximum height of grass plants, as well as for forb and herbs, which will be labeled as other plants in the results section, were measured for both watersheds on a bi-weekly basis. Each watershed had 9-10 sections measured, each section having 3 repetitions of height measurements. Additional height measurements were made for the woody plants in the C3SA watershed. These height measurements were important for understanding the potential CO<sub>2</sub> source and sink heights of plants relative to our sampling inlets. Additionally, leaf area index was indirectly measured using a plant canopy analyzer (LAI-2000, LICOR Biosciences, Lincoln, NE, USA). LAI was taken of the canopy in each watershed. There were approximately 9 sections measured for LAI, each with 3 repetitions, for each watershed. For the K2A watershed, woody species were not present near the LAI sampling locations. The C3SA watershed had an additional 9 sections measured to identify the LAI of woody species in the watershed. This data

was combined with the plant canopy data gathered for the C3SA. This combination of data is meant help identify the heterogeneity in LAI values within the watershed, which is helpful when wanting to describe physical features of the watershed.

Other variables, such as, rainfall, air temperature and humidity, incoming shortwave radiation, photosynthetically active radiation (PAR), and infrared canopy temperature were measured at the K2A watershed by the K2A original EC system. The 30-year climate normal data and daily average data were obtained from a nearby KPBS weather station (Arguez et al, 2012), located approximately 4 km WNW from the K2A EC systems.

### 3.2.5 Standardizing stable isotopic variations of CO<sub>2</sub> and isotope flux ratio method

Mixing ratio measurements for CO<sub>2</sub> isotopologues were expressed in delta notation using equation 2.1. Mixing ratio vertical gradients of the isotopologues <sup>13</sup>CO<sub>2</sub> and <sup>12</sup>CO<sub>2</sub> were used to calculate the <sup>13</sup>C composition of NEE using the isotope flux ratio approach, as follows:

$$\frac{F^{13C}}{F^{12C}} = \frac{-(K_c \overline{\rho_a}) \frac{d^{13}CO_2}{dz}}{-(K_c \overline{\rho_a}) \frac{d^{12}CO_2}{dz}} \quad (3.2)$$

where  $F^{13C}/F^{12C}$  is the ratio of the net fluxes of the <sup>13</sup>CO<sub>2</sub> and <sup>12</sup>CO<sub>2</sub>,  $\overline{\rho_{air}}$  is the time averaged air density component (kg m<sup>-3</sup>),  $K_c$  is the eddy diffusivity,  $M_a$  is the molecular weight of dry air,  $\frac{d^{13}CO_2}{dz}$  and  $\frac{d^{12}CO_2}{dz}$  are 30-min averaged concentration gradient differences for their respective CO<sub>2</sub> isotopologues. Equation 3.1 can be further simplified since eddy diffusivity is the same for both isotopologues, and that the density of air and molecular weight of dry air for each sample of the isotopologues are equal. With these assumptions,  $F^{13C}/F^{12C}$  is given by:

$$\frac{F^{13C}}{F^{12C}} = \frac{[^{13}CO_2]_{z2} - [^{13}CO_2]_{z1}}{[^{12}CO_2]_{z2} - [^{12}CO_2]_{z1}} \quad (3.3)$$

Where  $[^{13}\text{CO}_2]_{z_2} - [^{13}\text{CO}_2]_{z_1}$  is the measured mixing ratio gradient of  $^{13}\text{CO}_2$  between the two inlets and  $[^{12}\text{CO}_2]_{z_2} - [^{12}\text{CO}_2]_{z_1}$  is the measured mixing ratio gradient of  $^{12}\text{CO}_2$  between the two inlets. The value of the  $F^{13\text{C}}/F^{12\text{C}}$  can also be expressed in delta notation as follows:

$$\delta^{13}\text{C}_F = \left( \frac{F^{13\text{C}}/F^{12\text{C}}}{R_{\text{standard}}} - 1 \right) \quad (3.4)$$

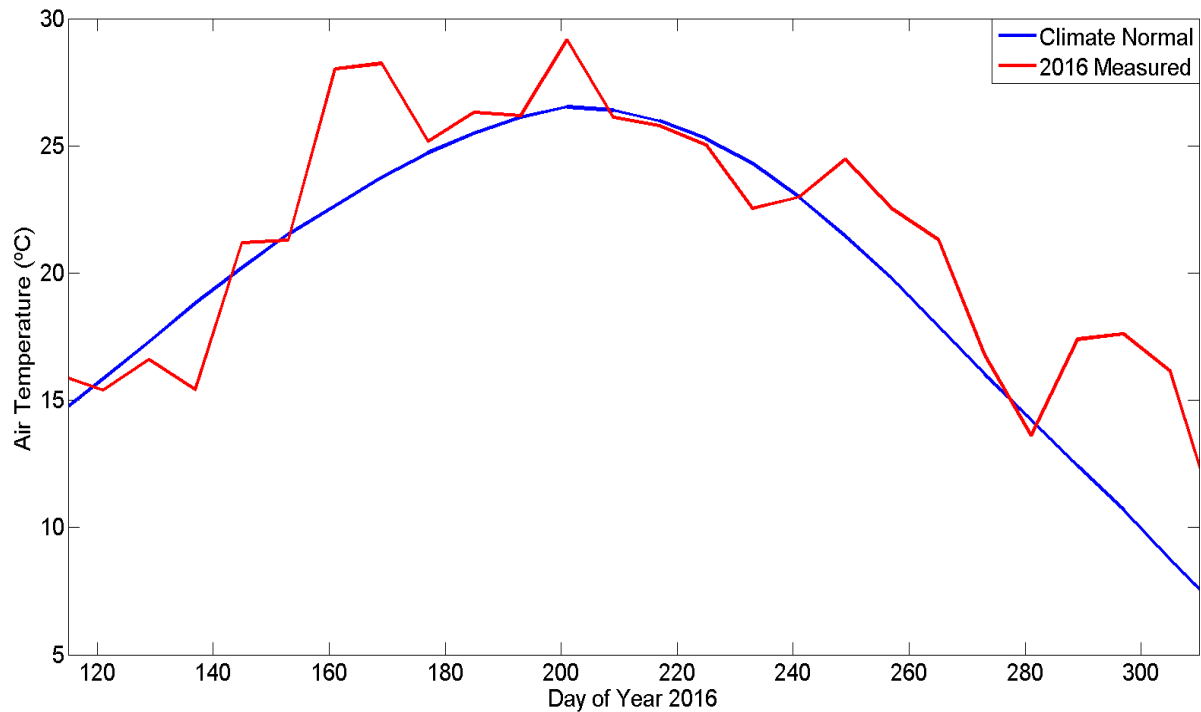
where  $\delta^{13}\text{C}_F$  is the isotopic ratio flux composition in delta notation described in per mil (‰) and  $R_{\text{standard}}$  is the isotopic ratio of the VPDB,  $^{13}\text{C}/^{12}\text{C} = 0.0112372$ .

### 3.3 Results and discussions

#### 3.3.1 Site environmental conditions

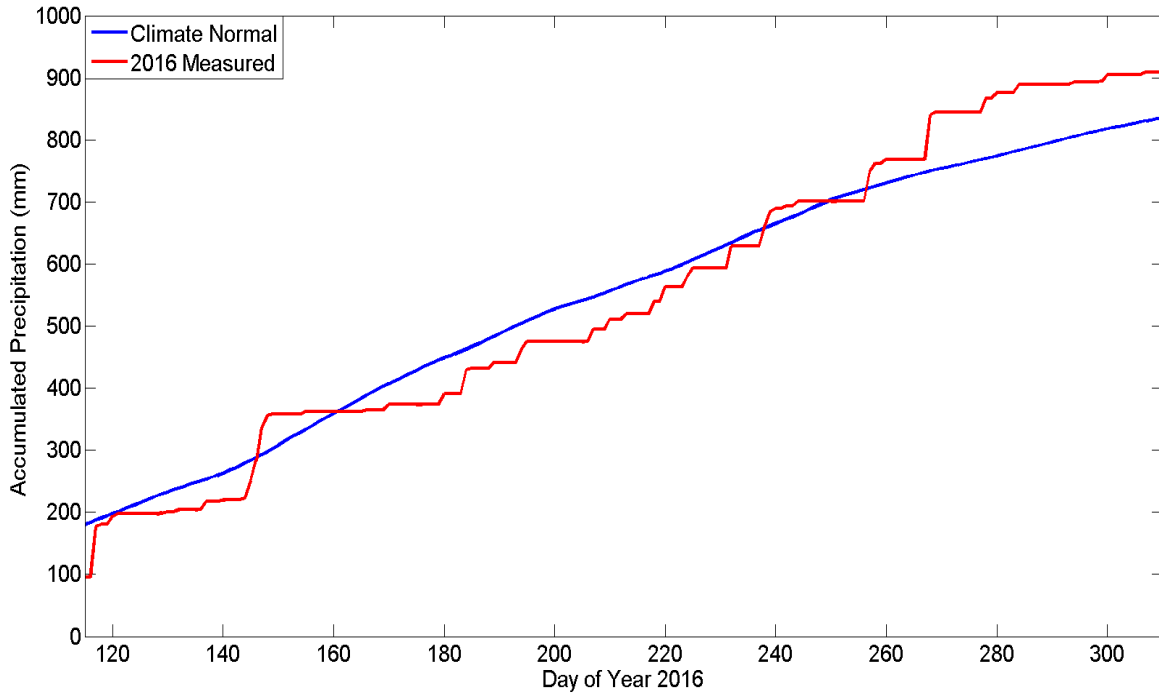
Figure 3.3 shows 8-day temperature average values collected at the KPBS weather station during the experimental period and over a 30-year period ('Daily averages', NOAA).

Temperature data show that winter, spring, and summer months were higher than the climate average temperatures. Warming periods such as this could lead to earlier plant emergence and budding times (Cleland et al, 2006). In some instances, such as between DOY 139 to 154, the 2016 average temperatures are relatively close to the average climatological normal values.



**Figure 3.3 – KPBS weather station’s 8-day temperature averages from 1981-2010 and the 2016 KPBS weather station’s 8-day temperature readings (°C).**

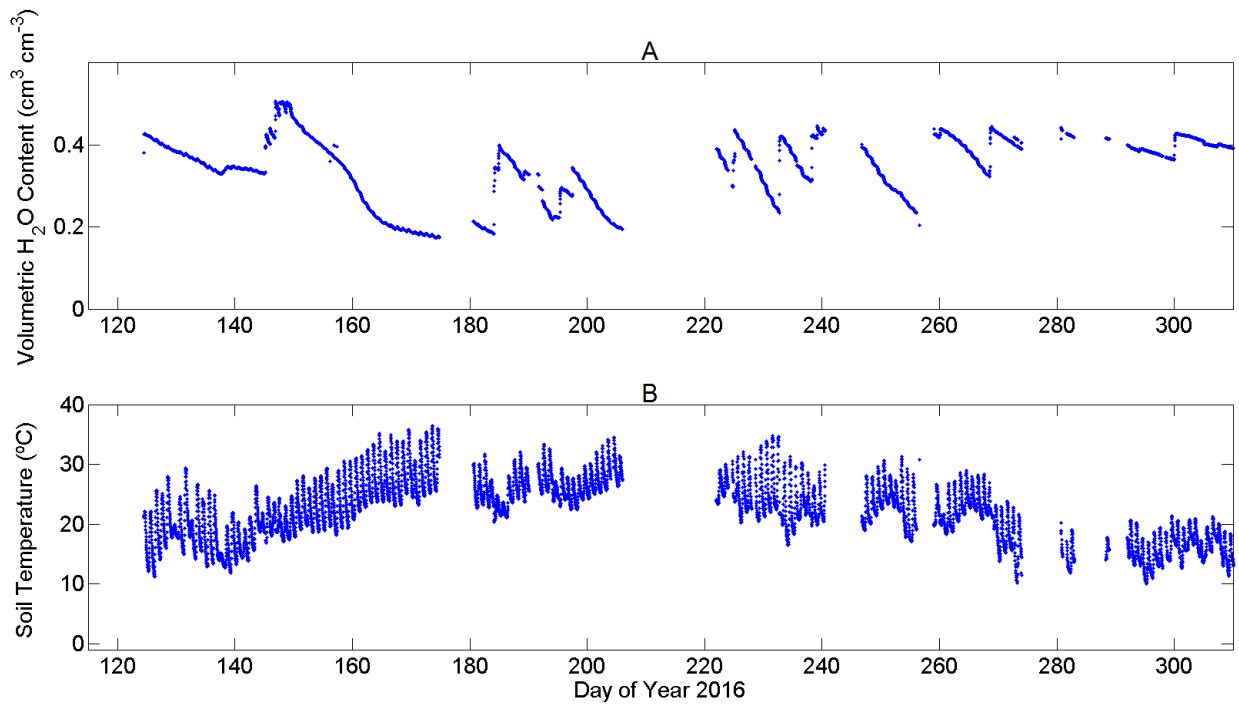
Figure 3.4 shows numerous intense precipitation events often created periods through the growing season with greater than climate average cumulative precipitation, but there are also periods of cumulative deficits. There is a clear difference in accumulated precipitation between the 2016 season and the climatological normal during parts of the mid spring, such as between DOY 149 to 153. It must be noted that daily-accumulated precipitation data provided is from the KPBS weather station and not the K2A weather station. This is because the K2A station was not actively monitoring precipitation data prior to the start of the sampling season and does not have the capability to effectively measure snowfall. Independent tests reveal that the intensity of rainfall events early in the sampling season were reasonably similar, however later on in the season the K2A station’s rain gauge was less reliable because of data gaps caused by power problems associated with the station’s datalogger.



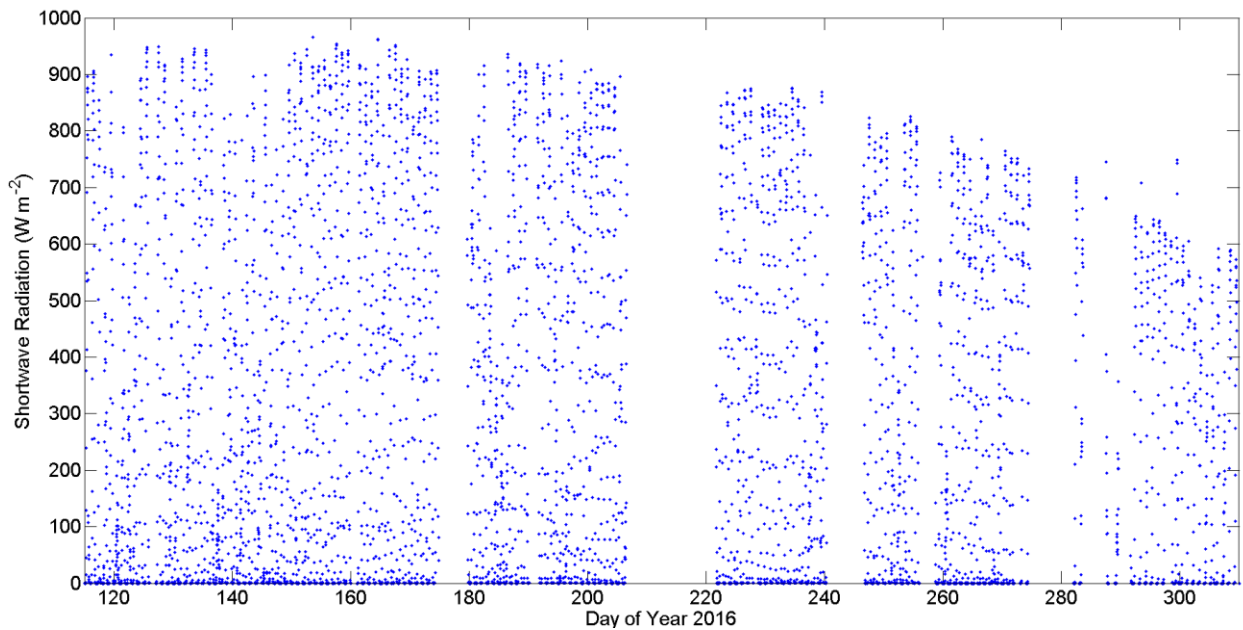
**Figure 3.4 – The KPBS weather station’s average cumulative precipitation normal totals (mm), from 1981 – 2010, and the KPBS weather station’s 2016 accumulated precipitation totals (mm)**

Figure 3.5 shows the volumetric water content and soil temperature readings, respectively, over the course of the growing season. As shown in Figure 3.5A, peak water content occurred at approximately DOY 146. A dry down period soon followed until roughly DOY 181, but realistically there should be an increase in the water content prior to this because Figure 3.4 shows that there was a series of periods were accumulated precipitation events from DOY 175 to DOY 185. The missing data gaps in 3.5A and 3.5B prevented us from seeing the spike in water content before DOY 181. Figure 3.5B shows that soil temperature had sharp increase in temperature from DOY 127 to DOY 134. Based on photographs, and measurements of incoming shortwave radiation (Figure 3.6), this spike in soil temperature could be related to the cloud conditions being mostly clear during this time interval, therefore the incoming solar radiation could be high compared to days where clouds are present. Additionally, the canopy had

not yet reached closure, allowing direct sunlight to warm the soil surface instead of being intercepted by the plant canopy. Shortwave radiation had an initial spike in values approximately a day or two before the spike in soil temperatures. After the initial spike in soil temperature there was a brief span of days consisting of mostly cloudy conditions, where altostratus clouds dominated most of the cloud types. These cloudy conditions influenced solar radiation and likely contributed to the relatively large drop off in soil temperatures around DOY 140. Soil temperatures were at their maximum near DOY 168 through DOY 174. Soil temperature would start to decrease after this time, until DOY 230 to DOY 234. During this time, the temperature had a brief increase during the daytime period because of clearer skies during the previous days. Many of the periods of lower soil temperatures coincided with periods of recent precipitation events and increases in water contents. This correlation could be caused by numerous things. Notably, incoming solar radiation after rainfall events may be used to heat up and vaporize the water that was deposited by the precipitation events, thereby reducing the energy available to heat up the soil. We can use latent heat flux to monitor how much energy is being used to vaporize the water as discussed in Section 3.3.4



**Figure 3.5 – (A) 30-minute average volumetric water content ( $\text{cm}^3 \text{cm}^{-3}$ ) and (B) 30-minute soil temperature measured at 10 cm depth at the K2A watershed.**



**Figure 3.6 – Half-hourly values of shortwave radiation ( $\text{W m}^{-2}$ ) as measured by a pyranometer (LI200R, LICOR Biosciences, Lincoln, NE, USA).**



### 3.3.2 Vegetation measurements

Plant phenology for the K2A site was assessed by examining the green chromatic coordinate (GCC) values from digital photographs. This GCC data are provided in Figure 3.7. Values of GCC increased sharply between DOY 108 through 135 (April 17 - May 14), and peaked around DOY 150 (May 29). The sharp increase in GCC may be attributed to the green up time of plants in this ecosystem. A sharp drop in GCC occurred during DOY 160. This sharp drop is attributed to an inherent problem in the methodology. Since the averaging interval is 3 days long, it does not describe the GCC values in-between the 3 day spans. An independent investigation reveals that signals during the drop off had periods where GCC values were abnormally low. These abnormal values appear to be caused by a community of plants that look noticeably less green compared to neighboring vegetation. This community may have experienced wilting or the community was composed majorly of plant species that do not exhibit as much greenness as surrounding plant species. Based on digital photographs, canopy senescence started for a large majority of the grass species around the end of September (DOY 266 to DOY 268). GCC values did not drop sharply during the senescence period. This was likely caused by the grass species' lower leaves remaining green until roughly late November. Non-grassy plant species in the watershed appeared to remain green later in the year as well, which may have contributed to the steady decline in GCC values.

Plants often would grow in front of the camera's line of sight to the reference panel, thereby influencing our ability to ensure the camera was not drifting in its red, green, and blue channels. Future recommendations include using an even larger reference panel and to install the panel closer to the camera. This setup would help reduce the likelihood of plants contaminating the GCC signal of the reference panel. In addition, a higher quality camera may be necessary to

provide better picture resolution, allowing for more of the canopy to be sampled and better color balance. A camera is also needed for the C3SA watershed to provide a similar analysis for the phenology of the canopy. A panoramic camera could be especially useful for this watershed, because the canopy is much more heterogeneous in terms of plant species compared to the K2A canopy. Nearby trees and sedges could have different green-up and senescence times compared to grasses in the K2A watershed, which could influence our ability to better analyze our flux result comparisons.

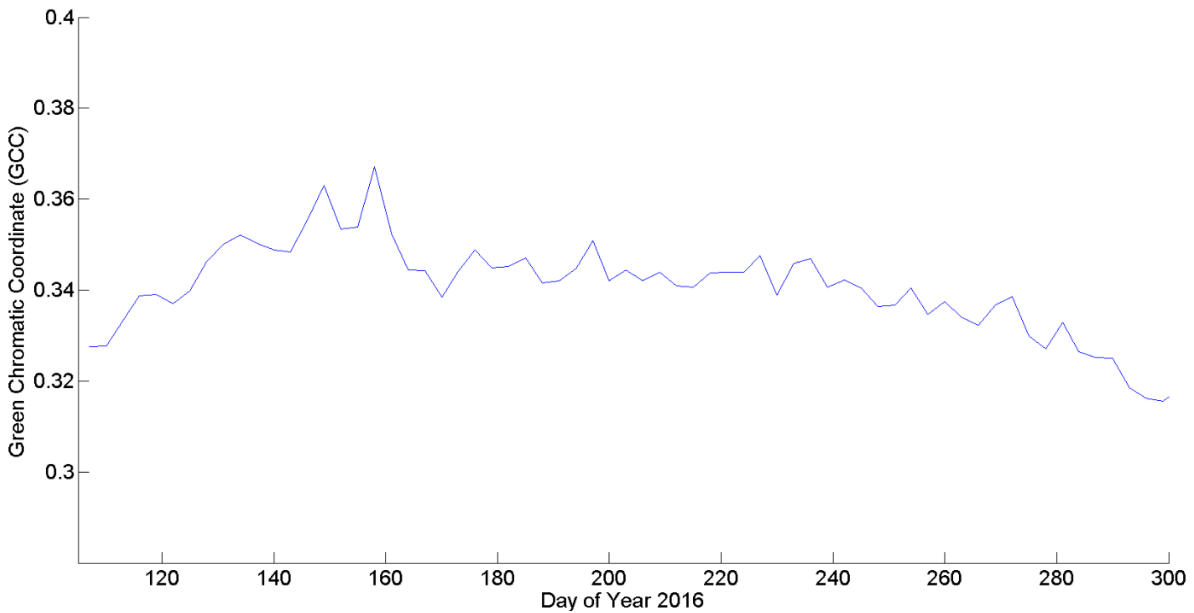


**Figure 3.7 – 3-day average green chromatic coordinate (GCC) values obtained from digital photographs taken at the K2A watershed in 2016.**

Plant maximum height measurements are plotted in Figures 3.8 and 3.9. The grass plants had a relatively fast increase in their heights around DOY 215 (August 2). Our digital photographs around this date time reveal that the grass plants were starting to reach boot stage. They then quickly started to head out. As expected for the grass plants, full canopy bloom accompanied the average maximum grass heights on DOY 255 (September 11), which was shown earlier in Figure 3.2. A shift in the canopy GCC was expected during this time, but the

shift was more apparent 3-4 days after full canopy bloom (Figure 3.2). The relatively large standard deviation values in the grass plant height measurements is believed to be primarily associated with significant height differences between grass plant species, such as little bluestem and indiagrass. Indiagrass tended to have higher maximum heights, while little bluestem was typically shorter in stature. The other non-grass plant heights remained fairly close to one another compared to the grass plant species respective heights.

Figure 3.9 shows the maximum heights of the grass plants, woody species, and the herbs and forbs that were noticeably below the grass plant maximum heights. The grass plant maximum heights in the C3SA watershed typically had greater standard deviation values throughout the season compared to the K2A grass plant maximum heights standard deviation values. This is likely a result of grazing in the C3SA watershed. Cattle could roam near the sample sections and, assumingly, consumed or stomped on plants where height measurements were taken. The effects of grazing are reflected during the last sampling visit on DOY 281 as a notable decrease in the grass plant top heights was observed. Although there was a drop off in plant heights observed during the last sampling of heights for the K2A watershed, the magnitude in change between plant heights from the previous sampling visit is much more apparent in the C3SA watershed. This change in heights for the last sampling visits is roughly equal to 0.19 cm for C3SA, which is greater than the ~0.02 cm change in heights observed for the K2A watershed. Plants in the C3SA watershed that were below the grass tops were relatively uniform in height and showed a decline in heights similar to the K2A's heights of plants below the grass tops. For future sampling, cages might be required to isolate plant communities from cattle intrusion in order to find out how grazing impacts plant heights for this watershed.

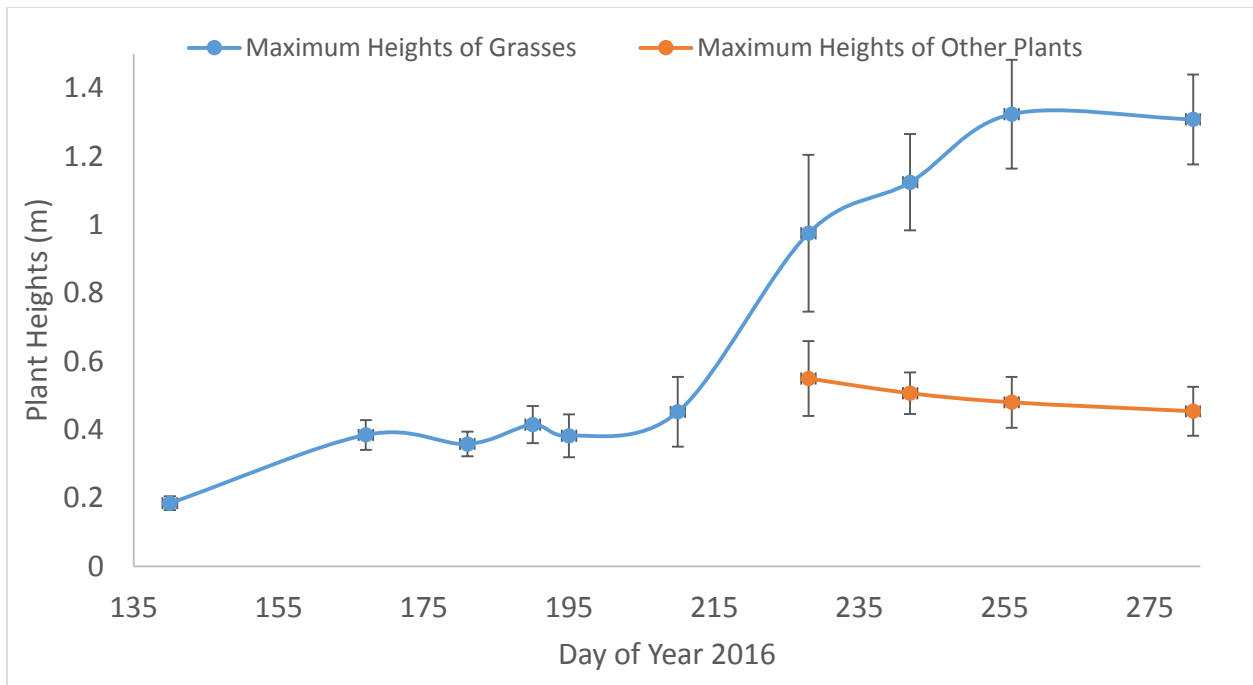


**Figure 3.8 – Plant heights during the growing season for the K2A watershed. Error bars in this chart depict the standard deviation found for each sampling period.**

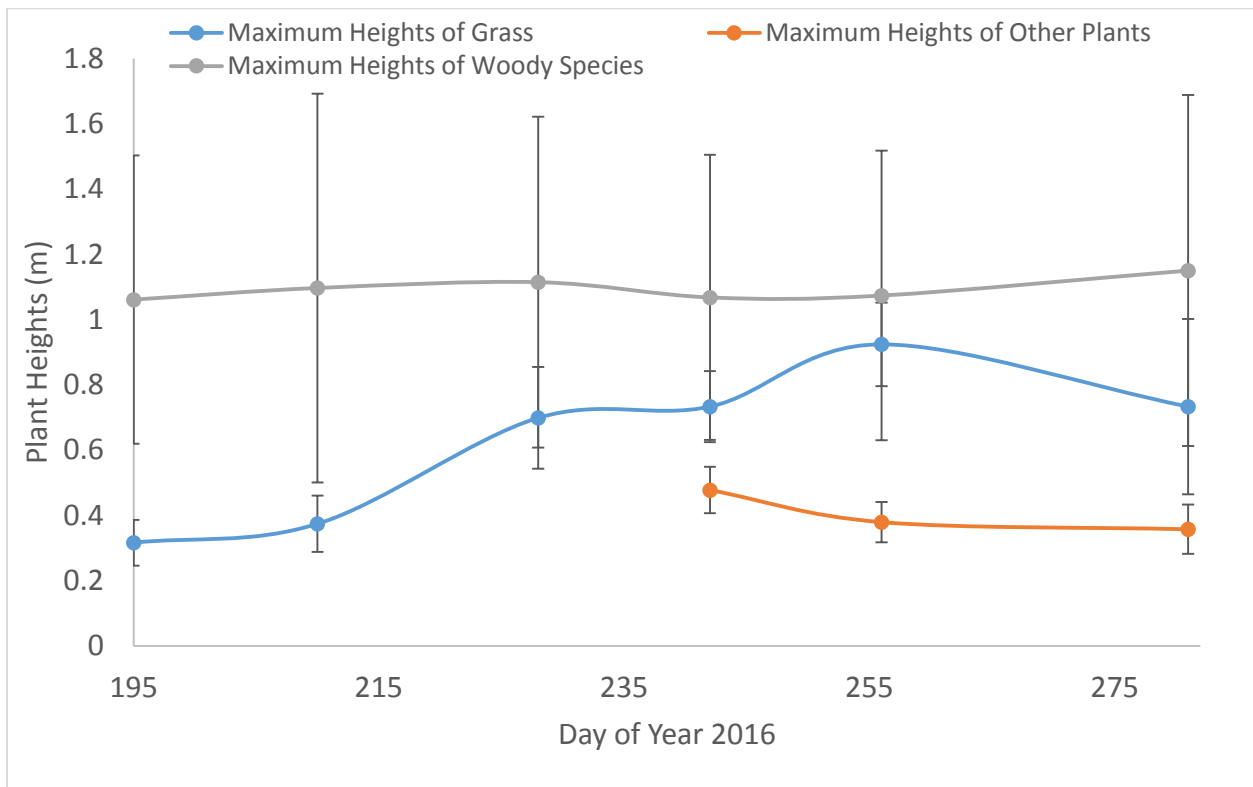


**Figure 3.9 – Plant heights during the growing season for the C3SA watershed. Error bars in this chart depict the standard deviation found for each sampling period.**

Figure 3.10 displays the LAI values for each watershed and the standard deviation values for these LAI values, respectively. Figure 3.10A shows that when including woody species into the LAI measurements, the LAI values in the C3SA watershed had a relatively higher LAI value compared to the canopy LAI values that did not include woody species for both the K2A and C3SA watersheds. The K2A watershed appears to have slightly more LAI over the duration of the sampling period, but one data point seems inconsistent with this trend. On DOY 222, the C3SA and K2A canopy LAI values were nearly equal to one another and is likely just a coincidence in the data. Figure 3.10B reveals that the LAI standard deviations for the C3SA canopy, when including woody species, is very high compared to the canopies without woody species for both K2A and C3SA. Many of the woody species plant stands that were measured for LAI relatively shorter tree stands and bushes nearby. Many of the woody species and bushes identified during LAI measurements were *Cornus drummondii* (dogwood) and *Rhus glabra* (smooth sumac), respectively. The standard deviation for the canopies without woody species in both the K2A and C3SA were relatively close to another throughout the sampling campaign. In addition, Figure 3.10B shows that relatively high amounts of standard deviation occurred when including woody species with other plants in the C3SA watershed. This can be caused by many factors, such as not sampling the LAI in the exact positions every sampling period. In addition, many tree species have different growth patterns and responses in the environment to the non-woody species. A much more effective methodology for collecting LAI is needed to better describe the physical characteristics of the canopy.

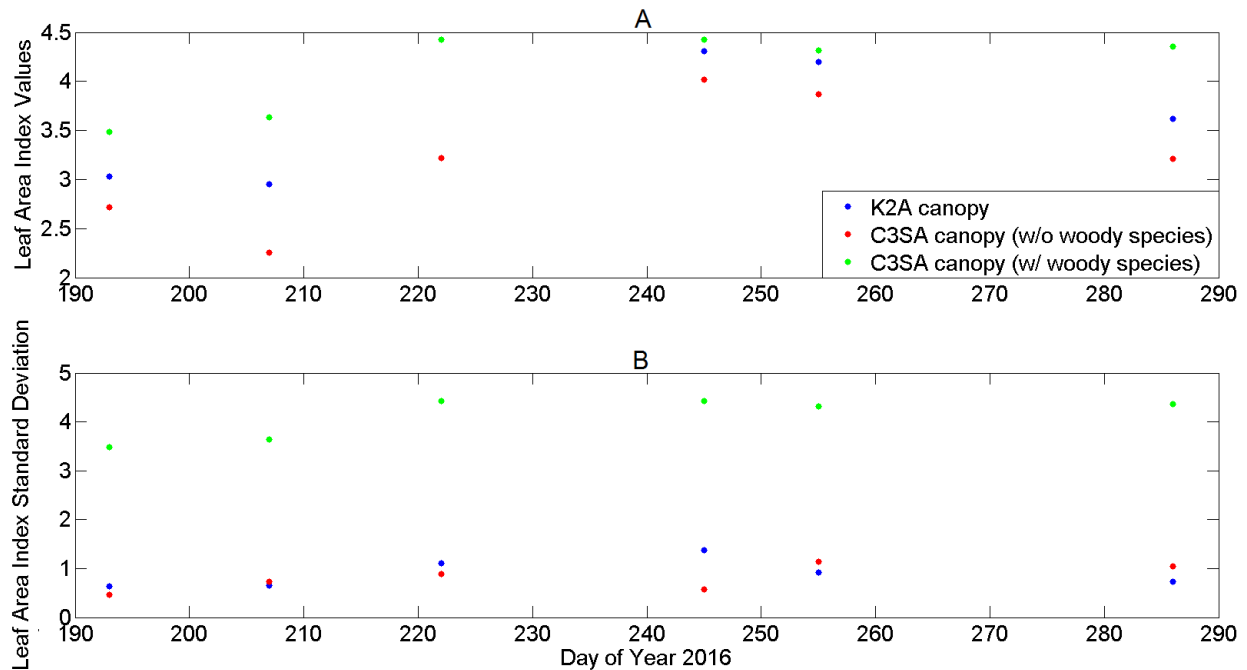


**Figure 3.10 – (A) Leaf area index values for the K2A watershed and C3SA watershed and (B) Leaf area index standard deviation values for the K2A watershed and C3SA watershed.**

### 3.3.3 Soil CO<sub>2</sub> measurements

Figure 3.11 displays the soil respiration data as estimated by our linear regression model as described in Section 3.2.3. In Appendix D, we find that the model has a noticeable correlation ( $R^2_{\text{adjusted}} = 0.6692$ ) with the measured efflux values when using soil temperature and moisture content as our independent variables. The model also adjusts readily to the changes in the soil moisture content and temperature, much like what would be expected for real soil CO<sub>2</sub> fluxes. More real time data point comparisons with modeled outputs could help instill confidence in the model's ability to predict soil CO<sub>2</sub> efflux. Relative water content might be a more appropriate variable to assess instead of volumetric water content, as described by Norman et al. (1992). Another model that Norman et al. (1992) proposed includes the use of LAI measurements. Tests are needed to determine if Norman et al. (1992) models have higher  $R^2_{\text{adjusted}}$  values compared to our linear model.

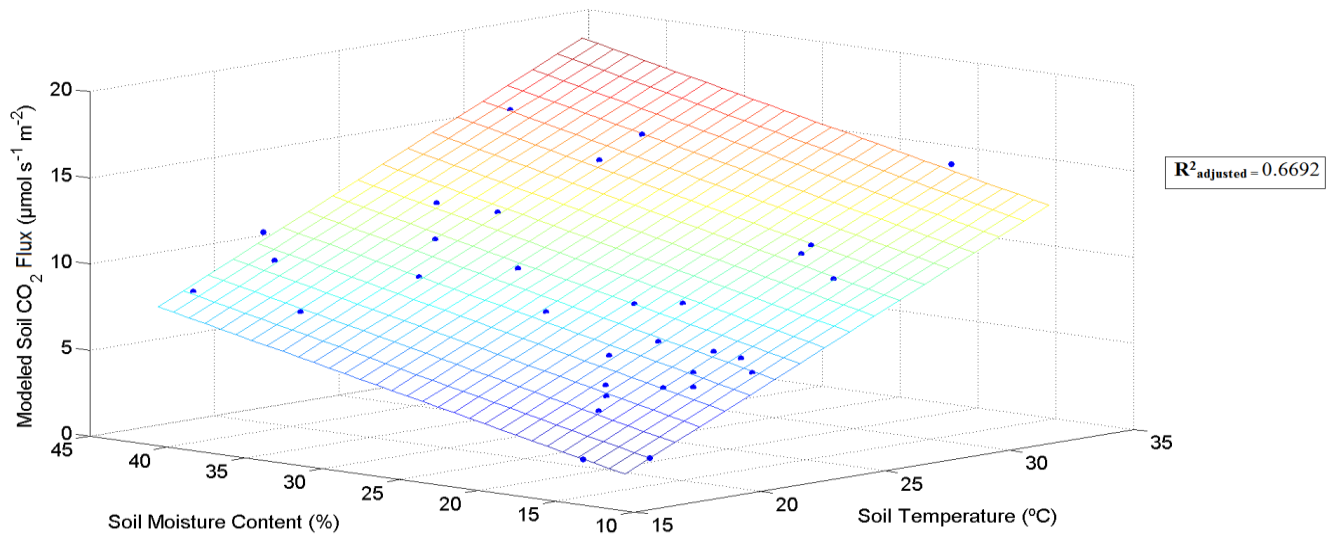


**Figure 3.11 – A multiple linear regression plot displaying the measured soil moisture content (%) and measured soil temperatures (°C) relationship with modeled soil CO<sub>2</sub> flux the dots are the measured independent variables and the colored grid is our linear regression plane.**

#### 3.3.4 Ecosystem flux measurements

Figure 3.12 shows half-hourly values of latent heat fluxes during the growing season. Latent heat flux typically followed an increase and decrease in its values during wetting and drying cycles. For example, DOY 150's noticeable precipitation event increased the latent heat energy until roughly DOY 160. Other peaks in these latent heat flux values appear during days following precipitation events, such as the precipitation events during DOY 175 to DOY 180 and DOY 222 to DOY 224. The overall trend in latent heat was downward from around DOY 182 until the end of the sampling campaign. Cloudy skies likely contributed to varying degrees of a lagged response of latent heat flux after a precipitation event, cloudy days could block the solar radiation that helps drive the latent heat flux.

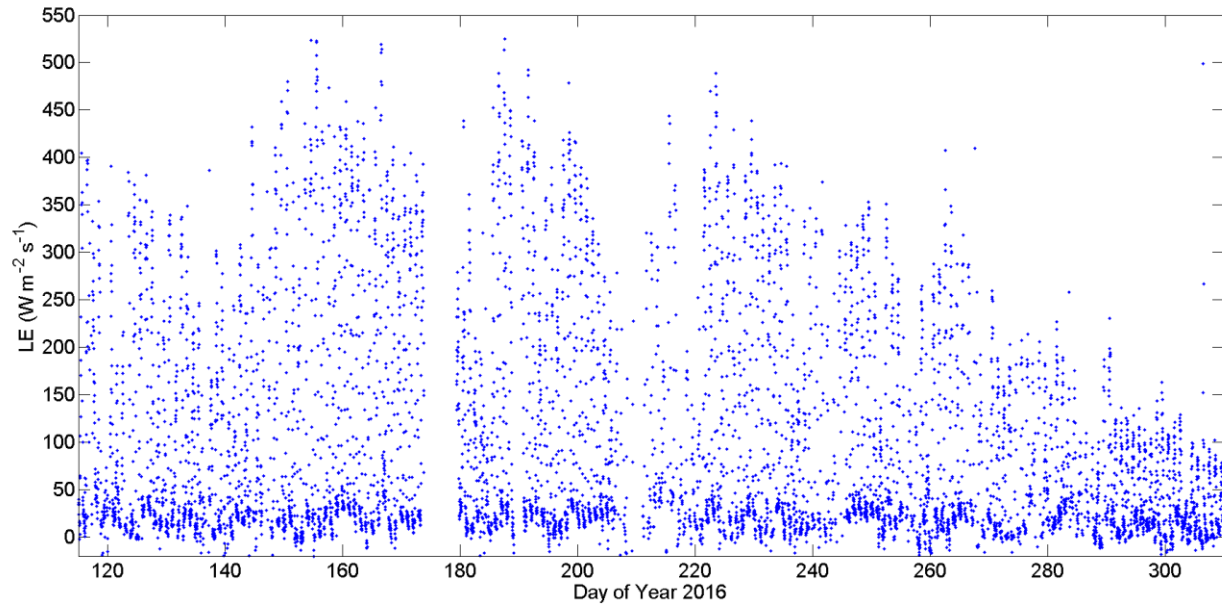


**Figure 3.12 – Half-hourly values on latent heat fluxes (LE,  $\text{W m}^{-2} \text{s}^{-1}$ ) in the K2A watershed during the 2016 growing season.**

Values of NEE and modeled soil  $\text{CO}_2$  efflux for 30-min periods are provided in Figure 3.13. NEE values were positive during the nighttime due to the absence of photosynthesis activity. Values of the modelled soil  $\text{CO}_2$  fluxes appear to be close in magnitude to NEE values during the nighttime early in the sampling campaign, suggesting that soil  $\text{CO}_2$  is a major component of the nighttime NEE values. It must be mentioned that the modeled soil  $\text{CO}_2$  values are at their minimum during the night because of soil temperatures reaching their minimum. This is expected and is caused by radiative cooling processes at night that reduce the soil temperature. The soil moisture variable appears to be a big limiting factor in the modeled soil  $\text{CO}_2$  flux values when compared against the NEE values, but describing this relationship with decreasing or increasing soil moisture content is not straightforward. There are instances when soil moisture is relatively high and the soil  $\text{CO}_2$  flux values are relatively close to the NEE flux values (DOY 155). In other instances where relative soil moisture content is present, the soil  $\text{CO}_2$  flux



measurement is lower than the NEE flux values (DOY 266). This is likely just the result of the coupling between soil moisture content and soil temperature, and how one of these variables, namely precipitation, can be so much more variable compared to the other, such as soil temperatures. Daytime NEE values are negative during the growing season because of vegetation performing photosynthesis. These daytime NEE values reach their greatest (negative) amplitude during DOY 160 and DOY 197. After DOY 197, there is a steady decline in the daytime NEE values. This is likely caused by the growth, development, and eventual senescence of the canopy.

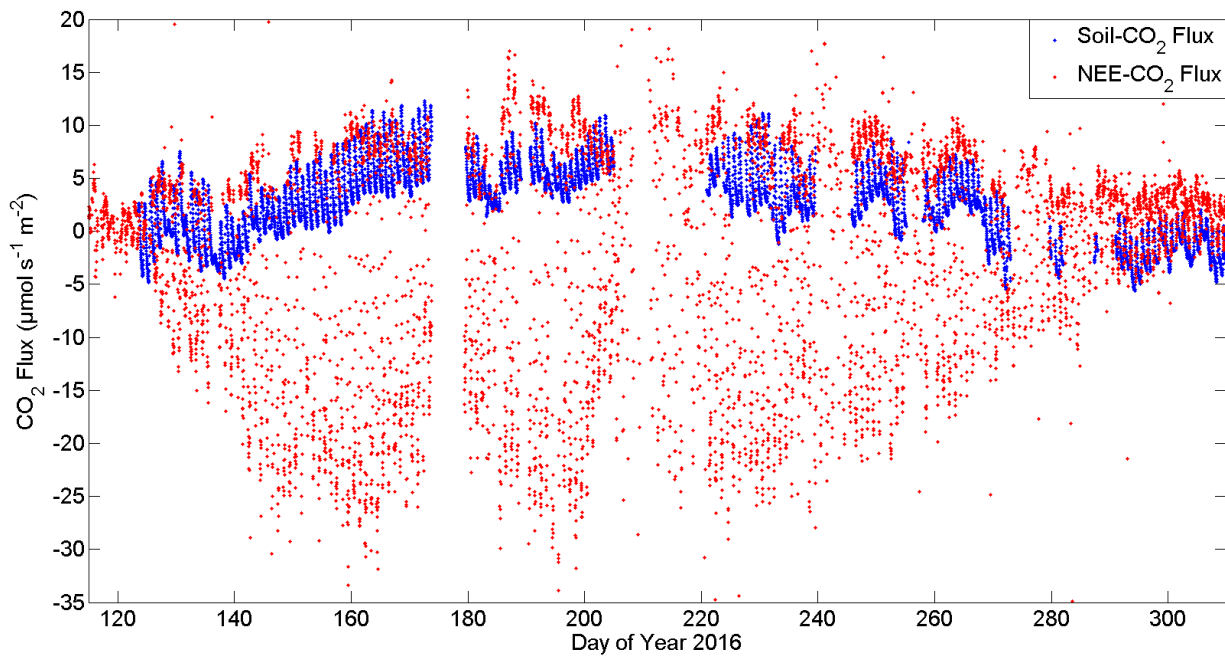


**Figure 3.13 – Half-hourly values of NEE for the K2A watershed compared to the modeled soil CO<sub>2</sub> respiration data.**

### 3.3.5 Temporal dynamics of the isotope exchange in grazed and ungrazed watersheds

Figure 3.14 shows the diel cycles of half-hour averages for the CO<sub>2</sub> mixing ratio and δ<sup>13</sup>C, respectively, measured above the plant canopy in early June. Only one week of data is shown to help enhance key points of interest on the graph. Showing a longer time frame might

increase the scaling of the graph, which could reduce the amount of detail that would be more apparent at a smaller scaling. Diel cycles of CO<sub>2</sub> mixing ratio follows cycles of daytime vegetative photosynthesis and nighttime ecosystem respiration building up in the nocturnal boundary layer.  $\delta^{13}\text{C}$  values also exhibit a similar pattern that is influenced majorly by the day and night processes, except during the daytime the  $\delta^{13}\text{C}$  is increasing and at night the  $\delta^{13}\text{C}$  signal is decreasing. This is likely caused by the uptake of <sup>12</sup>CO<sub>2</sub> plants in either watershed ecosystem, creating a relative enrichment in the  $\delta^{13}\text{C}$  signal. At night time, some of the previously sequestered <sup>12</sup>CO<sub>2</sub> molecules, in the form of carbon substrate, are metabolized and released during respiration back into the canopy. This release of <sup>12</sup>CO<sub>2</sub> starts to shift the  $\delta^{13}\text{C}$  signal to being more depleted.

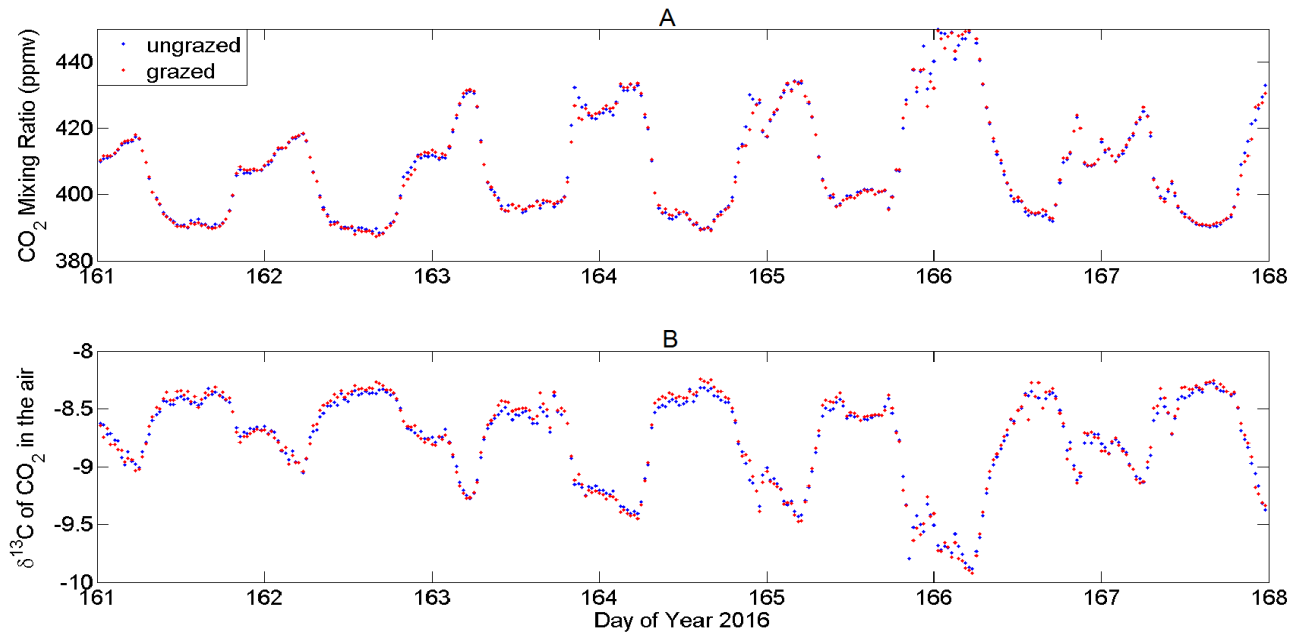


**Figure 3.14 – Half-hourly average values of: (A) CO<sub>2</sub> mixing ratio and (B)  $\delta^{13}\text{C}$  of atmospheric CO<sub>2</sub> at the two watersheds. The values were derived based on the concentration readings from the top sampling inlets of the ungrazed and grazed watersheds (1.52 m and 1.5 m, respectively).**

Values of the CO<sub>2</sub> mixing ratio were mostly similar for both the ungrazed and grazed watersheds during this one-week period, while the  $\delta^{13}\text{C}$  signals were noticeable different during

the same time frame. The grazed watershed appears to have a relatively more enriched  $\delta^{13}\text{C}$  signal during the daytime compared to the ungrazed watershed. At nighttime, the reverse is true. This may reveal that, during the daytime, the typically  $\text{C}_4$  dominant community in the ungrazed watershed is sequestering relatively more of the  $^{13}\text{CO}_2$  molecules compared to the  $\text{C}_3$  community in the grazed watershed. This creates a depletion in the  $\delta^{13}\text{C}$  signal of the ungrazed watershed. The nighttime reveals that the  $\delta^{13}\text{C}$  signals reflect the respiration of the sequestered isotopic  $\text{CO}_2$  molecules. Since the  $\text{C}_4$  community had previously uptaken more of the  $^{13}\text{CO}_2$  during the day, the subsequent metabolism of the substrates that were made using the  $^{13}\text{CO}_2$  molecules reflect a more enriched  $\delta^{13}\text{C}$  signal in the ambient air of the ungrazed watershed. Soil respiration could also be playing a role in the diel changes in  $\delta^{13}\text{C}$ , but it is unclear how at this time.

The  $\delta^{13}\text{C}$  signals became more varying and more depleted towards the end of the week. Soil moisture content may have had an impact on these  $\delta^{13}\text{C}$  signal trends, as according to Figure 3.8A the soil moisture content was starting to wane considerably at the end of Figure 3.14's time frame (DOY 167). However, since we did not have soil moisture sensors installed at the grazed watershed, it is unclear if the soil moisture content of the grazed watershed was decreasingly as equally as the ungrazed watershed. It would be reasonable to assume that both watersheds were possibly experiencing a significant dry down period at the same time, because these sites are within close proximity to one another. It is likely that precipitation events affecting one site will have likely influenced the other. However, soil properties and topography are notably different between the two sites, as noted in the site descriptions. Therefore, soil moisture content could be different between the two watersheds over the course of Figure 3.14's timeline. A much more thorough evaluation of the soil moisture content and its relationship to the plant and soil microbial water demands is needed to better describe plant and soil contributions to the  $\delta^{13}\text{C}$   $\text{CO}_2$

signal. This will require soil moisture probes installed at deeper depths characterize accurately the soil moisture content status of the soil surrounding plant roots. Also, isotope analysis of the soil respiration  $\delta^{13}\text{C}$  values will help us identify how much the soil respiration component is contributing to the  $\delta^{13}\text{C}$   $\text{CO}_2$  measured in the watersheds.

The isotopic composition of NEE was determined using the isotope flux ratio method (see section 3.2.4). Previous studies show that small gradients of mixing ratios increase the uncertainties of  $\delta^{13}\text{C}_F$  of NEE estimates (Griffis et al, 2004; Santos et al, 2012). Therefore, we assessed the minimal gradient threshold needed to retain high quality data and to mitigate noise by analyzing the results presented in Figure 3.15. This figure shows that as our absolute gradients of  $\text{CO}_2$  concentrations become very small, typically less than 1-2 ppmv of  $\text{CO}_2$ , the flux-ratio signal becomes much more variable. Using this figure, we identified that gradients equal to or greater than 3.5 ppmv would provide the high quality data needed to correctly assess the differences in the  $\delta^{13}\text{C}_F$  signal for both the grazed and ungrazed watersheds. Hereafter, references to data being filtered out or being eliminated will simply refer to some data points not having a high enough concentration gradient. MATLAB scripts and functions were programmed to not process data points with too low of concentration gradients. Instead of being processed and used in MATLAB calculations, the MATLAB scripts and functions replace these respective data points  $\delta^{13}\text{C}$ ,  $\delta^{13}\text{C}_F$ , and  $\text{CO}_2$  values with 'Nan' values. These 'Nan' values, or not a number values, are simply placeholders in our data outputs generated by our MATLAB scripts.

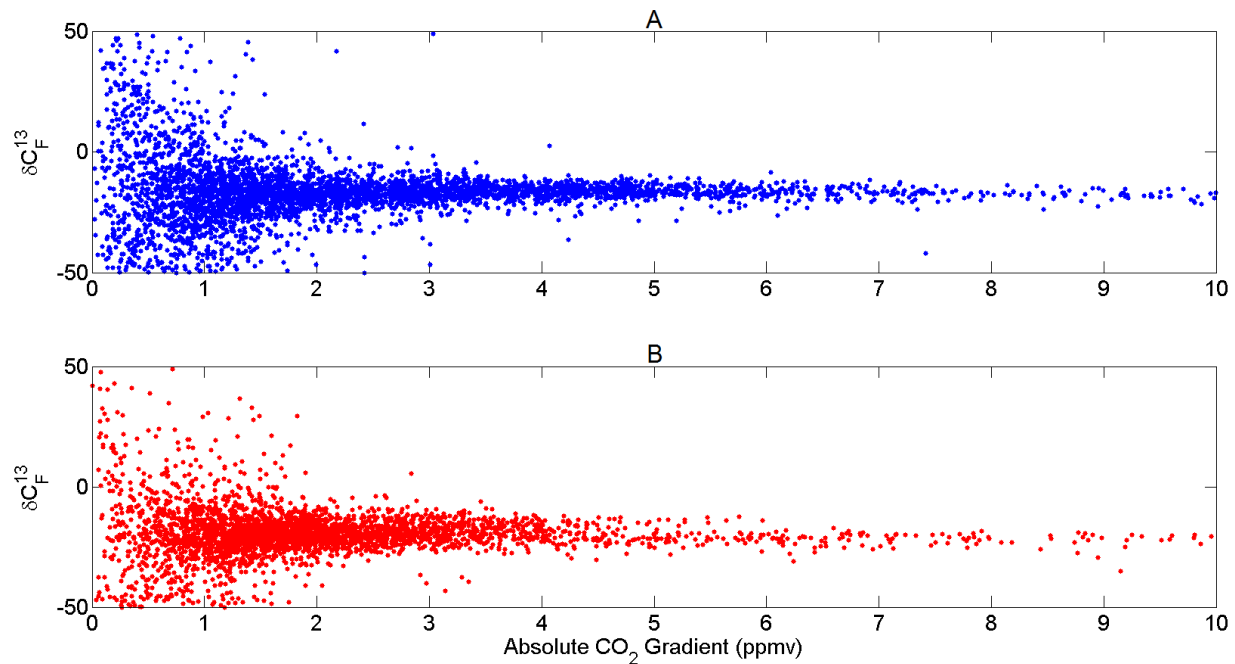


**Figure 3.15 – Relationship between the isotopic flux-ratio signal in delta notation ( $\delta^{13}\text{C}_F$ ) versus the concentration gradient of  $\text{CO}_2$  in absolute form for the ungrazed (A) and grazed (B) watersheds.**

Figure 3.16 shows the ensemble half-hour average of the  $\delta^{13}\text{C}_F$  composition of NEE for the mid-summer portion and early fall parts of the sampling campaign. The time scales are representing the ensemble average of each half-hour interval in a day over a 30-day span. Both Figure 3.16A and 3.16B show a consistent enrichment in the  $\delta^{13}\text{C}$  signal of the ungrazed watershed compared to the grazed watershed, indicating that  $\text{C}_4$  plants might be having a greater impact on the movement of  $\text{CO}_2$  in the ungrazed watershed compared to the grazed. However, it is apparent that the  $\delta^{13}\text{C}_F$  signals of both watersheds are missing during the daytime in Figure 3.16B and only for the grazed watershed during the mid-summer  $\delta^{13}\text{C}_F$  analysis shown in Figure 3.16A. These data gaps are likely caused by our previously created gradient filter removing data points from the dataset because they have too low of gradients. However, there is uncertainty as to why the ungrazed signal does not become filtered out during the day for the mid-summer

analysis, much like the grazed data and its data gaps during the daytime for both the mid-summer and early fall. It might be possible that values for the ungrazed system are stronger than the concentration gradient threshold of 3.5 ppmv during the daytime of the mid-summer period. In the other instances where gaps in data are apparent, it is likely that well-mixed conditions are present and creating too small of CO<sub>2</sub> gradients between the sampling inlets. This is a result of high turbulence mixing created by daily diurnal heating that breaks up the nocturnal boundary. Figure 3.11 shows that NEE started to decrease in early fall. This may create weak gradients of CO<sub>2</sub> being sampled between the two sampling inlets for either watershed; therefore, the gradients are not strong enough to make the gradient threshold and the  $\delta^{13}\text{C}_F$  values are filtered out.

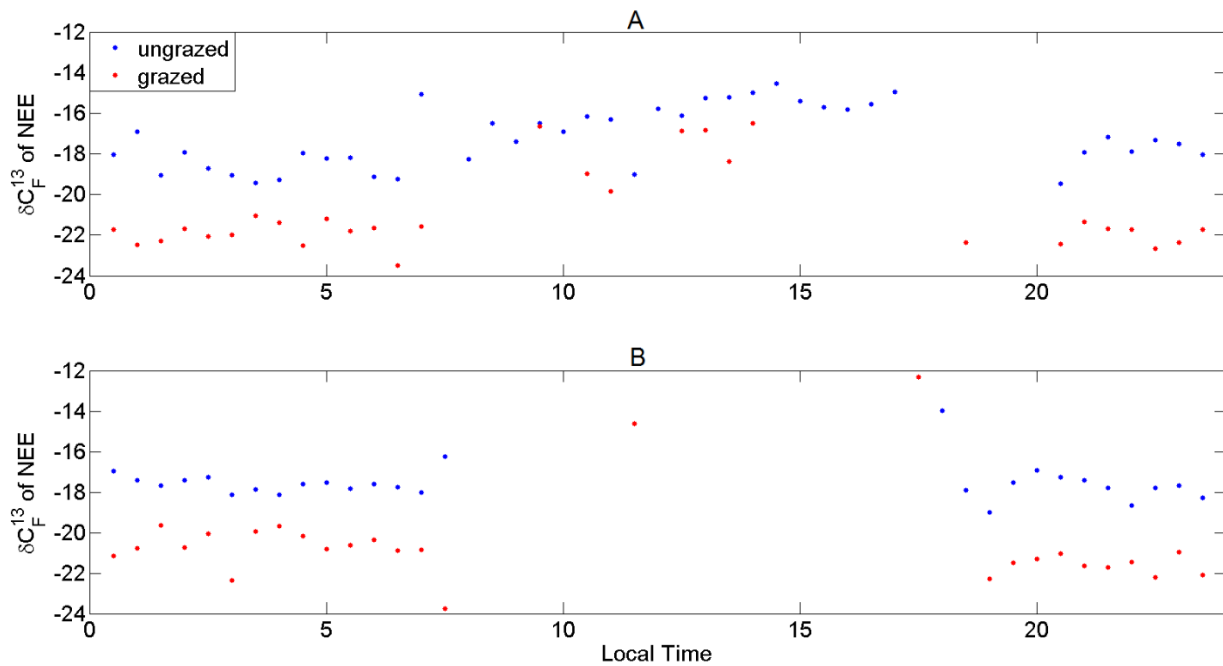


**Figure 3.16 – Half-hourly ensemble average of  $\delta^{13}\text{C}_F$  for 30 day-periods during (A) the midsummer (DOY 162 to DOY 192) and (B) early fall portion (DOY 220 to DOY 250) for the grazed (C3SA) and ungrazed (K2A) watersheds**

Since the nighttime signals appear to be more reliable to analyze, because they tend to not have too weak of gradients and not be eliminated by our gradient threshold filter that is used in our MATLAB data processing script, the average daily night  $\delta^{13}\text{C}_F$  signals were used to

determine if a seasonal trend is apparent. Figure 3.17 displays these nightly values from DOY 100 to DOY 250. This plot shows the 12-hour average nighttime data for a given day of the year. There is a slow shift in both watershed's  $\delta^{13}\text{C}_\text{F}$  night time signals over the course of the growing season. It appears that the ungrazed  $\delta^{13}\text{C}_\text{F}$  signals start to become relatively enriched in its  $\delta^{13}\text{C}_\text{F}$  signal as the season progresses. Lai et al. (2003) found similar results in their work at the Rannells Prairie, a research site near the Konza Prairie Biological Station. They solved for  $\delta_\text{R}$  using a Keeling plot method and collected weekly samples of the ecosystem air using an automated flask collection system. Values from the grazed watershed during DOY 100 to DOY 150 are not available. This is due to the inlets in this watershed not being installed until later on in the season. The ungrazed  $\delta^{13}\text{C}_\text{F}$  signal between DOY 100 and DOY 150 appears to have greater variance compared to later on in the season. This could be attributed to the laser that was used initially in the experiment having more variance. In addition, the canopy at this time was relatively young. As such, even though the data passed our gradient threshold values, the mixing of signals from the atmosphere and young canopy likely contributed to some of the notable variability. The  $\delta^{13}\text{C}_\text{F}$  signal trends for both watersheds started to become more negative later on in the season, as the canopy will have fully senesced. At the time of full senescence, the  $\delta^{13}\text{C}_\text{F}$  signal should mostly reflect that of the heterotrophic soil respiration component of the ecosystem respiration. Since source and sink strength components will have weakened by that point in the growing season, further data analysis could show similar variability in the  $\delta^{13}\text{C}_\text{F}$  signal during DOY 100 to DOY 150 for the ungrazed watershed, but uncertainty exists regarding the prediction of the grazed watershed's  $\delta^{13}\text{C}_\text{F}$  during this period.

There is a noticeable difference between the  $\delta^{13}\text{C}_\text{F}$  values of the ungrazed watershed and the grazed watershed when examining the period of DOY 150 to DOY 250. The ungrazed

watershed has  $\delta^{13}\text{C}_F$  values typically between -21‰ and -16‰, while the grazed watershed has varying, more depleted,  $\delta^{13}\text{C}_F$  signal range between -26‰ and -18‰. Lai et al. (2003) found by that  $\text{C}_4$  plants likely adjust the  $\delta_R$  value in the prairie to be between -17.5 to -13 per-mille (‰), while  $\text{C}_3$  plants were suspected to shift the  $\delta_R$  signal to be more negative than -18 per-mille (‰). The  $\delta^{13}\text{C}_F$  signal in the grazed is comparably more depleted to what Lai et al. (2003) found, while the ungrazed watershed has several instances where the  $\delta^{13}\text{C}_F$  is comparably more depleted.

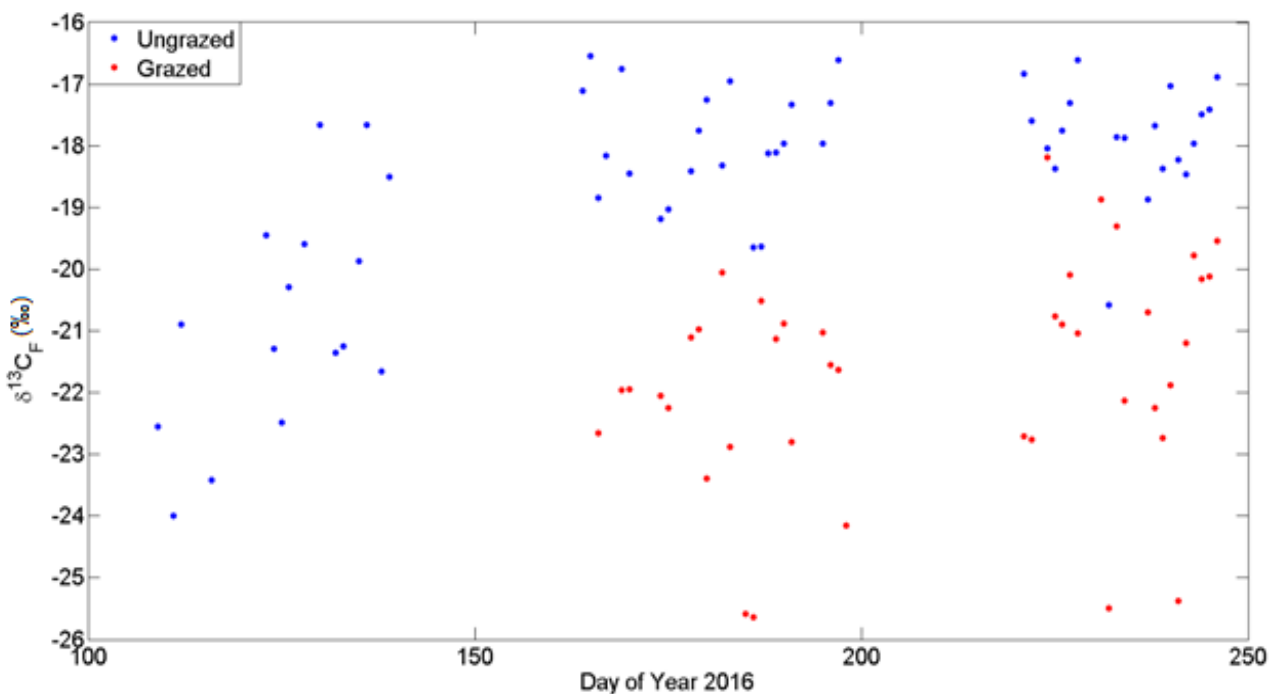


**Figure 3.17 – Nightly average  $\delta^{13}\text{C}_F$  (‰) signal for the ungrazed watershed and the grazed watershed.**

The  $\delta^{13}\text{C}_F$  signal of the grazed watershed appears more varying compared to the ungrazed watershed. Lai et al. (2003) reported that wind direction and wind speed can shift the sources of signals measured by a sampling system, which would affect the variability in  $\delta_R$  values. Since the grazed watershed's  $\delta^{13}\text{C}_F$  value appears to be quite variable over time, an investigation similar to



the one performed by Lai et al. (2003) was conducted. Figure 3.18 displays graphs of wind characteristics related to the  $\delta^{13}\text{C}_F$  for the nighttime values found in Figure 3.17. Figure 3.18A shows that the depleted  $\delta^{13}\text{C}_F$  signal at the ungrazed watershed (K2A) could be associated with the wind direction coming from the south to the southwest. Therefore, there is a weak trend between wind direction and increasingly negative  $\delta^{13}\text{C}_F$  signals for the K2A watershed. Figure 3.18B does not appear to have a consistent pattern in its  $\delta^{13}\text{C}_F$  signal versus wind direction, but it is possible that a weak trend could be interpreted. This weak trend seems to show that winds coming from the south and moving more easterly may enrich the  $\delta^{13}\text{C}_F$  signal. Figures 3.18C and 3.18D appear to show that wind speed is marginally influencing our  $\delta^{13}\text{C}_F$  results. A more thorough investigation into the relationship between wind characteristics and the  $\delta^{13}\text{C}_F$  will likely require the use of a flux footprint model. A flux footprint model can help estimate where our fluxes are originating from across the watersheds. Using the flux footprint model with satellite imagery could help identify clusters of plant communities that are nearby, or far away in some situations, that could be influencing the  $\delta^{13}\text{C}_F$  signals. In addition, there is a need to identify the  $\delta^{13}\text{C}_F$  and  $\delta^{13}\text{C}$  signal of soil respiration in both watersheds, as well find a better way to estimate the strength of the flux generated by soil respiration overtime. Soil respiration isotope analysis could be essential for helping us better understand the variability of the  $\delta^{13}\text{C}_F$  and  $\delta^{13}\text{C}$  signals for both watersheds.

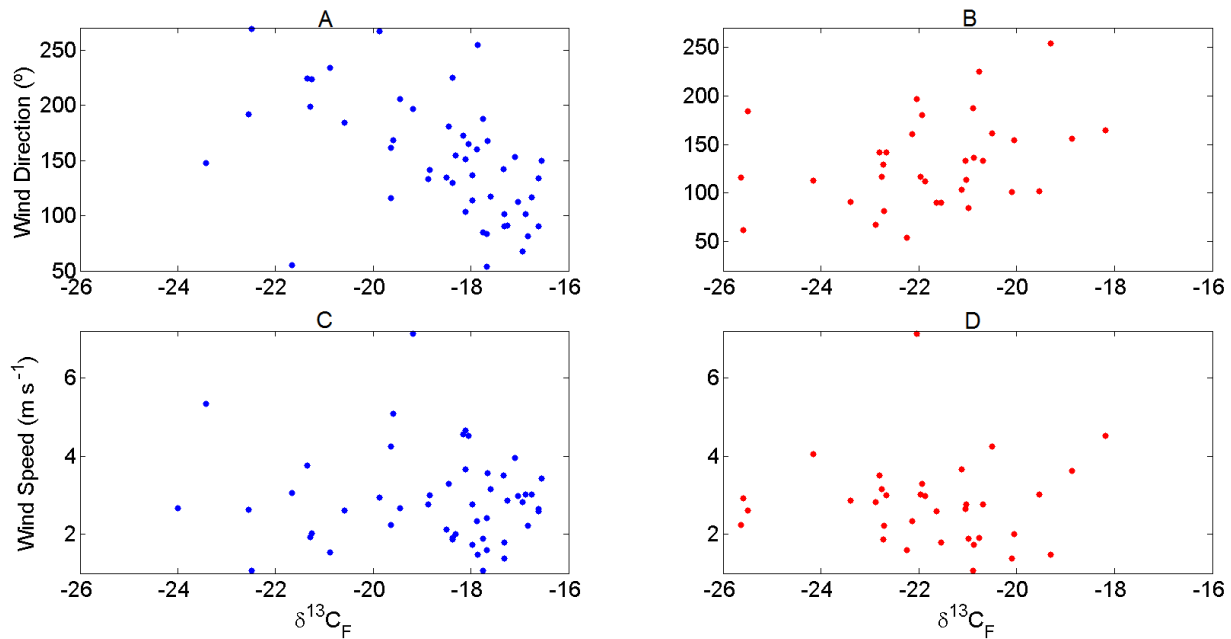


**Figure 3.18 – Plots of (A) wind direction compared to the  $\delta^{13}\text{C}_F$  signal for the ungrazed watershed, (B) wind direction compared to the  $\delta^{13}\text{C}_F$  signal for the grazed watershed, (C) wind speed compared to the  $\delta^{13}\text{C}_F$  signal for the ungrazed watershed, and (D) wind speed compared to the  $\delta^{13}\text{C}_F$  signal for the grazed watershed.**

### 3.4 Conclusion

It is apparent that this combination of micrometeorological techniques with the relatively new tunable-diode laser trace gas analyzer can adequately monitor changes in the  $\delta^{13}\text{C}_F$  and  $\delta^{13}\text{C}$  signals for comparative ecosystems with varying grassland management practices. Less filtering and more data retention might be possible by using a more sophisticated method for choosing the  $\text{CO}_2$  gradient cutoff filter for the  $\delta^{13}\text{C}_F$  signals. In addition, it might be worthwhile to install more sampling inlets. Having more sampling inlets may help provide a larger height distance between sampling inlets, which could help resolve some of the weak gradient issues. Additional inlets could be installed in different sections of both watersheds to determine if there is similar variability in the  $\delta^{13}\text{C}_F$  and  $\delta^{13}\text{C}$  signals. As noted in Chapter 2, issues can arise for the sampling system when adding additional sampling inlets. More inlets can lead to more partial sampling

time errors, but a tradeoff between potential errors and more reliable data points must be assessed based upon the site. Environmental conditions must also be examined more closely to determine their impact on the growth of the vegetation and the subsequent impact on the ecosystem signals of CO<sub>2</sub>. These changes to the ecosystem may ultimately influence the values of  $\delta^{13}\text{C}$  and  $\delta^{13}\text{C}_\text{F}$  signals in NEE. The complexity that environmental parameters add to the analysis of  $\delta^{13}\text{C}$  and  $\delta^{13}\text{C}_\text{F}$  signals is daunting, but such analysis will be necessary to develop a better understanding on the relationship that the environment plays on  $\delta^{13}\text{C}$  and  $\delta^{13}\text{C}_\text{F}$  signals. For now, this newly combined methodology and instrumentation practice holds great promise for future site endeavors. Many more data points are available to analyze compared to traditional methods, such as Lai et al. (2003) attempts to characterize the prairies  $\delta_\text{R}$  values, and there is hope that further improvements in the sampling methodology could drastically increase the utility of this practice. Future experiments may look to implementing a soil respiration-sampling regime that can identify changes in soil  $\delta^{13}\text{C}$  flux over time. Such an experiment could help identify the relative contribution of the soil CO<sub>2</sub> efflux component to the net ecosystem CO<sub>2</sub> exchange. In addition, future experiments should look to examine additional isotopologues, such as  $^{12}\text{C}^{18}\text{O}^{16}\text{O}$ , because they could provide help to better link together water and carbon cycles. Lasers are currently available to analyze for the aforementioned isotopic compound, but independent tests have revealed the laser to be too noisy for ecosystem research. More technology updates could bolster this instrument, allowing for even better carbon and water cycle analysis studies.

## Bibliography

- Albanito, F., McAllister, J., Cescatti, A., Smith, P., & Robinson, D. (2012). Dual-chamber measurements of  $\delta^{13}\text{C}$  of soil-respired  $\text{CO}_2$  partitioned using a field-based three end-member model. *Soil Biology and Biochemistry*, 47, pp. 106-115.
- Allan, D. W. (1966). Statistics of atomic frequency standards. *Proceedings of the IEEE*, 54(2), pp. 221-230.
- Allred, B. W., Fuhlendorf, S. D., & Hamilton, R. G. (2011). The role of herbivores in Great Plains conservation: comparative ecology of bison and cattle. *Ecosphere*, 2(3), pp. 1-17.
- Amundson, R., Stern, L., Baisden, T., & Wang, Y. (1998). The isotopic composition of soil and soil-respired  $\text{CO}_2$ . *Geoderma*, 82(1), pp. 83-114.
- Anderson, R. C. (2006). Evolution and origin of the Central Grassland of North America: climate, fire, and mammalian grazers. *The Journal of the Torrey Botanical Society*, 133(4), pp. 626-647.
- Arguez, A., Durre, I., Applequist, S., Vose, R., Squires, M., Yin, X., Heim, R., & Owen, T. (2012). NOAA's 1981-2010 U.S. Climate Normals: An Overview. *Bulletin of the American Meteorological Society*, 93, pp. 1687-1697.
- Atkin, O. K., Bloomfield, K. J., Reich, P. B., Tjoelker, M. G., Asner, G. P., Bonal, D., Bönisch, G., Bradford, M.G., Cemusak, L., & Cosio, E. G. (2015). Global variability in leaf respiration in relation to climate, plant functional types and leaf traits. *New Phytologist*, 206(2), pp. 614-636.
- Bahn, M., Rodeghiero, M., Anderson-Dunn, M., Dore, S., Gimeno, C., Drösler, M., Williams, M., Ammann, C., Berninger, F., & Flechard, C. (2008). Soil respiration in European grasslands in relation to climate and assimilate supply. *Ecosystems*, 11(8), pp. 1352-1367.
- Baldocchi, D., Reichstein, M., Papale, D., Koteen, L., Vargas, R., Agarwal, D., & Cook, R. (2012). The role of trace gas flux networks in the biogeosciences. *EOS Transactions American Geophysical Union*, 93(23), pp. 217-218.
- Baldocchi, D. (2003). Assessing the eddy covariance technique for evaluating carbon dioxide exchange rates of ecosystems: past, present and future. *Global Change Biology*, 9(4), pp. 479-492.
- Balogh, J., Papp, M., Pintér, K., Fóti, S., Posta, K., Eugster, W., & Nagy, Z. (2015). Autotrophic component of soil respiration is repressed by drought more than the heterotrophic one in a dry grassland. *Biogeosciences Discussions*, 12(20), pp. 16885-16911.

- Barbour, M. M., Evans, J. R., Simonin, K. A., & Caemmerer, S. (2016). Online CO<sub>2</sub> and H<sub>2</sub>O oxygen isotope fractionation allows estimation of mesophyll conductance in C<sub>4</sub> plants, and reveals that mesophyll conductance decreases as leaves age in both C<sub>4</sub> and C<sub>3</sub> plants. *New Phytologist*, 210(3), pp. 875-889.
- Beverly, D., & Franklin, S. (2015). Heterotrophic and Autotrophic Soil Respiration under Simulated Dormancy Conditions. *Open Journal of Forestry*, 5(03), p. 274.
- Blair, J., Nippert, J., & Briggs, J. (2014). Grassland Ecology. In Russell, M. (Eds.), *Ecology and the Environment* (pp. 389-423). New York, NY: Springer-Verlag.
- Bond-Lamberty, B., & Thomson, A. (2010). A global database of soil respiration data. *Biogeosciences*, 7(6), pp. 1915-1926.
- Bowling, D. R., Hall, S. J., & Egan, J. (2015). Environmental forcing does not induce diel or synoptic variation in the carbon isotope content of forest soil respiration. *Biogeosciences*, 12(16), pp. 5143-5160.
- Bowling, D.R., Pataki, D.E., & Ehleringer, J.R. (2003). Critical evaluation of micrometeorological methods for measuring ecosystem-atmosphere isotopic exchange of CO<sub>2</sub>. *Agricultural and Forest Meteorology*, 116(3-4), pp. 159-179.
- Bowling, D. R., Pataki, D. E., & Randerson, J. T. (2008). Carbon isotopes in terrestrial ecosystem pools and CO<sub>2</sub> fluxes. *New Phytologist*, 178(1), pp. 24-40.
- Bowling, D. R., Tans, P. P., & Monson, R. K. (2001). Partitioning net ecosystem carbon exchange with isotopic fluxes of CO<sub>2</sub>. *Global Change Biology*, 7(2), pp. 127-145.
- Brüggemann, N., Gessler, A., Kayler, Z., Keel, S., Badeck, F., Barthel, M., Boeckx, P., Buchmann, N., Brugnoli, E., Esperschütz, J., Gavrichkova, O., Ghashghaie, J., Gomez-Casanovas, N., Keitel, C., Knohl, A., Kuptz, D., Palacio, S., Salmon, Y., Uchida, Y., & Bahn, M. (2011). Carbon allocation and carbon isotope fluxes in the plant-soil-atmosphere continuum: a review. *Biogeosciences*, 8(11), pp. 3457-3489.
- Burba, G. (2013). *Eddy covariance method for scientific, industrial, agricultural and regulatory applications: A field book on measuring ecosystem gas exchange and areal emission rates*: Lincoln, NE: LI-COR Biosciences.
- Cescatti, A., Marcolla, B., Goded, I., & Gruening, C. (2016). Optimal use of buffer volumes for the measurement of atmospheric gas concentration in multi-point systems. *Atmospheric Measurement Techniques*, 2016, 9(9), pp. 4665-4672.
- Ciais, P., Sabine, C., Bala, G., Bopp, L., Brovkin, V., Canadell, J., ... Thornton, P. (2013). Carbon and other biogeochemical cycles *Climate Change 2013: The Physical Science Basis. Contribution of Working Group I to the Fifth Assessment Report of the Intergovernmental Panel on Climate Change* (pp. 465-474). United Kingdom: Cambridge University Press.

- Chen, X., Post, W., Norby, R., & Classen, A. (2011). Modeling soil respiration and variations in source components using a multi-factor global climate change experiment. *Climate change*, 107(3), pp. 459-480.
- Clay, D. E., Clay, S. A., Reitsma, K. D., Dunn, B. H., Smart, A. J., Carlson, G. G., Horvath, D., & Stone, J. J. (2014). Does the conversion of grasslands to row crop production in semi-arid areas threaten global food supplies? *Global Food Security*, 3(1), pp. 22-30.
- Cleland, E., Chiariello, N., Loarie, S., Mooney, H., & Field, C. (2006). Diverse responses of phenology to global changes in a grassland ecosystem. *Proceedings of the National Academy of Sciences of the United States of America*, 103(37), pp. 13740-13744.
- Cobb, K. (2012, September 27th). *Isotope Geochemistry Lecture 11: Georgia Tech University*. [PowerPoint slides] Retrieved August 24, 2016 from <http://shadow.eas.gatech.edu/~kcobb/isochem/lectures.html>
- Collins, M., Knutti, R., Arblaster, J., Dufresne, J-L., Fichet, T., Friedlingstein, ... Wehner, M. (2013). Long-term climate change: projections, commitments and irreversibility. *Climate Change 2013: The Physical Science Basis. Contribution of Working Group I to the Fifth Assessment Report of the Intergovernmental Panel on Climate Change* (pp. 1029-1135). United Kingdom: Cambridge University Press.
- Collins, S. L., & Calabrese, L. B. (2012). Effects of fire, grazing and topographic variation on vegetation structure in tallgrass prairie. *Journal of Vegetation Science*, 23(3), pp. 563-575.
- Collins, S. L., Koerner, S. E., Plaut, J. A., Okie, J. G., Brese, D., Calabrese, L. B., ... Nonaka, E. (2012). Stability of tallgrass prairie during a 19-year increase in growing season precipitation. *Functional Ecology*, 26(6), pp. 1450-1459.
- Collins, S. L., & Smith, M. D. (2006). Scale-dependent interactions of fire and grazing on community heterogeneity in tallgrass prairie. *Ecology*, 87(8), pp. 2058-2067.
- Conant, R. T. (2010). Challenges and opportunities for carbon sequestration in grassland systems. *Integrated Crop Management*, 9. Food and Agricultural Organization of the United Nations.
- Cuntz, M. (2011). Carbon cycle: a dent in carbon's gold standard. *Nature*, 477(7366), pp. 547-548.
- Daily averages climate data for Konza Prairie Biological Station. NOAA National Centers for Environmental Information. Retrieved October 17<sup>th</sup>, 2016 from <http://www.ncdc.noaa.gov/cdo-web/>

- Dawson, T. E., Mambelli, S., Plamboeck, A. H., Templer, P. H., & Tu, K. P. (2002). Stable isotopes in plant ecology. *Annual review of ecology and systematics*, pp. 507-559.
- Delgado-Balbuena, J., Arredondo, J., Loescher, H., Huber-Sannwald, E., Chavez-Aguilar, G., Luna-Luna, M., & Barretero-Hernandez, R. (2013). Differences in plant cover and species composition of semiarid grassland communities of central Mexico and its effects on net ecosystem exchange. *Biogeosciences*, *10*(7), pp. 4673-4690.
- Dore, M. H. (2005). Climate change and changes in global precipitation patterns: what do we know? *Environment International*, *31*(8), pp. 1167-1181.
- Drewitt, G., Wagner-Riddle, C., & Warland, J. (2009). Isotopic CO<sub>2</sub> measurements of soil respiration over conventional and no-till plots in fall and spring. *Agricultural and Forest Meteorology*, *149*(3), pp. 614-622.
- Dufek, N., Vermeire, L., Waterman, R., & Ganguli, A. (2014). Fire and nitrogen addition increase forage quality of *Aristida purpurea*. *Rangeland Ecology & Management*, *67*(3), pp. 298-306.
- Dymond, C. C., Nitschke, C. R., Coates, K. D., & Scheller, R. M. (2016). Carbon sequestration in managed temperate coniferous forests under climate change. *Biogeosciences*, *13*(6), pp. 1933-1947.
- Earth System Research Laboratory (2016-A). The measurements: Stable isotope mass spectrometry, National Oceanic and Atmospheric Administration. Retrieved 05/03/2016 from [http://www.esrl.noaa.gov/gmd/outreach/isotopes/mass\\_spec.html](http://www.esrl.noaa.gov/gmd/outreach/isotopes/mass_spec.html)
- Earth System Research Laboratory (2016-B). The data: The story told from CO<sub>2</sub> samples, National Oceanic and Atmospheric Administration. Retrieved 12/13/2016 from <https://www.esrl.noaa.gov/gmd/infodata/isotopes/mixing.html>
- Eskelinen, A., Stark, S., & Männistö, M. (2009). Links between plant community composition, soil organic matter quality and microbial communities in contrasting tundra habitats. *Oecologia*, *161*(1), pp. 113-123.
- Farquhar, G. D., Ehleringer, J. R., & Hubick, K. T. (1989). Carbon isotope discrimination and photosynthesis. *Annual review of plant biology*, *40*(1), pp. 503-537.
- Fassbinder, J. J., Griffis, T. J., & Baker, J. M. (2012). Interannual, seasonal, and diel variability in the carbon isotope composition of respiration in a C<sub>3</sub>/C<sub>4</sub> agricultural ecosystem. *Agricultural and Forest Meteorology*, *153*, pp. 144-153.
- Field, C. B., Lobell, D. B., Peters, H. A., & Chiariello, N. R. (2007). Feedbacks of Terrestrial Ecosystems to Climate Change. *Annual Review of Environment and Resources*, *32*(1), pp. 1-29.

- Fischer, M. L., Torn, M. S., Billesbach, D. P., Doyle, G., Northup, B., & Biraud, S. C. (2012). Carbon, water, and heat flux responses to experimental burning and drought in a tallgrass prairie. *Agricultural and Forest Meteorology*, *166*, pp. 169-174.
- Flanagan, L. B., & Farquhar, G. D. (2014). Variation in the carbon and oxygen isotope composition of plant biomass and its relationship to water-use efficiency at the leaf-and ecosystem-scales in a northern Great Plains grassland. *Plant, Cell & Environment*, *37*(2), pp. 425-438.
- Flexas, J., Barbour, M. M., Brendel, O., Cabrera, H. M., Carriquí, M., Díaz-Espejo, A., ... Warren, C. (2012). Mesophyll diffusion conductance to CO<sub>2</sub>: An unappreciated central player in photosynthesis. *Plant Science*, *193-194*, pp. 70-84.
- Franks, S. J., Weber, J. J., & Aitken, S. N. (2014). Evolutionary and plastic responses to climate change in terrestrial plant populations. *Evolutionary Applications*, *7*(1), pp. 123-139.
- Gangi, L., Rothfuss, Y., Ogée, J., Wingate, L., Vereecken, H., & Brüggemann, N. (2015). A New Method for In Situ Measurements of Oxygen Isotopologues of Soil Water and Carbon Dioxide with High Time Resolution. *Vadose zone journal*, *14*(8), pp. 1-14.
- Garcia-Pausas, J., & Paterson, E. (2011). Microbial community abundance and structure are determinants of soil organic matter mineralisation in the presence of labile carbon. *Soil Biology and Biochemistry*, *43*(8), pp. 1705-1713.
- Ghashghaie, J., & Badeck, F. W. (2014). Opposite carbon isotope discrimination during dark respiration in leaves versus roots—a review. *New Phytologist*, *201*(3), pp. 751-769.
- Ghashghaie, J., & Tcherkez, G. (2012). Isotope ratio mass spectrometry technique to follow plant metabolism: principles and applications of <sup>12</sup>C/<sup>13</sup>C isotopes. In D. Rolin, J-P Jacquot, & P. Gadal (Eds.), *Metabolomics Coming of Age with its Technological Diversity*, *67*, pp. 377-405. United Kingdom: Elsevier.
- Ghosh, P., & Brand, W. A. (2003). Stable isotope ratio mass spectrometry in global climate change research. *International Journal of Mass Spectrometry*, *228*(1), pp. 1-33.
- Glenn, A., Amiro, B., Tenuta, M., Wagner-Riddle, C., Drewitt, G., & Warland, J. (2011). Contribution of crop residue carbon to soil respiration at a northern Prairie site using stable isotope flux measurements. *Agricultural and Forest Meteorology*, *151*(8), pp. 1045-1054.
- Goffin, S., Aubinet, M., Maier, M., Plain, C., Schack-Kirchner, H., & Longdoz, B. (2014). Characterization of the soil CO<sub>2</sub> production and its carbon isotope composition in forest soil layers using the flux-gradient approach. *Agricultural and Forest Meteorology*, *188*, pp. 45-57.



- Griffis, T., Baker, J., Sargent, S., Tanner, B., & Zhang, J. (2004). Measuring field-scale isotopic CO<sub>2</sub> fluxes with tunable diode laser absorption spectroscopy and micrometeorological techniques. *Agricultural and Forest Meteorology*, 124(1), pp.15-29.
- Griffis, T., Sargent, S., Baker, J., Lee, X., Tanner, B., Greene, J., Greene, J., Billmark, K. (2008). Direct measurement of biosphere-atmosphere isotopic CO<sub>2</sub> exchange using the eddy covariance technique. *Journal of Geophysical Research: Atmospheres*, 113(D0804), pp. 1-20.
- Griffis, T., Zhang, J., Baker, J., Kljun, N., & Billmark, K. (2007). Determining carbon isotope signatures from micrometeorological measurements: Implications for studying biosphere-atmosphere exchange processes. *Boundary-layer meteorology*, 123(2), pp. 295-316.
- Griffis, T. J. (2013). Tracing the flow of carbon dioxide and water vapor between the biosphere and atmosphere: A review of optical isotope techniques and their application. *Agricultural and Forest Meteorology*, 174-175, pp. 85-109.
- Guo, L. B., & Gifford, R. (2002). Soil carbon stocks and land use change: a meta analysis. *Global Change Biology*, 8(4), pp. 345-360.
- Harrison, S. P., Gornish, E. S., & Copeland, S. (2015). Climate-driven diversity loss in a grassland community. *Proceedings of the National Academy of Sciences*, 112(28), pp. 8672-8677.
- Hashimoto, S., Carvalhais, N., Ito, A., Migliavacca, M., Nishina, K., & Reichstein, M. (2015). Global spatiotemporal distribution of soil respiration modeled using a global database. *Biogeosciences*, 12, pp. 4121-4132.
- Haslwanter, A., Hammerle, A., & Wohlfahrt, G. (2009). Open-path vs. closed-path eddy covariance measurements of the net ecosystem carbon dioxide and water vapour exchange: a long-term perspective. *Agricultural and Forest Meteorology*, 149(2), pp. 291-302.
- Henn, M. R., & Chapela, I. H. (2000). Differential C isotope discrimination by fungi during decomposition of C<sub>3</sub>-and C<sub>4</sub>-derived sucrose. *Applied and Environmental Microbiology*, 66(10), pp. 4180-4186.
- Jones, M. B., & Jongen, M. (1996). Sensitivity of temperate grassland species to elevated atmospheric CO<sub>2</sub> and the interaction with temperature and water stress. *Agricultural and Food Science*, 5(3), pp. 271-283.
- Keeling, C. D. (1979). The Suess effect: <sup>13</sup>Carbon-<sup>14</sup>Carbon interrelations. *Environment International*, 2(4-6), pp. 229-300.

- Kendall, C., & McDonnell, J.J. (1998). Fundamentals of isotope geochemistry. In C. Kendall & E.A. Caldwell (Eds), *Isotope tracers in catchment hydrology* (pp. 51-86). Amsterdam: Elsevier Science.
- Knapp, E. E., Estes, B. L., & Skinner, C. N. (2009). Ecological effects of prescribed fire season: a literature review and synthesis for managers.
- Knapp, M. (n.d.). *Kansas's Climate – The CoCoRaHS 'State Climates' Series* [PDF document]. Retrieved on October 19<sup>th</sup>, 2016 from [http://www.cocorahs.org/Media/docs/ClimateSum\\_KS.pdf](http://www.cocorahs.org/Media/docs/ClimateSum_KS.pdf)
- Kodama, N., Cousins, A., Tu, K. P., & Barbour, M. M. (2011). Spatial variation in photosynthetic CO<sub>2</sub> carbon and oxygen isotope discrimination along leaves of the monocot triticale (*Triticum* × *Secale*) relates to mesophyll conductance and the Péclet effect. *Plant, Cell & Environment*, 34(9), pp. 1548-1562.
- Konza Prairie LTER Data Catalog. [PDF Document]. pp. 157-160. Retrieved September 5, 2016 from: <http://www.konza.ksu.edu/knz/docs/DC.pdf>
- Köhler, P., Schmitt, J., & Fischer, H. (2006). On the application and interpretation of Keeling plots in paleo climate research for deciphering <sup>13</sup>C of atmospheric CO<sub>2</sub> measured in ice cores. *Biogeosciences Discussions*, 3(3), pp. 513-573.
- Kuzyakov, Y. (2006). Response to the comments by Peter Högberg, Nina Buchmann and David J. Read on the review 'Sources of CO<sub>2</sub> efflux from soil and review of partitioning methods' (*Soil Biology & Biochemistry* 38, pp. 425–448): Object-versus method-oriented terminology. *Soil Biology and Biochemistry*, 38(9), pp. 2999-3000.
- Lai, C.-T., Schauer, A., Owensby, C., Ham, J., & Ehleringer, J. (2003). Isotopic air sampling in a tallgrass prairie to partition net ecosystem CO<sub>2</sub> exchange. *Journal of Geophysical Research*, 108(D18), p. 4566.
- Law, B. (2005). Carbon dynamics in response to climate and disturbance: recent progress from multi-scale measurements and modeling in AmeriFlux. In K. Omasas, I. Nouchi, & L.J. De Kok (Eds.), *Plant responses to air pollution and global change* (pp. 205-213): Tokyo: Springer-Verlag.
- Lawler, J. J., Lewis, D. J., Nelson, E., Plantinga, A. J., Polasky, S., Withey, J. C., ... Radeloff, V. C. (2014). Projected land-use change impacts on ecosystem services in the United States. *Proceedings of the National Academy of Sciences*, 111(20), pp. 7492-7497.
- Lee, X., Massman, W., & Law, B. (2004). *Handbook of micrometeorology: a guide for surface flux measurement and analysis* (Vol. 29). New York, NY: Springer Science & Business Media.

- Liu, W., Zhang, Z., & Wan, S. (2009). Predominant role of water in regulating soil and microbial respiration and their responses to climate change in a semiarid grassland. *Global Change Biology*, 15(1), pp. 184-195.
- Massman, W., & Ibrom, A. (2008). Attenuation of concentration fluctuations of water vapor and other trace gases in turbulent tube flow. *Atmospheric Chemistry and Physics*, 8(20), pp. 6245-6259.
- Matthews, H. D., & Keith, D. W. (2007). Carbon-cycle feedbacks increase the likelihood of a warmer future. *Geophysical Research Letters*, 34(9).
- McGranahan, D. A., Engle, D. M., Fuhlendorf, S. D., Miller, J. R., & Debinski, D. M. (2012). An invasive cool-season grass complicates prescribed fire management in a native warm-season grassland. *Natural Areas Journal*, 32(2), pp. 208-214.
- Mendoza-Ponce, A., & Galicia, L. (2010). Aboveground and belowground biomass and carbon pools in highland temperate forest landscape in Central Mexico. *Forestry*, 83(5), pp. 497-506.
- Meredith, L. K., Commane, R., Munger, J., Dunn, A., Tang, J., Wofsy, S. C., & Prinn, R. G. (2014). Ecosystem fluxes of hydrogen: a comparison of flux-gradient methods. *Atmospheric Measurement Techniques*, 7, pp. 2787-2805.
- Monson, R., & Baldocchi, D. (2014). Observations of turbulence fluxes: The effect of a plant canopy on atmospheric turbulence. *Terrestrial biosphere-atmosphere fluxes* (pp. 328-337). New York: Cambridge University Press.
- Muccio, Z., & Jackson, G. P. (2009). Isotope ratio mass spectrometry. *Analyst*, 134(2), pp. 213-222.
- Munger, W.J., Loeschner, H.W., & Luo, H. (2012). Measurement, tower, and site design consideration. In M. Aubinet, T. Vesala, & D. Papale (Eds.), *Eddy covariance: a practical guide to measurement and data analysis* (pp. 42-50). New York, NY: Springer Science & Business Media.
- Nickerson, N., Egan, J., & Risk, D. (2014). Subsurface approaches for measuring soil CO<sub>2</sub> isotopologue flux: Theory and application. *Journal of Geophysical Research: Biogeosciences*, 119(4), pp. 614-629.
- Norman, J. M., Garcia, R., & Verma, S.B. (1992). Soil surface CO<sub>2</sub> fluxes and carbon budget of a grassland. *Journal of Geophysical Research*, 97(D17).
- Pataki, D. E., Ehleringer, J. R., Flanagan, L., Yakir, D., Bowling, D. R., Still, C., . . . Berry, J. (2003). The application and interpretation of Keeling plots in terrestrial carbon cycle research. *Global Biogeochemical Cycles*, 17(1).

- Peichl, M., Leava, N. A., & Kiely, G. (2012). Above-and belowground ecosystem biomass, carbon and nitrogen allocation in recently afforested grassland and adjacent intensively managed grassland. *Plant and Soil*, 350(1-2), pp. 281-296.
- PhenoCam Network, University of New Hampshire, Retrieved on May 25<sup>th</sup>, 2015 from <https://phenocam.sr.unh.edu/webcam/tools/>
- Pinno, B. D., & Wilson, S. D. (2011). Ecosystem carbon changes with woody encroachment of grassland in the northern Great Plains. *Ecoscience*, 18(2), pp. 157-163.
- Post, W. M., & Kwon, K. C. (2000). Soil carbon sequestration and land-use change: processes and potential. *Global Change Biology*, 6(3), pp. 317-327.
- Qiu, G. (2006). Development and testing of Lagrangian models of scalar dispersion in canopies (Doctoral dissertation). Retrieved June 22, 2016 from <https://atrium.lib.uoguelph.ca/xmlui/handle/10214/2079>
- Raczka, B., Duarte, H., Koven, C., Ricciuto, D., Thornton, P., Lin, J., & Bowling, D. (2016) An observational constraint on stomatal function in forests: evaluating coupled carbon and water vapor exchange with carbon isotopes in the Community Land Model (CLM4.5). *Biogeosciences*, 13(18), pp. 5183-5204.
- Raich, J., & Schlesinger, W. H. (1992). The global carbon dioxide flux in soil respiration and its relationship to vegetation and climate. *Tellus B*, 44(2), pp. 81-99.
- Raich, J. W., Potter, C. S., & Bhagawati, D. (2002). Interannual variability in global soil respiration, 1980–94. *Global Change Biology*, 8(8), pp. 800-812.
- Randall, J. (2012). Considerations for prescribed burning: Timing a prescribed burn [PDF Document]. *Iowa State Extension Forestry*. Retrieved May 1, 2016 from [https://www.extension.iastate.edu/forestry/publications/PDF\\_files/PM2088C.pdf](https://www.extension.iastate.edu/forestry/publications/PDF_files/PM2088C.pdf)
- Ratajczak, Z., Briggs, J. M., Goodin, D. G., Luo, L., Mohler, R. L., Nippert, J. B., & Obermeyer, B. (2016). Assessing the Potential for Transitions from Tallgrass Prairie to Woodlands: Are We Operating Beyond Critical Fire Thresholds? *Rangeland Ecology & Management*, 69(4), pp. 280-287.
- Raynor, E. J., Joern, A., & Briggs, J. M. (2015). Bison foraging responds to fire frequency in nutritionally heterogeneous grassland. *Ecology*, 96(6), pp. 1586-1597.
- Richardson, A. D., Jenkins, J. P., Braswell, B. H., Hollinger, D. Y., Ollinger, S. V., & Smith, M.-L. (2007). Use of digital webcam images to track spring green-up in a deciduous broadleaf forest. *Oecologia*, 152(2), pp. 323-334.

- Richter, D., Wert, B. P., Fried, A., Weibring, P., Walega, J. G., White, J. W., . . . Tittel, F. K. (2009). High-precision CO<sub>2</sub> isotopologue spectrometer with a difference-frequency-generation laser source. *Optics letters*, 34(2), pp. 172-174.
- Riebeek, H. (2011). The Carbon Cycle. Retrieved May 23, 2016, from <http://earthobservatory.nasa.gov/Features/CarbonCycle/page1.php>
- Riederer, M., Pausch, J., Kuzyakov, Y., & Foken, T. (2015). Partitioning NEE for absolute C input into various ecosystem pools by combining results from eddy-covariance, atmospheric flux partitioning and <sup>13</sup>CO<sub>2</sub> pulse labeling. *Plant and Soil*, 390(1-2), pp. 61-76.
- Rinehart, L. (2006). Pasture, rangeland and grazing management. *National Sustainable Agricultural Information Service. ATTRA Publication# IP306*.
- Santos, E., Wagner-Riddle, C., Lee, X., Warland, J., Brown, S., Staebler, R., Bartlett, P., & Kim, K. (2012). Use of the isotope flux ratio approach to investigate the C<sup>18</sup>O<sup>16</sup>O and <sup>13</sup>CO<sub>2</sub> exchange near the floor of a temperate deciduous forest. *Biogeosciences*, 9(7), pp. 2385-2399.
- Sargent, S. (2015). *Performance Evaluation of a New, Tunable-Diode Laser Trace-Gas Analyzer for Isotope Ratios of Carbon Dioxide*. Paper presented at the 2015 AGU Fall Meeting.
- Scharlemann, J. P., Tanner, E. V., Hiederer, R., & Kapos, V. (2014). Global soil carbon: understanding and managing the largest terrestrial carbon pool. *Carbon Management*, 5(1), pp. 81-91.
- Schwartz, J. D. (2014). Soil as Carbon Storehouse: New Weapon in Climate Fight. *Yale Environment*, 360. Retrieved March 25, 2015 from [http://e360.yale.edu/feature/soil\\_as\\_carbon\\_storehouse\\_new\\_weapon\\_in\\_climate\\_fight/2744/](http://e360.yale.edu/feature/soil_as_carbon_storehouse_new_weapon_in_climate_fight/2744/)
- Shi, Y., Baumann, F., Ma, Y., Song, C., Kühn, P., Scholten, T., & He, J.-S. (2012). Organic and inorganic carbon in the topsoil of the Mongolian and Tibetan grasslands: pattern, control and implications. *Biogeosciences*, 9(6), pp. 2287-2299.
- Shimoda, S., Murayama, S., Mo, W., & Oikawa, T. (2009). Seasonal contribution of C<sub>3</sub> and C<sub>4</sub> species to ecosystem respiration and photosynthesis estimated from isotopic measurements of atmospheric CO<sub>2</sub> at a grassland in Japan. *Agricultural and Forest Meteorology*, 149(3), pp. 603-613.
- Šimanský, V. (2015). Changes in soil structure and soil organic matter due to different severities of fire. *Ekológia (Bratislava)*, 34(3), pp. 226-234.

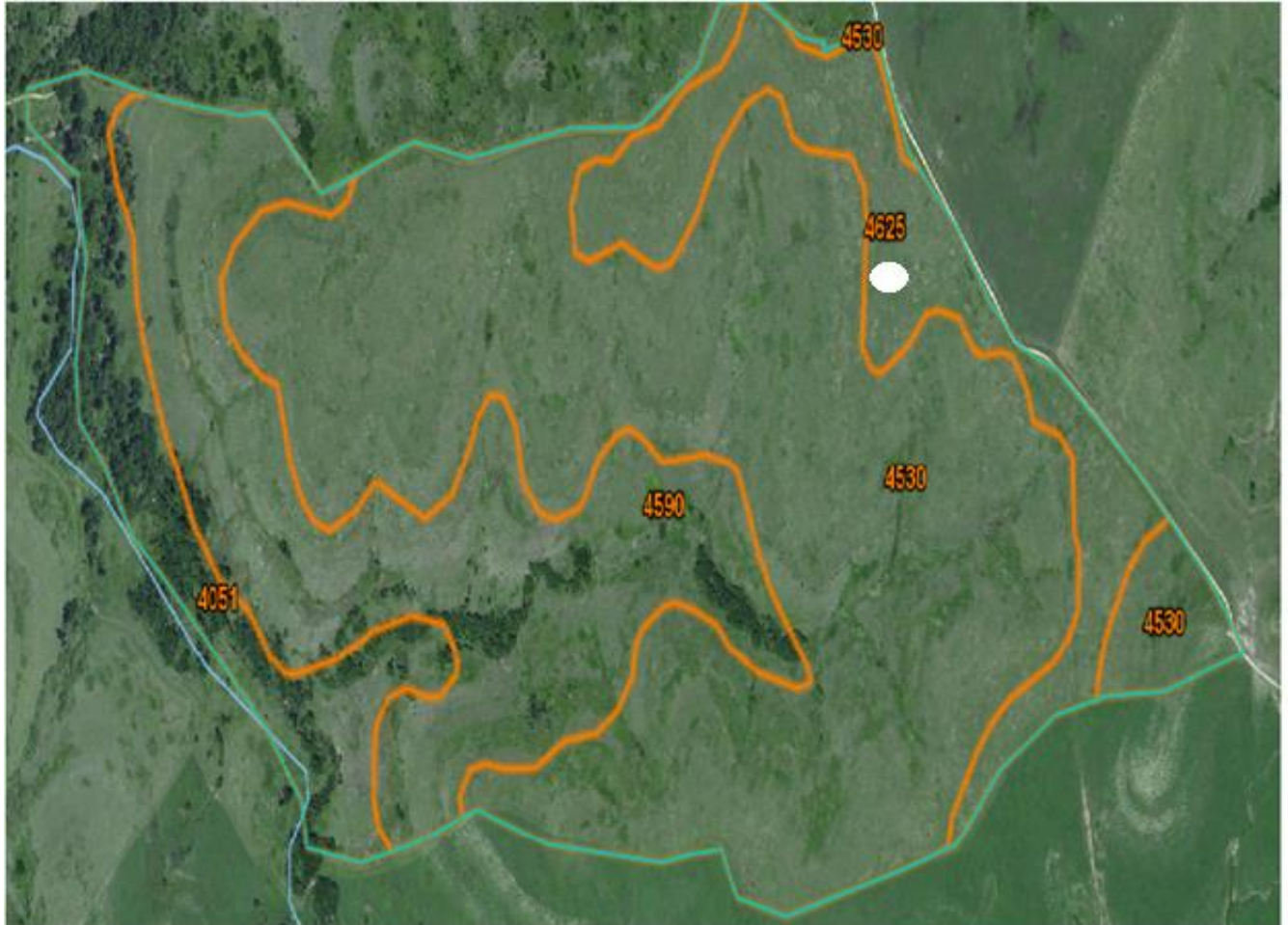
- Simonsen, V., Fleischmann, J., Whisenhunt, D., Volesky, J., & Twidwell, D. (2015). Act now or pay later: evaluating the cost of reactive versus proactive Eastern redcedar management. [Press release]
- Simpson, I., Thurtell, G., Neumann, H., Den Hartog, G., & Edwards, G. (1998). The validity of similarity theory in the roughness sublayer above forests. *Boundary-layer meteorology*, 87(1), pp. 69-99.
- Smith, K. A., & Cresser, M. S. (Eds.). (2003). *Soil and environmental analysis: modern instrumental techniques*. CRC Press. pp. 422-424.
- Spasojevic, M. J., Aicher, R. J., Koch, G. R., Marquardt, E. S., Mirotchnick, N., Troxler, T. G., & Collins, S. L. (2010). Fire and grazing in a mesic tallgrass prairie: impacts on plant species and functional traits. *Ecology*, 91(6), pp. 1651-1659.
- Stull, R. B. (1988). *An introduction to boundary layer meteorology* (Vol. 13): Springer Science & Business Media.
- Sturm, P., Eugster, W., & Knohl, A. (2012). Eddy covariance measurements of CO<sub>2</sub> isotopologues with a quantum cascade laser absorption spectrometer. *Agricultural and Forest Meteorology*, 152, pp. 73-82.
- Sun, Z., Mou, X., Li, X., Wang, L., Song, H., & Jiang, H. (2011). Application of stable isotope techniques in studies of carbon and nitrogen biogeochemical cycles of ecosystem. *Chinese Geographical Science*, 21(2), pp. 129-148.
- Taylor Jr, C. A. (2008). Ecological consequences of using prescribed fire and herbivory to manage Juniperus encroachment. In O.W. Van Auken (Ed.), *Western North American Juniperus Communities* (pp. 239-252): New York, NY: Springer.
- Tcherkez, G., Mahé, A., & Hodges, M. (2011). <sup>12</sup>C/<sup>13</sup>C fractionations in plant primary metabolism. *Trends in plant science*, 16(9), pp. 499-506.
- Torn, M., Kleber, M., Zavaleta, E., Zhu, B., Field, C., & Trumbore, S. E. (2013). A dual isotope approach to isolate carbon pools of different turnover times. *Biogeosciences*, 10, pp. 8067-8081.
- Towne, E. G., & Craine, J. M. (2014). Ecological consequences of shifting the timing of burning tallgrass prairie. *PLoS ONE*, 9(7): e103423.
- Trenberth, K. E. (2011). Changes in precipitation with climate change. *Climate Research*, 47(1-2), pp. 123-138.


- Tuzson, B., Henne, S., Brunner, D., Steinbacher, M., Mohn, J., Buchmann, B., & Emmenegger, L. (2011). Continuous isotopic composition measurements of tropospheric CO<sub>2</sub> at Jungfraujoch (3580 m asl), Switzerland: real-time observation of regional pollution events. *Atmospheric Chemistry and Physics*, *11*(4), pp. 1685-1696.
- Vitiello, M. S., Scalari, G., Williams, B., & De Natale, P. (2015). Quantum cascade lasers: 20 years of challenges. *Optics express*, *23*(4), pp. 5167-5182.
- von Caemmerer, S., Ghannoum, O., Pengelly, J. J., & Cousins, A. B. (2014). Carbon isotope discrimination as a tool to explore C<sub>4</sub> photosynthesis. *Journal of experimental botany*, *65*(13), pp. 3459-3470.
- Walther, G.-R., Post, E., Convey, P., Menzel, A., Parmesan, C., Beebee, T. J., . . . Bairlein, F. (2002). Ecological responses to recent climate change. *Nature*, *416*(6879), pp. 389-395.
- Wang, L., Li, L., Chen, X., Tian, X., Wang, X., & Luo, G. (2014). Biomass allocation patterns across China's terrestrial biomes. *PloS one*, *9*(4), e93566.
- Wang, W., Zeng, W., Chen, W., Zeng, H., & Fang, J. (2013). Soil respiration and organic carbon dynamics with grassland conversions to woodlands in temperate China. *PloS one*, *8*(8), e71986.
- Wang, Y., & Hsieh, Y.-P. (2002). Uncertainties and novel prospects in the study of the soil carbon dynamics. *Chemosphere*, *49*(8), pp. 791-804.
- Wang, Y., Li, Y., Ye, X., Chu, Y., & Wang, X. (2010). Profile storage of organic/inorganic carbon in soil: From forest to desert. *Science of the Total Environment*, *408*(8), pp. 1925-1931.
- Warland, J. S., & Thurtell, G. W. (2000). A Lagrangian solution to the relationship between a distributed source and concentration profile. *Boundary-layer meteorology*, *96*(3), pp. 453-471.
- Web Soil Survey Application, Natural Resource Conservation Services. Retrieved on July 26<sup>th</sup>, 2016 from: <http://websoilsurvey.nrcs.usda.gov/>
- Wehr, R., Munger, J., McManus, J., Nelson, D., Zahniser, M., Davidson, E., . . . Saleska, S. (2016). Seasonality of temperate forest photosynthesis and daytime respiration. *Nature*, *534*(7609), pp. 680-683.
- Wehr, R., Munger, J., Nelson, D., McManus, J., Zahniser, M., Wofsy, S., & Saleska, S. (2013). Long-term eddy covariance measurements of the isotopic composition of the ecosystem-atmosphere exchange of CO<sub>2</sub> in a temperate forest. *Agricultural and Forest Meteorology*, *181*, pp. 69-84.

- Wehr, R., & Saleska, S. (2015). An improved isotopic method for partitioning net ecosystem-atmosphere CO<sub>2</sub> exchange. *Agricultural and Forest Meteorology*, 214, pp. 515-531.
- Wei, J., Cheng, J., Li, W., & Liu, W. (2012). Comparing the effect of naturally restored forest and grassland on carbon sequestration and its vertical distribution in the Chinese Loess Plateau. *PloS one*, 7(7), e40123.
- Weir, J. R. (2011). Are weather and tradition reducing our ability to conduct prescribed burns? *Rangelands*, 33(1), pp. 25-30.
- Welp, L. R., Keeling, R. F., Meijer, H. A., Bollenbacher, A. F., Piper, S. C., Yoshimura, K., . . . Wahlen, M. (2011). Interannual variability in the oxygen isotopes of atmospheric CO<sub>2</sub> driven by El Nino. *Nature*, 477(7366), pp. 579-582.
- Werner, C., & Gessler, A. (2011). Diel variations in the carbon isotope composition of respired CO<sub>2</sub> and associated carbon sources: a review of dynamics and mechanisms. *Biogeosciences*, 8(9), pp. 2437-2459
- Werner, C., Schnyder, H., Cuntz, M., Keitel, C., Zeeman, M., Dawson, T., . . . Grams, T. (2012). Progress and challenges in using stable isotopes to trace plant carbon and water relations across scales. *Biogeosciences*, 9(8), pp. 3083-3111.
- White, R. P., Murray, S., Rohweder, M., Prince, S., & Thompson, K. (2000). *Grassland ecosystems* (pp. 11-55). World Resources Institute, Washington, DC.
- Williams, M., Richardson, A., Reichstein, M., Stoy, P., Peylin, P., Verbeeck, H., ... Kattge, J. (2009). Improving land surface models with FLUXNET data. *Biogeosciences*, 6(7), pp. 1341-1359.
- Wilson, J. (1989). Turbulent transport within the plant canopy. *Estimation of Areal Evapotranspiration*, 177, pp. 43-80.
- Wu, Y., Ting, M., Seager, R., Huang, H.-P., & Cane, M. A. (2011). Changes in storm tracks and energy transports in a warmer climate simulated by the GFDL CM2. 1 model. *Climate dynamics*, 37(1-2), pp. 53-72.
- Yakir, D., & Affeck, H. (2003). The stable isotopic composition of atmospheric CO<sub>2</sub>. *Treatise on Geochemistry*, 4, pp. 192-195.
- Yakir, D., & Sternberg, L. (2000). The use of stable isotopes to study ecosystem gas exchange. *Oecologia*, 123(3), pp. 297-311.
- Zhu, B., & Cheng, W. (2011). <sup>13</sup>C isotope fractionation during rhizosphere respiration of C<sub>3</sub> and C<sub>4</sub> plants. *Plant and Soil*, 342(1-2), pp. 277-287.



## Appendix A - Table of the soil mapping units distribution for the K2A watershed

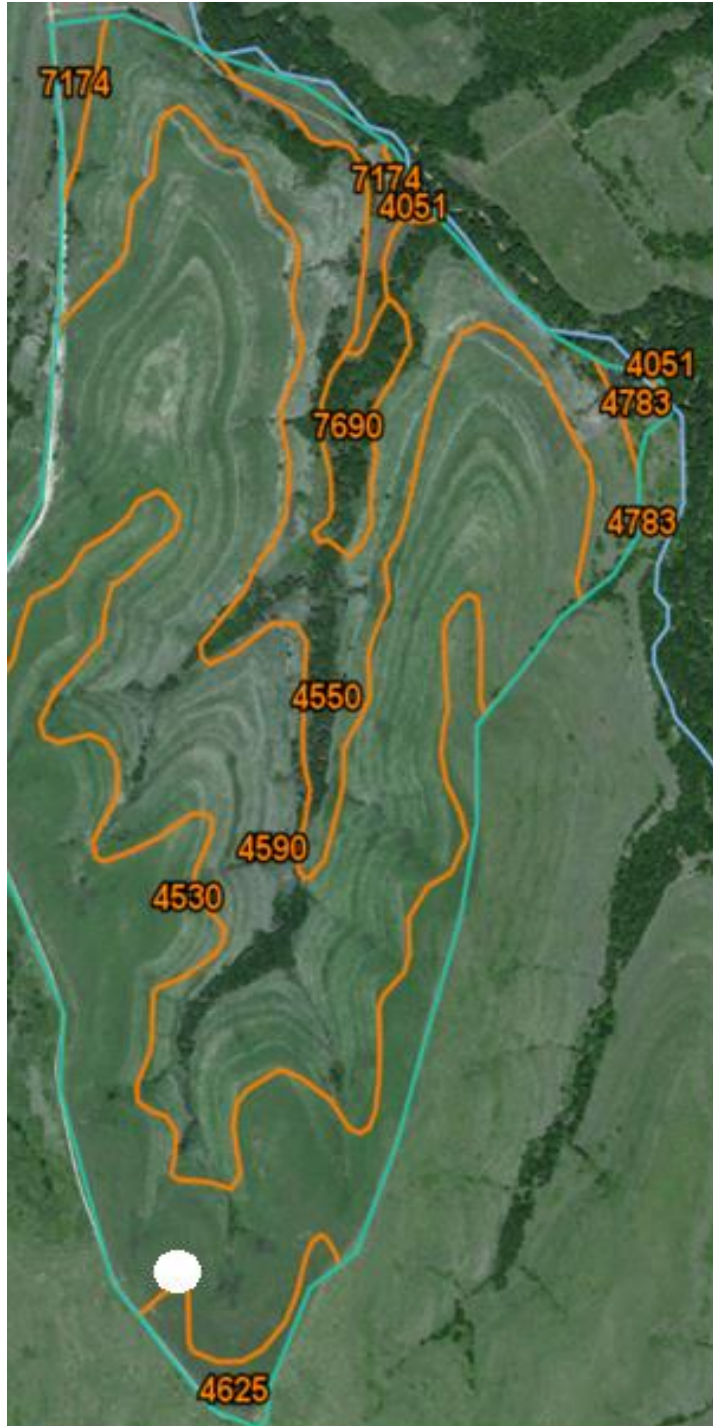


0  1,000 ft



Map Unit Symbol	Map Unit Name	Acres in AOI	Percent of AOI
4051	Ivan silt loam, channeled	14.4	9.2%
4530	Benfield-Florence complex, 5 to 30 percent slopes	86.3	55.0%
4590	Clime-Sogn complex, 3 to 20 percent slopes	38.6	24.6%
4625	Dwight-Irwin complex, 1 to 3 percent slopes	17.6	11.2%
<b>Totals for Area of Interest</b>		<b>156.9</b>	<b>100.0%</b>

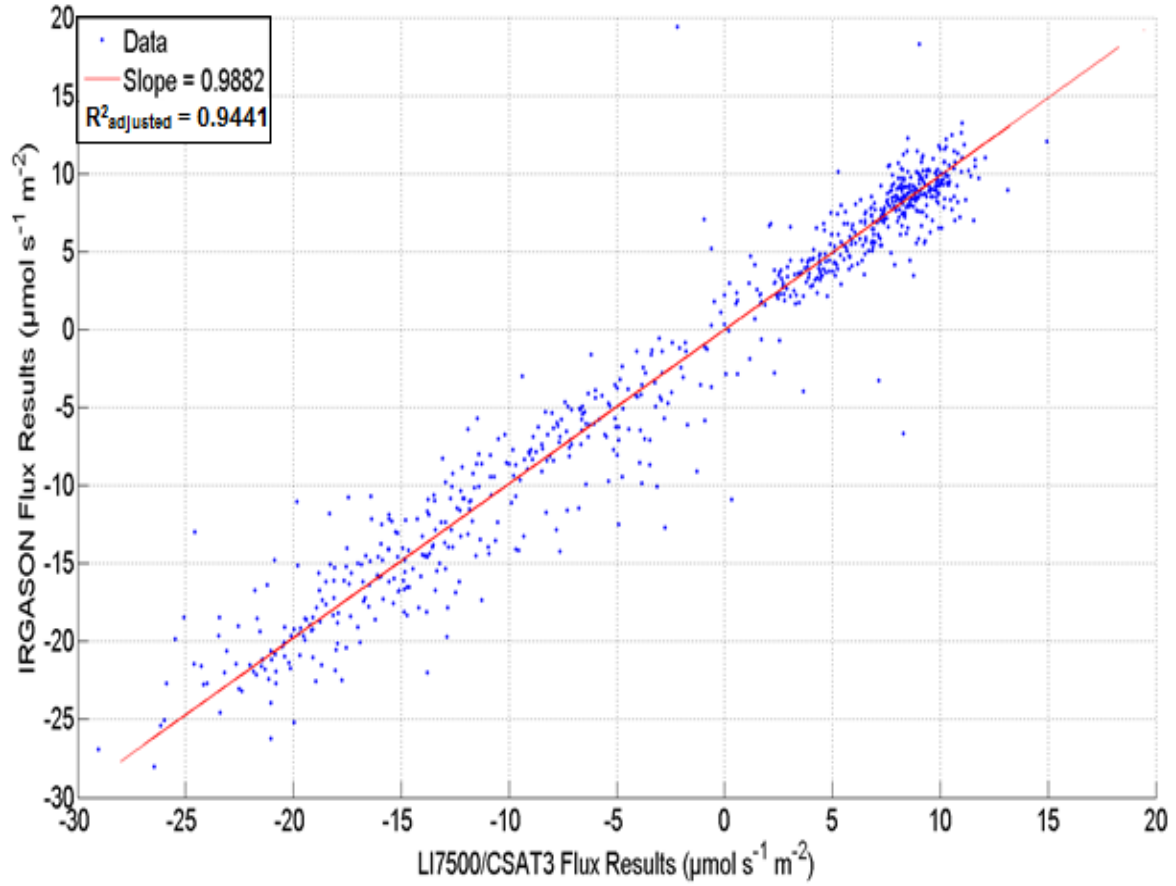
## Appendix B - Table of the soil mapping units distribution for the C3SA watershed



Map Unit Symbol	Map Unit Name	Acres in AOI
4051	Ivan silt loam, channeled	0.5
4530	Benfield-Florence complex, 5 to 30 percent slopes	65.9
4550	Clime silty clay loam, 20 to 40 percent slopes, very stony	51.9
4590	Clime-Sogn complex, 3 to 20 percent slopes	129.3
4625	Dwight-Irwin complex, 1 to 3 percent slopes	4.5
4783	Tully silty clay loam, 3 to 7 percent slopes	1.6
7174	Reading silt loam, 1 to 3 percent slopes	7.3
7690	Wymore-Kennebec complex, 0 to 17 percent slopes	5.4
<b>Totals for Area of Interest</b>		<b>266.4</b>



# Appendix C - IRGASON flux measurements compared to LI7500/CSAT3 flux measurements



# Appendix D - Soil CO<sub>2</sub> respiration model statistic tables and graphs

Number of Observations Read	32
Number of Observations Used	32

Durbin-Watson D	0.821
Pr < DW	<.0001
Pr > DW	1.0000
Number of Observations	32
1st Order Autocorrelation	0.521

Root MSE	0.10968	R-Square	0.6905
Dependent Mean	0.36739	Adj R-Sq	0.6692
Coeff Var	29.85297		

Analysis of Variance					
Source	DF	Sum of Squares	Mean Square	F Value	Pr > F
Model	2	0.77836	0.38918	32.35	<.0001
Error	29	0.34885	0.01203		
Corrected Total	31	1.12720			

Parameter Estimates					
Variable	DF	Parameter Estimate	Standard Error	t Value	Pr >  t
Intercept	1	-0.55056	0.11880	-4.63	<.0001
SoilTemperature	1	0.02986	0.00480	6.22	<.0001
SoilVWC	1	0.00874	0.00201	4.34	0.0002

